Stony Brook University

Solid state NMR and pair distribution function analysis studies

of Ge and Sn anodes for Li-ion batteries

A Dissertation Presented

by

Hyeyoung Jung

to

The Graduate School

in Partial Fulfillment of the Requirements

for the Degree of

Doctor of Philosophy

in

Chemistry

Stony Brook University

August 2015

Stony Brook University

The Graduate School

Hyeyoung Jung

We, the dissertation committee for the above candidate for the

Doctor of Philosophy degree, hereby recommend acceptance of this dissertation.

Clare P. Grey, Dissertation Advisor
Professor, Department of Chemistry, Stony Brook University

Peter Khalifah, Chairperson of Defense
Professor, Department of Chemistry, Stony Brook University

Robert B. Grubbs, Third Member
Professor, Department of Chemistry, Stony Brook University

Jordi Cabana, outside member
Professor, Department of Chemistry, University of Illinois at Chicago

This dissertation is accepted by the Graduate School

Charles Taber
Dean of the Graduate School

Abstract of the Dissertation

Title of Dissertation

by

Hyeyoung Jung

Doctor of Philosophy

in

Chemistry

Stony Brook University

2015

Metallic germanium and tin are attractive anode candidates in secondary lithium-ion batteries (LIBs) due to their high theoretical capacities and low operating voltages. They undergo (de) alloying processes with Li and exhibit much higher theoretical capacities, germanium (1623 mAh/g) and tin (993mAh/g), compared with graphite (375mAh/g).

Recently, germanium has been considered as a promising anode material for next generation LIBs due to its high capacity, fast lithium diffusion, and high electronic conductivity. Here, the (de) lithiation mechanism of micron-sized and nano-sized Ge anodes has been investigated with X-ray diffraction (XRD), pair distribution function (PDF) analysis, and *in/ex situ* high-resolution ^{7}Li solid-state nuclear magnetic resonance (NMR), utilizing the structural information and spectroscopic fingerprints obtained by characterizing a series of relevant Li_xGe_y model compounds. The lithiation process of micron-sized Ge anodes involves the formation of the Li_7Ge_3 phase initially through a two–phase reaction process. Li_7Ge_3 converts to Li_7Ge_2 via a series of highly disordered phases, all of these phases contain columns of Li, Ge-Ge, and Ge, with the relative proportions varying as lithiation proceeds. Eventually, Li_7Ge_2-like short-to-meduim range environments are observed. At this point, the nucleation and growth to form

crystalline $Li_{15}Ge_4$ occurs. Upon delithiation, a reverse conversion process occurs and finally formed amorphous Ge at the end of charge.

Tin is also another promising anode material due to its high capacity and compatibility with other elements. Here, relevant Li_xSn_y model compounds (with nominal compositions Li_2Sn_5, LiSn, Li_7Sn_3, Li_7Sn_2, and $Li_{22}Sn_5$) were synthesized and characterized by XRD, $^7Li/^{119}Sn$ solid-state NMR and PDF analysis to assist with the identification and structural determination of the Li_xSn_y phases that form during electrochemical lithiation.

These results provide insights into Li_xGe_y and Li_xSn_y phases transformation during cycling and will guide the further development of Li-alloy based anode materials for battery applications.

Table of Contents

List of Figures and Tables

Chapter 1

Chapter 2

Chapter 3

Chapter 4

Chapter 5

List of Abbreviations

2D	**2-dimentional**
CMC	Carboxyl methyl cellulose sodium salt
DBP	Dibutyl phtalate
DFT	Density function theory
DMC	Dimethyl Carbonate
EC	Ethylene Carbonate
EXAFS	Extended X-ray absorption fine structure
FEC	Fluoroethylene carbonate
FWHM	Full width at half maximum
GITT	Galvanostatic Intermittent Titration Technique
HEBM	High Energy Ball Milling
LIB	Lithium Ion Battery
MAS	Magic Angle Spinning
NMR	Nuclear Magnetic Resonance
OCV	Open Circuit Voltage
PAA	Polyacrylic acid
PDF	Pair Distribution Function
PTFE	Polytetrafluoroethylene
PVDF	Poly-vinylidene floride
RF	Radio frequency
SBR	Styrene butadiene rubber
SEI	Solid Electrolyte Interphase
SEM	Scanning Electron Microscopy
SOC	State of charge
SS	Solid state
TEM	Transmission Electron Microscopy
TXM	Hard X-ray transmission X-ray microscopy
XAS	X-ray absorption spectroscopy
XRD	X-Ray Diffraction
VC	Vinylene carbonate
VSP	Biologic potentiostat/galvanostat

Acknowledgments

First and foremost, I would like to thank my advisor, Professor Clare P. Grey, for providing me this great chance doing exciting research in this group and for her guidance and patience throughout my doctoral studies. It was a truly amazing experience to have her as an advisor during last six years. Her brilliant intuition of science and kindness always inspired me to find a breakthrough on my research and none of my work would make any sense without her assistance. I also would like to thank my committee members: Professors Peter Khalifah, Robert B. Grubbs, and Jordi Cabana for their encouragement and constructive criticism.

I would like to express my true gratitude to my NMR mentors, who have introduced me the beauty of NMR: Dr. Lin-Shu Du and Dr. Yan-Yan Hu. Thank you for sharing their profound scientific intuition and also for their enormous help and friendship during my PhD.

I would also thank Dr. Phoebe K. Allan, who taught me almost everything about PDF refinements. Her help, patience, assistance, and insightful suggestions, are truly appreciated.

I thank Dr. Nicole Trease for her big help in conducting Sn NMR experiments and data interpretations. I thank Dr. Olaf Borkiewicz, Dr. Karena W. Chapman, and Dr. Peter J. Chupas for their big assitance in collecting PDF data, data processing and collaborations.

I am also incredibly thankful to all my officemates throughout my doctoral studies and I was not able to finish my PhD without their help and friendship. In particular, I would like to thank my coffee buddy, Hee Jung Chang for her friendship and Shou-Hang Bo for sharing enthusiasm for science and fruitful discussions. I am also grateful to Gunwoo Kim for his help and friendship in Cambridge. I would like to thank all the past and present Grey group members in Stony Brook and Cambridge.

Last but not least, I want to express my deepest appreciation to my family. I am grateful to my parents, my husband, Kee Hyouk Lee, and my most adorable sweetheart, Hojin and Hyunjin, for the love, devotion, and support during last six years in Stony Brook. This would not have been possible without their tremendous love and help.

Chapter 1. Introduction

1.1. Lithium Ion batteries

Currently, fossil fuels are used for major energy sources, but fossil fuels are limited in supply and will be eventually depleted. In addition, the production and use of fossil fuels cause severe environmental issues. For example, CO_2 emission from petroleum industries is a main cause of global warming. The global demand for alternative energy sources has increased dramatically in the past decades.

Rechargeable batteries (secondary batteries) store electricity in a chemical form and can be used as an alternative energy. They can be re-charged and re-used as a handy and portable power source.

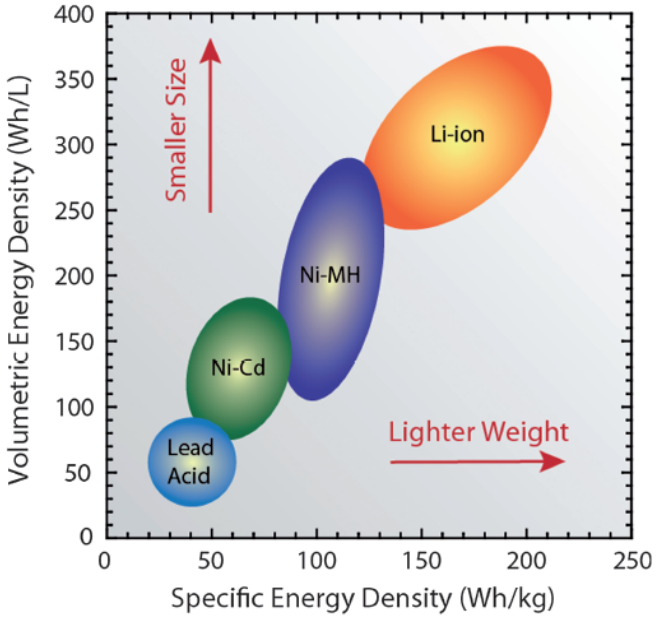

Figure 1.1. Comparison of rechargeable battery technologies based on their energy storage ability. (Figure taken from reference 1)

Typical types of rechargeable batteries are lead-acid, nickel-cadmium (Ni-Cd), nickel-metal hydride (Ni-MH), lithium ion batteries (Li-ion) and lithium metal batteries.

Figure 1.1 gives a comparison of different types of rechargeable batteries based on their energy storage ability. Among the rechargeable batteries, lithium ion batteries (LIBs) have the best capability in terms of volumetric energy density (Wh/L) and gravimetric energy (Wh/kg). LIBs can store more than twice the energy of other cells of the same mass and size, as shown in Figure 1.1.

Commercialized lithium ion batteries (shown in Figure 1.2) consist of a lithium metal oxide (i.e., $LiCoO_2$) as a cathode, graphite as an anode and an electrolyte solution (such as $LiPF_6$ in ethylene carbonate and dimethyl carbonate). Both electrode materials have layered structures, allowing Li ions to move in and out of the layers. During charging, Li ions move from the positive electrode and are intercalated into the negative electrode, while discharging, Li ions are extracted from the negative electrode and reinserted into the positive electrode. [1,2]

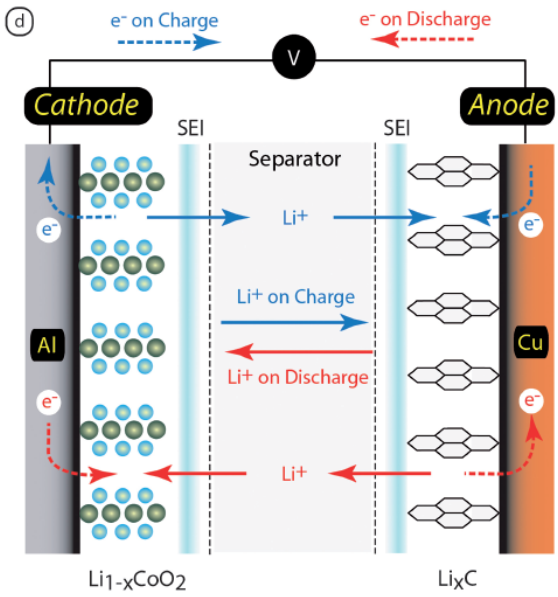

Figure 1.2. Intercalation mechanism of Li ion batteries.
(Figure taken from reference 1)

1.1.1. Lithium metal and Carbon

Li metal is in principle an attractive anode candidate since it is the lightest and the most electropositive (-3.04V *vs.* standard hydrogen electrode) material among metals.[3] However, it suffers from two main issues 1) dendrites form at the anode during charging, which causes short-circuiting; 2) the high chemical reactivity of metallic Li, which results in poor battery characteristics. The uneven dendritic growth that can occur during charge-discharge cycles presents an explosion hazard, limiting the use of these Li anode systems. Due to the apparent safety issues with lithium metal-based batteries, research studies have turned to alternative anode materials.

Carbons have been pursued as alternatives to lithium metal and enabled the LIBs to become commercially viable. There are several types of carbons of varying crystallinity that have varying electrochemical performance. The general reaction that occurs in the carbon-based batteries is as follows,

$$Li_xC_n \leftrightarrow xLi^+ + xe^- + C_n \qquad [1.1]$$

where C_n can represent any of the variety of available carbons.

Electrochemical activity in graphitic carbons comes from the intercalation of lithium between the graphene layers, which offer good 2-dimensional mechanical stability, electrical conductivity, and lithium transport (Figure 1.2).

1.1.2. New materials for negative electrodes.

Rechargeable lithium ion batteries have become the most popular energy storage devices for portable electronics such as laptop computers, smart phones, and electric vehicles. Since Sony introduced the first generation of Li-ion batteries (LIBs) in 1991, layered carbonaceous materials (usually graphite) have been used as a negative electrode due to good cyclability and moderate capacity compared to the positive electrode. However, as the demand for LIBs used in electric vehicles and large-scale energy storage systems is rapidly growing, it necessitates the search for new negative electrode materials with higher power and energy densities than graphite (372mAh/g).[4] Silicon, germanium, and tin are attractive anode candidates for LIBs due to their high energy densities and safety characteristics.[5] They undergo alloying processes with Li and exhibit much higher theoretical capacities than graphite, silicon (3579 mAh/g), germanium (1623 mAh/g), and tin (993 mAh/g).[6-8] Moreover, they mitigate safety issues associated with using Li metal

as anodes.[6] Figure 1.3 shows various cathode and anode materials, which are currently used or are potential future candidates.

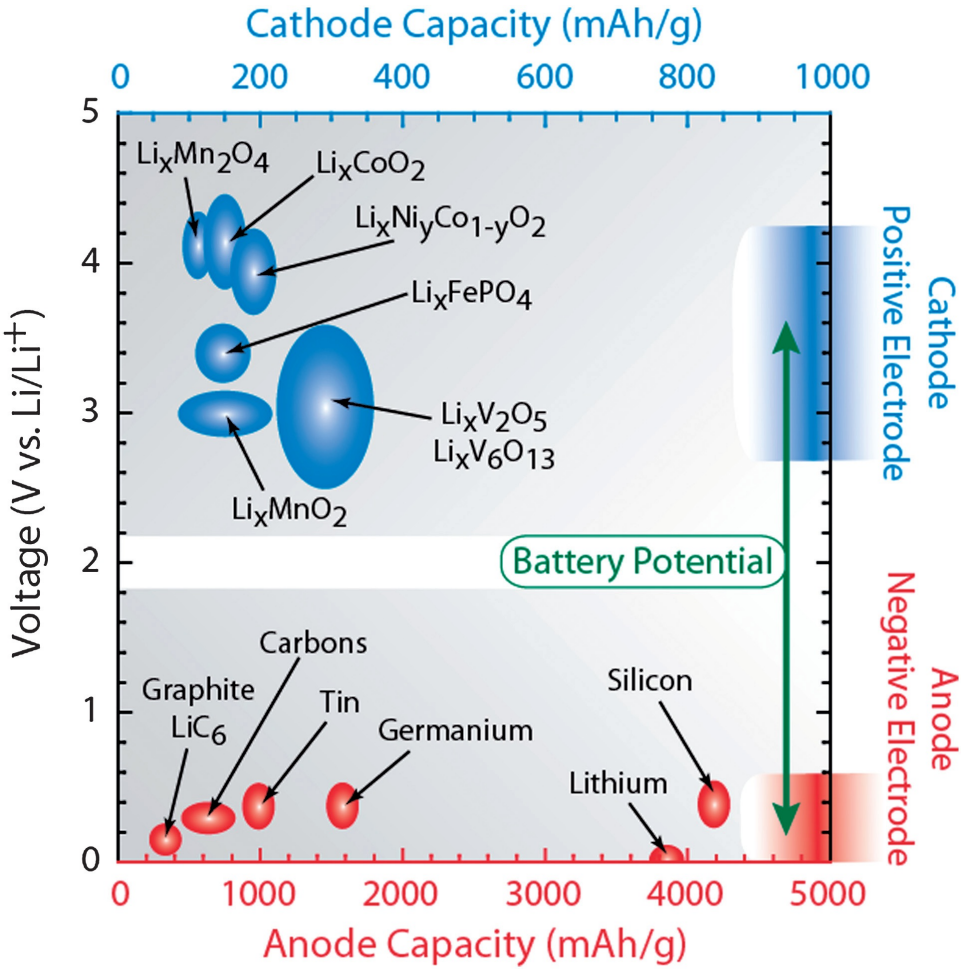

Figure 1.3. Voltage *vs.* capacity for positive and negative battery materials.

(Figure taken from references 1 and 10)

1.1.3. Li-alloy based anode materials

Li –alloy based materials (*e.g.* group IV elements: Si, Ge and Sn) are known for a larger specific capacity than graphite and reducing safety issues related to lithium deposition.

Table1.1 gives a comparison of theoretical capacity, volume expansion rates and operating voltages with respect to Li^+/Li for graphite and alloying materials. The theoretical capacities of alloy anodes are 3-10 times higher than graphite. In addition, alloy anodes show a moderated operation voltage versus lithium, which reduces the safety concern of lithium deposition as with graphite anodes (~0.05V *vs.*Li).

Table1.1. Comparison of specific (gravimetric) capacity, volume change and operating voltages of graphite and metal alloying materials.[9]

	C	Si[10,11]	Ge[11,12]	Sn[13]
Lithiated phase	LiC_6	$Li_{4.4}Si$	$Li_{4.4}Ge$	$Li_{4.25}Sn$
Specific capacity (mAh/g)	375	4200	1623	993
Volume expansion (%)	12	400	370	260
Voltage *vs.*Li	0.05	0.4	0.55	0.6

However, these materials suffer from severe volume expansion up to 400% during the lithium alloying/dealloying at the first cycle (Figure 1.4), which leads to disintegration of electrodes, poor capacity retention during cycling and a large irreversible capacity loss at the first cycle. Zhang[6] suggested several strategies for overcoming the volume changes and reducing the first cycle irreversible capacity loss of Li-alloy based anodes. Mainly these approaches have been adopted to improve the cyclic performances of group IV element (Si, Ge and Sn);

1) multiphase composites such as inactive-matrix composites (SnCo[14]), active-matrix composites (SnSb[15]), carbon-based composites, and porous structures,

2) particle size or shape control; nano-size, nano-rod, and nano-wire types,

3) thin film and amorphous alloys,

4) different binders (CMC; carboxylmethyl cellulose sodium salt, or PAA; polyacrylic acid or SBR; styrene butadiene rubber) and electrolyte (FEC;fluoroethylene carbonate, or VC; vinylene carbonate).

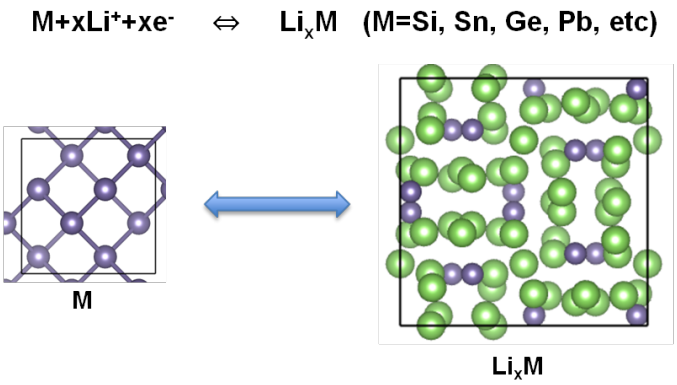

Figure 1.4. A schematic representation of the Li-alloy formation process. (Violet circles: metal, green circles: lithium)

Silicon has been shown to be one of the best candidates for replacing existing anodes due to its high capacity.[16,17] However, the high capacity is associated with large volume changes up to 400% (Table 1.1) upon lithiation, resulting in particle fracture, capacity loss and cell design issues. Many approaches have been pursued to accommodate the volume change of silicon, such as preparation of Si/carbon composites to improve the electronic conductivity and prevent the breakdown of the particle.[5,17,18] One problem with this strategy is that it requires the low operating potential to access the full carbon capacity. Furthermore, control of the volume change was attempted by particle size or morphology controls[19] (porous micron-sized particles, nano-sized particles,[20] nano-wires,[21] nanoporous structures and thin films). By analogy with silicon, the practical applications of germanium and tin based anodes are also hindered by the pulverization problem caused by the large volume change during Li insertion/extraction processes.[5,6,22,23]

In the subsequent sections (1.1.4. and 1.1.5), Ge and Sn will be introduced in detail and will be main focus of this thesis.

1.1.4. Germanium (Ge)

Recently, much research has focused on silicon anodes because they show the highest capacity among all anode materials except Li metal, and have high natural abundance and low cost, whereas germanium, with a relatively higher cost, has received little attention. Compared with silicon, germanium has 400 times greater lithium diffusivity[24] and 104 times greater electronic conductivity due to a smaller band gap (E_g(Ge) = 0.6eV and E_g(Si) = 1.1eV).[25] These properties lead to much better rate performance of Ge anodes than that of Si anodes used in LIBs. [26]

In order to enhance the cycling stability, several approaches have been developed to accommodate the volume changes of germanium during alloying/dealloying processes. The morphology of germanium has been modified to give increased structural stability, such as nano-particles[27,28], nano-wires[29-31], nano-tube[32,33] and macroporous[34]/mesoporous[35]/3D-porous nano[36] structures. Furthermore, germanium based composites (tin-germanium nano-composites[37,38], germanium/carbon composites[32,39,40]) and nano-sized germanium oxides[41] are also promising candidates for improving capacity retention.

The known binary phase diagram of Li-Ge system consists of seven experimentally reported crystalline phases: Li_7Ge_{12}, LiGe, $Li_{11}Ge_6$, Li_9Ge_4, Li_7Ge_2, $Li_{15}Ge_4$, and $Li_{22}Ge_5$.[42] In addition, $Li_{14}Ge_6$ (Li_7Ge_3) and $Li_{12}Ge_7$ [43,44,45,46] have also been reported. Recent density functional theory (DFT) calculations[11] have shown that the Li-Ge phase diagram is extremely rich. LiGe($I4_1/a$), Li_7Ge_3 ($P32_12$), $Li_{13}Ge_5$($P\bar{3}\ m1$), Li_8Ge_3($R\bar{3}\ m$), $Li_{15}Ge_4$($I\bar{4}\ 3d$)and $Li_{17}Ge_4$($F\bar{4}\ 3m$), were identified via the combined random structure searching[47,48] and atomic species swapping method[11] to be stable (*i.e.*, lie on a convex hull between Li and Ge), while other Li_xGe_y alloys, including, Li_5Ge_2, and $Li_{13}Ge_4$[11], are only slightly metastable with respect to disproportionation to the thermodynamic phases and hence are likely to be also present at room temperature.

The crystal structures of a series of Li_xGe_y compounds, relevant to the work in Chapters 2, 3 and 4, are shown in Figure 1.5. The phase Li_9Ge_4, (or $Li_{2.25}Ge$) identified in some previous electrochemical studies,[23,49] (space group, *Cmcm*) contains Ge-Ge

dumbbells with a Ge-Ge bond length of ~2.44 Å, the dumbbells being separated by 2 or 7 Li atoms in rows along the c-axis. The dumbbell columellar motif is common to Li_xGe_y structures with similar compositions. Li_7Ge_3, (or $Li_{2.33}Ge$), a stable phase identified in the previous DFT studies, adopts a $P32_12$ space group with 8 Li and 3 Ge crystallographic sites.[44] The Ge atoms also form Ge-Ge dumbbells with a Ge-Ge distance of 2.50 Å, the dumbbells being separated by either 4 or 5 Li atoms along the c-axis. Li_5Ge_2, (or $Li_{2.5}Ge$) is above the tie line in DFT studies (i.e., is metastable) and has a $R\bar{3}m$ symmetry with 3 Li and 1 Ge crystallographic sites. The Ge atoms again exist as Ge-Ge dumbbells (Ge-Ge bond distance of 2.56 Å), separated by 5 Li atoms along the c-axis.[11] $Li_{13}Ge_5$ (or $Li_{2.6}Ge$) is a thermodynamically stable phase with symmetry of $P\bar{3}m1$ and 7 Li and 3 Ge crystallographic sites. The isolated Ge atoms in this material are separated by 5 Li atoms, while the Ge-Ge dumbbells with a bond distance of 2.55Å are separated by 4 Li atoms along the c-axis.[11]

Two different polymorphs for Li_7Ge_2 have been suggested by theoretical studies, with symmetries of *Cmmm* and $P\bar{3}m1$.[11,49,50] However, only the *Cmmm* structure has been reported experimentally,[49,50] featuring Ge-Ge dumbbells and isolated Ge atoms, where 50% of the Ge atoms are present as dumbbells. The structure is comprised of columns along the a-axis; one sixth of these columns contain Ge-Ge dumbbells (with bond length 2.62 Å) separated by one Li atom, while one third of the columns contain isolated Ge with 2 Li atoms in between, the rest of the columns containing only Li atoms. Two lithium-germanium alloys with high-lithium content have been reported, $Li_{15}Ge_4$ (space group: $I\bar{4}3d$) and $Li_{22}Ge_5$ (symmetry group: $F\bar{4}3m$), both containing isolated Ge atoms in a matrix of Li.[45,49,51]

The lithium germanides Li_xGe_y (e.g., Li_9Ge_4, Li_7Ge_2, and $Li_{15}Ge_4$) lie at the border between Zintl phases and intermetallic compounds, compounds with lower Li content being better described as Zintl phases, simple electron counting rules failing for materials with higher lithium contents. The Zintl formalization can be used to rationalize electronic structure and stability.[52] In this formalism, the Li^+ ions are assumed to have a formal charge of 1+, the resulting negative charge being distributed amongst the Ge (or more generally, the less electropositive metal) to result in a complete octet (i.e., Ge^{4-} for

an isolated Ge ion). In the case of the highly polarizing Li^+ ion, however, full transfer of charge from Li to Ge does not occur in the majority of compounds, the additional electron density being found in so-called "cage orbitals" on the lithium ions.[53] The dumbbell compounds are easiest to rationalize. The Ge_2 dumbbells, with short Ge-Ge distances (Li_9Ge_4: 2.44 Å), are assigned to $(Ge_2)^{4-}$. The partial formal charge of lithium ions in Li_xGe_y is +0.89 (Li_9Ge_4: $Li_9^{8+}[Ge_2]_2^8$) and +0.86 (Li_7Ge_2: $(Ge_2)^{4-}$ and Ge^{4-}), where the remaining additional electrons are delocalized on the Li sites in the cage orbitals. According to Zintl electron counting rules,[53] $Li_{15}Ge_4$ nominally requires 16 electrons to form 4 Ge^{4-} ions, and is thus an electron deficient compound. $Li_{14}MgGe_4$ also exists and this is a conventional Zintl phase. $Li_{21}Ge_5$, by contrast, is a Li-excess compound again the additional electron being accommodate in "cage orbitals", according to Nesper[53]. However, given that this phase displays metallic properties,[42]this may not be the most appropriate way to view this material. This series of materials demonstrates the limitation of Zintl approaches to Li-rich germanides (Li_9Ge_4, Li_7Ge_2, and $Li_{15}Ge_4$).

In this study, the main goal is to investigate electrochemical lithiation/delithiation mechanisms of micron- and nano-sized germanium anodes. *Ex-situ* XRD (X-ray diffraction) was used to probe the long-range structural changes while *in-* and *ex-situ* solid state NMR and pair distribution function analysis (PDF) were employed to follow the local structural variations. Relevant Li-Ge model compounds (Li_9Ge_4, Li_7Ge_2, $Li_{15}Ge_4$, and $Li_{22}Ge_5$) were synthesized and characterized by XRD, solid-state NMR and PDF analysis to assist with the identification and confirmation of electrochemically formed Li_xGe_y phases (Chapter 2, 3 and 4).

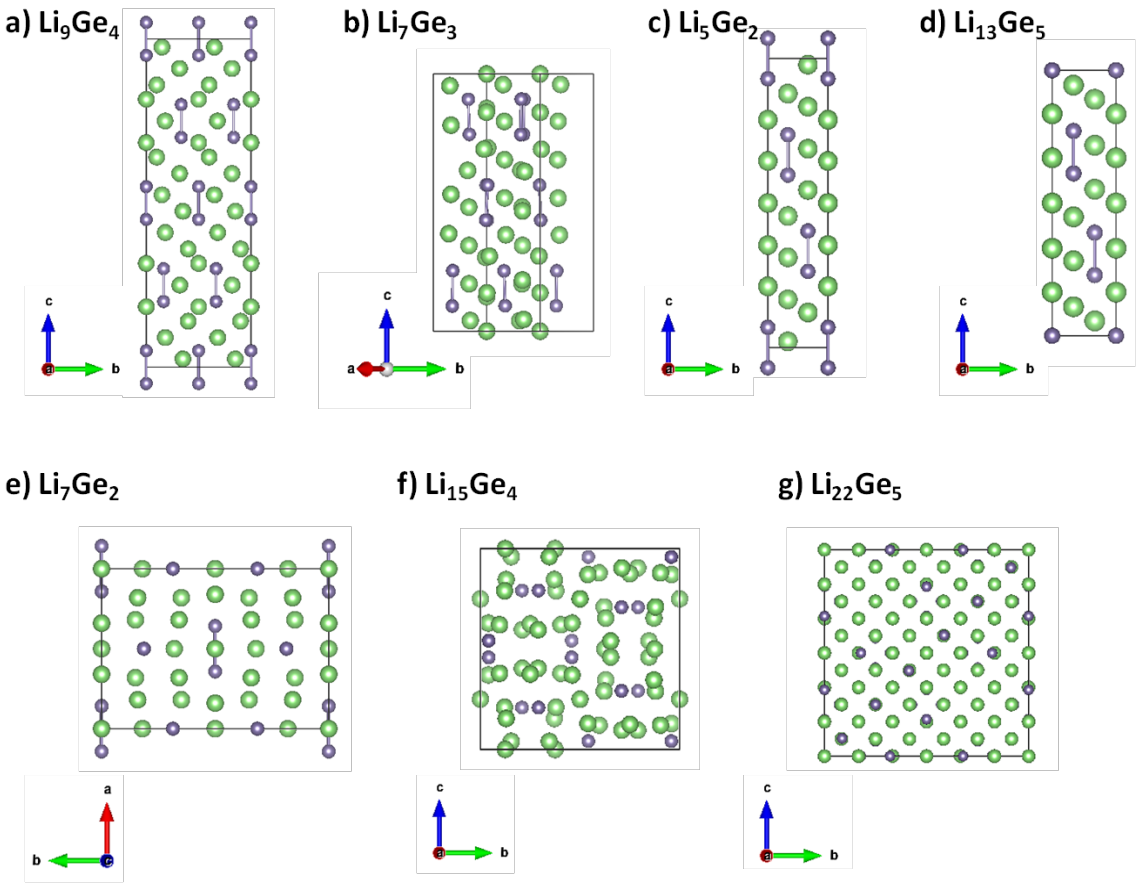

Figure 1.5. Structures of key Li_xGe crystalline phases investigated as part of this thesis a) Li_9Ge_4 ($Li_{2.25}Ge$, space group, *Cmcm*, PDF#01-073-6200[54]); b) Li_7Ge_3 ($Li_{2.33}Ge$, *P* 32_12)[11]; c) Li_5Ge_2 ($Li_{2.5}Ge$, $R\bar{3}m$)[11]; d) $Li_{13}Ge_5$ ($Li_{2.6}Ge$, $P\bar{3}m1$)[11]; e) Li_7Ge_2 ($Li_{3.5}Ge$, *Cmmm*, PDF # 00-029-0636[50]); f) $Li_{15}Ge_4$ ($Li_{3.75}Ge$, $I\bar{4}3d$, PDF # 01-089-3034[55]); g) $Li_{22}Ge_5$ ($Li_{4.4}Ge$, $F\bar{4}3m$, PDF #00-017-0402[56]). Green and blue spheres denote Li and Ge atoms, respectively, the blue lines indicating Ge-Ge bonds in the Ge dumbbells.

1.1.5. Tin (Sn)

Tin based materials are also very attractive as anode due to their high energy densities[57,58] and have slightly higher operating potentials compared to graphite, which reduces the safety issues associated with metallic lithium deposition.[22] Tin undergoes a reversible alloying process with lithium and exhibits a high theoretical capacity of 993 mAh/g.[6]

During electrochemical cycling, each Sn theoretically can take up 4.4 Li atoms to form a $Li_{4.4}Sn$ alloy phase, but the associated volume expansion is approximately 260%, which can cause cracking and a loss of reversible capacity.[5] When Sn reacts with lithium, Sn forms several Li-Sn alloy phases, which have different lattice parameters and structures. Therefore, stress occurs while converting from one phase to the other. This stress is usually released by cracking or fragmentation of the Sn particles[5]. To overcome the problem of the huge volume change, various approaches have been reported to improve the cycling stability of tin. Multiphase composites, such as using inactive matrix or carbon based composite and nano-structured/ nano composite materials are being widely explored for the next-generation LIBs.[6]

In 1997, Fuji used the concept of a buffer matrix and announced a new material which they called STALION, an amorphous tin composite oxide (ATCO), as a negative electrode.[3] During the first cycle, lithium reacts with oxygen from tin oxide to form Li_2O and metallic tin. The tin phase is finely dispersed in the Li_2O matrix and prevents the aggregation of the Sn particles. The electrochemically inactive Li_2O plays as a role of "a buffer matrix" to support the structure while metallic tin undergoes Li-Sn alloying /dealloying process reversibly.

The basic reaction scheme is shown below:[9]

$$SnO_2 + 4Li^+ + 4e^- \rightarrow Sn + 2Li_2O \quad [1.2]$$

$$Sn + 2Li_2O + 4.4Li^+ + 4.4e^- \Leftrightarrow 2Li_{4.4}Sn + 2Li2O \quad [1.3]$$

$$SnO + 2Li^+ + 2e^- \rightarrow Sn + Li_2O + 4.4Li^+ + 4.4e^- \quad [1.4]$$

$$Sn + Li_2O + 4.4Li^+ + 4.4e^- \Leftrightarrow Li_{4.4}Sn + Li_2O \quad [1.5]$$

However STALION was not used commercially because of poor cyclability and a large irreversible capacity loss during the first cycle due to the formation of Li_2O.

In 2005, Sony introduced the "Nexelion" battery, the first commercial Sn-based (an amorphous Sn-Co-C composite) negative electrode battery. It was announced that Nexelion had 30% more capacity than a conventional battery.[59] Carbon is used as a conductive matrix, with nanosized Sn-Co nanoparticles embedded in it.[60] The amorphous Sn-Co-C material has approximately the same local bonding structure as the crystalline Sn-Co phase (hexagonal, *P6/mmm*).[61] The electrochemical properties show a smooth charge/discharge curve indicating that only a single solid-solution process occurs. There is no significant evidence of Sn aggregation as seen in tin or tin oxide based materials.[62] In addition, this material has good capacity retention over 40 cycles. This suggests that nanosized Sn-Co particles are well dispersed in the carbon matrix. During lithiation and delithiation, the volume expansion and contraction appear to be absorbed by the carbon matrix without cracking and aggregation of the Sn particles. Since then, several groups have investigated different synthesis approaches and electrochemical mechanisms, but lithiation mechanisms are still under debate. Thus, a more detailed characterization of the Li-Sn alloys is required to understand the electrochemical mechanisms.

The known binary phase diagram of the Li-Sn system[42,63] consists of seven experimentally reported crystalline phases: Li_2Sn_5, LiSn, Li_7Sn_3, Li_5Sn_2, $Li_{13}Sn_5$, Li_7Sn_2, and $Li_{22}Sn_5$, whose structures have been characterized by X-ray diffraction (XRD).[64-71] The crystal structures of the relevant Li_xSn_y compounds proposed to form in electrochemical processes are shown in Figure 1.6. Sn-rich compounds (Li_2Sn_5 and LiSn) have a two or a three dimensional lattice structure based on Sn-Sn bonds. The Sn richest compound, Li_2Sn_5,[64] adopts *P*4/*mbm* symmetry with 1 Li and 2 Sn crystallographic sites. Sn-Sn bonds (3.1~3.3Å) form a three dimensional Sn network structure with lithium isolated by the Sn network. LiSn[65] (*P*2/*m*) contains a two dimensional layered Sn structure (Sn-Sn bond distance of ~3.1 Å) with 2 Li and 2 Sn crystallographic sites.

Li-rich compounds (Li_7Sn_3, Li_5Sn_2, $Li_{13}Sn_5$, and Li_7Sn_2) mainly contain Sn-Sn dimer or trimer structures. Li_7Sn_3[66], (or $Li_{2.33}Sn$) adopts a P_12_1/m space group with 7 Li and 3 Sn crystallographic sites. The Sn atoms form Sn-Sn-Sn trimers with Sn-Sn

distances of 2.94 Å. Li_5Sn_2 ($R\bar{3}m$), $Li_{13}Sn_5$ ($P\bar{3}m1$), and Li_7Sn_2 ($Cmmm$) all contain Sn-Sn dumbbell structures, which are aligned in parallel rows, analogous to Li_5Si_2 ($R\bar{3}m$), $Li_{13}Si_4$ ($P\bar{3}m1$) in the Li-Si system and Li_5Ge_2 ($R\bar{3}m$), $Li_{13}Ge_5$ ($P\bar{3}m1$), Li_7Ge_2 ($Cmmm$) in the Li-Ge system.[11] Li_5Sn_2[67] (or $Li_{2.5}Sn$) has $R\bar{3}m$ symmetry with 3 Li and 1 Sn crystallographic sites. The Sn atoms exist as Sn-Sn dumbbells (Sn-Sn bond distance of 2.88Å), separated by 5 Li atoms along the c-axis. $Li_{13}Sn_5$[68] (or $Li_{2.6}Sn$, space group, $P\bar{3}m1$) contains Sn-Sn dumbbells and isolated Sn atoms. The isolated Sn atoms in this material are separated by 5 Li atoms, while the Sn-Sn dumbbells with a bond distance of 2.86Å are separated by 4 Li atoms along the c-axis. Li_7Sn_2 with symmetry of $Cmmm$[69] has Sn-Sn dumbbells and isolated Sn atoms, where 50% of the Sn atoms are present as dumbbells. The crystal structure comprises columns along the a-axis; one sixth of these columns contain Sn-Sn dumbbells (with bond length 2.99 Å) separated by one Li atom, while one third of the columns contain isolated Sn with 2 Li atoms in between, the rest of the columns containing only Li atoms.

The Li-richest compound that has been reported is $Li_{22}Sn_5$ (or $Li_{4.4}Sn$; space group: $F23$, analogous to the $Li_{22}Pb_5$ structure type). It contains only isolated Sn atoms in a matrix of Li with 16 Li and 4 Sn crystallographic sites on the basis of X-ray powder film analysis.[71,72] Nesper *et al.*[73] reinvestigated the $Li_{4.4}Sn$ phase by means of X-ray single-crystal diffraction and suggested a new structure type ($Li_{21}Si_5$ structure type) with a higher symmetry space group ($F\bar{4}3m$). Goward *et al.*[74] studied the family of $Li_{21}X_5$ phases (X = Si, Ge, Sn, and Pb) and reformulated the composition and structure as $Li_{17}X_4$ with $F\bar{4}3m$ symmetry for X=Ge, Sn and Pb. More recently, Lupu *et al.*[75], in an X-ray single crystal and a neutron powder diffraction study, identified well-defined lithium positions in $Li_{17}Sn_4$, the structure containing 13 Li and 4 Sn crystallographic sites. They performed transport measurements for this phase, reporting poor metallic behavior similar to that of heavily doped semiconductors. However, previous NMR studies have reported large ^{7}Li Knight shifts (see section 1.2.3) for the "$Li_{21}Sn_5$" phase (of ~60 – 100 ppm), suggesting that these phases are metallic. There seems to be a contradiction between the electronic properties reported for what is nominally this phase – and there

appear to be at least two compositions, presumably $Li_{21}Sn_5$ and $Li_{17}Sn_4$. This will be discussed further in chapter 5.

Dunlap *et al*.[76] and Robert *et al*.[77] investigated the known Li-Sn phases by means of ^{119}Sn Mössbauer spectroscopy. Sn-rich compounds (Li_2Sn_5 and LiSn) and Li-rich compounds (Li_7Sn_3, Li_5Sn_2, $Li_{13}Sn_5$, Li_7Sn_2 and $Li_{22}Sn_5$) are clearly distinguished by their isomer shift (δ) and quadropole splitting (Δ). The isomer shift (δ) is intimately related to 5s electron density of a Sn nucleus and the quadropole splitting (Δ) is associated with the asymmetry of the electron distribution around the Sn nucleus.[77] The Sn-rich compounds have a two or a three dimensional Sn network structure, as shown in Figure 1.6, so isomer shift values appear in a similar range to β-Sn (2.56 to 2.34 mm/s), while Li-rich compounds have isolated Sn or small Sn clusters (dumbbell or triatomic structure) and show a large decrease of isomer shift (2.07 to 1.83 mm/s) due to a smaller contribution from the Sn network structure.[77] They suggested that a (Δ-δ) correlation diagram could be used to identify the Li-Sn phases during electrochemical lithiation.

A ^{119}Sn solid-state nuclear magnetic resonance (NMR) study of LiSn by Haarmann *et al*.[78] reported a large Knight shift of about 5400 ppm. The Knight shift occurs when the nuclear spin can interact with conduction electrons and will be discussed further in Section 1.2.3. The assignment of the resonance as at Knight shift is supported by calculations of the total electronic density of states (DOS) of LiSn.[79]

Bekaert *et al.*[80], in a high resolution MAS ^{7}Li NMR study and electronic structure calculations with DFT of Li-Sn model compounds, determined ^{7}Li NMR shifts of each model compound and demonstrated a good correlation between the participation of the Li to the DOS at the Fermi level and the corresponding ^{7}Li NMR shifts.

The aim of this study is to better understand the electronic and local structures of Li-Sn model compounds via XRD, PDF and ^{7}Li/^{119}Sn NMR analysis. This will be used to investigate and characterize electrochemically lithiated Li-Sn phases. Relevant Li_xSn_y model compounds (with nominal compositions Li_2Sn_5, LiSn, Li_7Sn_3, Li_7Sn_2, and $Li_{22}Sn_5$) have been prepared by solid-state synthesis and electrochemical lithiation and characterized by XRD, solid-state NMR and PDF analysis to assist with the identification

and structural determination of the Li_xSn_y phases that form during electrochemical lithiation.

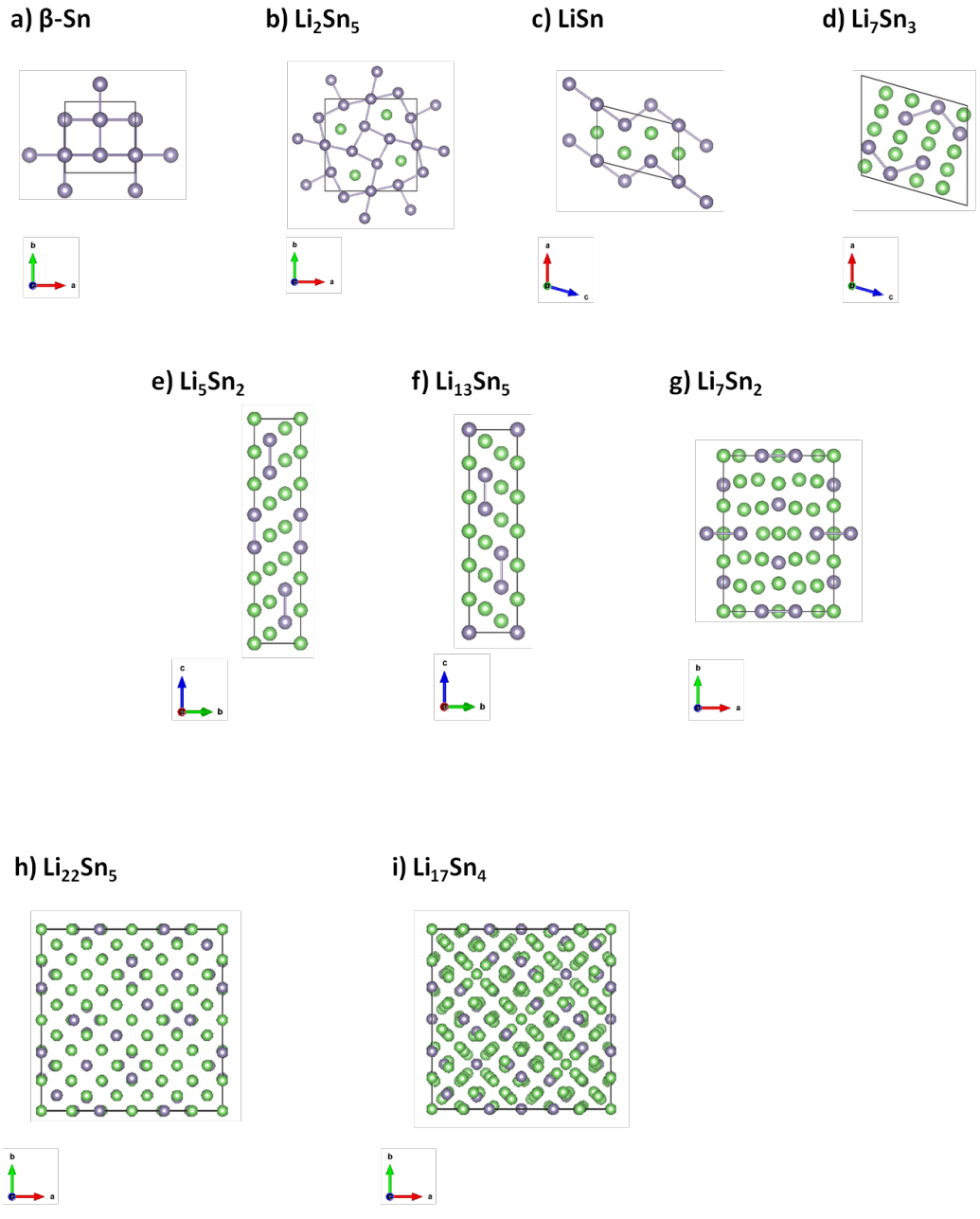

Figure 1.6. Structures of key Li_xSn_y crystalline phases investigated as part of this work a) β-Sn (space group, $I\,4_1/a\,m\,d$)[81]; b) Li_2Sn_5 ($Li_{0.4}Sn$, $P4/mbm$)[22]; c) LiSn (LiSn, $P2/m$)[82]; d) Li_7Sn_3 ($Li_{2.33}Sn$, P_12_1/m)[66] ; e) Li_5Sn_2 ($Li_{2.5}Sn$, $R\bar{3}m$)[67]; f) $Li_{13}Sn_5$ ($Li_{2.6}Sn$, $P\bar{3}m1$)[68]; g) Li_7Sn_2 ($Li_{3.5}Sn$, *Cmmm)*[69]; h) $Li_{22}Sn_5$ ($Li_{4.4}$ Sn $F\bar{4}3m$)[67]; i) $Li_{17}Sn_4$ ($Li_{4.25}Sn$, $F\bar{4}3m$,)[75]. Green and blue spheres denote Li and Sn atoms, respectively, the blue lines indicating Sn-Sn bonds.

1.2. Solid state nuclear magnetic resonance (NMR)

Solid state NMR is a powerful technique for probing the local structures and electronic properties of electrode materials for LIBs. Solid-state NMR is an element-specific technique that is very sensitive to the local environment of the nucleus probed, in this thesis ^{7}Li and ^{119}Sn. Since lithium ions are directly involved in the electrochemical reactions, *in-* and *ex-situ* solid-state ^{7}Li NMR experiments are employed to help identify the local structures formed in disordered phases, the method having been shown to be highly sensitive to local structure and deviations from stoichiometry of the crystalline phases in the lithium-silicon system.[16,17,83]

The total interaction energy of nuclear spins can be expressed as the sum of each individual interaction; [84]

$$\hat{H}_{tot}=\hat{H}_Z + \hat{H}_{CS} + \hat{H}_D + \hat{H}_J + \hat{H}_Q + \hat{H}_{P,} \qquad [1.6]$$

where $\hat{H}_Z$ is the Zeeman interaction, $\hat{H}_{CS}$ is the chemical shift, $\hat{H}_D$ is the dipolar coupling, $\hat{H}_J$ is the J-coupling, $\hat{H}_Q$ is the quadrupolar coupling, and $\hat{H}_P$ is the paramagnetic interactions (the interaction between a nuclear spin and unpaired electrons: dipolar coupling, Fermi-contact shift, and pseudo-contact shift). $\hat{H}_Z$ is the external Hamiltonian, which depends on the external magnetic field. The rest of the Hamiltonians represent internal spin interactions.

1.2.1. The chemical shielding (shift)

The chemical shift in NMR is significantly important, as it gives valuable information about the local environments surrounding the nucleus. When a molecule is placed in an external magnetic filed $\boldsymbol{B_0}$, the electrons in the molecules cause an induced local magnetic (shielding) field. This induced field leads to a change in the total magnetic field experienced by the nucleus. The chemical shielding interaction can be given as follows:[85]

$$H_{CS} = -\gamma\hbar \cdot \hat{I} \cdot \boldsymbol{\sigma} \cdot \boldsymbol{B}_0, \qquad [1.7]$$

where σ is the chemical shielding tensor, which describes the orientation dependent interaction between two vectors. The effective magnetic field ($\boldsymbol{B_{eff}}$) experienced by the nucleus is smaller than the applied field ($\boldsymbol{B_0}$);

$$\boldsymbol{B_{eff}} = (1 - \boldsymbol{\sigma})\boldsymbol{B}_0 \qquad [1.8]$$

In practical NMR experiments, the absolute chemical shielding (σ) is difficult to measure and thus is converted into a more convenient form, a chemical shift δ (in ppm units), which is given by;

$$\delta = 10^6(\sigma_{\text{ref}} - \sigma_{\text{sample}}), \qquad [1.9]$$

where σ_{ref} is the shielding of the same type of nucleus in a model compound.

The chemical shielding tensor (σ) is a 3x3 second rank tensor with diagonal elements σ_{11}, σ_{22}, and σ_{33} in the principal axis system.[86] These tensors can be rewritten using as chemical shift, δ, with the Haeberlen convention.[87] The isotropic chemical shift, δ_{iso}, chemical shift anisotropy, δ_{aniso}, and chemical shift asymmetry (CSA), η_{cs}, parameters are defined as:

$$\delta_{\text{iso}} = \frac{\delta_{11} + \delta_{22} + \delta_{33}}{3}, \qquad [1.10]$$

$$\delta_{\text{aniso}} = \delta_{33} - \delta_{\text{iso}}, \qquad [1.11]$$

$$\eta_{cs} = \frac{\delta_{22} - \delta_{11}}{\delta_{\text{aniso}}}, \qquad [1.12]$$

where δ_{11}, δ_{22}, and δ_{33} are the principal components of the chemical shift tensor in the order of $\delta_{11} \geq \delta_{22} \geq \delta_{33}$ (*i.e.,* $\approx \sigma_{33} \geq \sigma_{22} \geq \sigma_{11}$) and $|\delta_{33} - \delta_{iso}| \geq |\delta_{11} - \delta_{iso}| \geq |\delta_{22} - \delta_{iso}|$. The anisotropic

parameters, δ_{aniso} and η_{cs}, lead to a broadening that arises from asymmetry in the electron density surrounding a given nucleus. In liquids, an average chemical shift is observed due to averaging over all orientations on a timescale short in comparison with the NMR measurement time. In solids, a complex line shape results from a sum of all possible chemical shifts. Therefore, a broad NMR spectrum is an example of inhomogeneous broadening arising from CSA. The CSA patterns are described by the principal components of the chemical shift tensor, thus fitting the pattern can deduce the defined NMR parameters (δ_{iso}, δ_{aniso}, and η_{cs}(Figure 1.7) These parameters provide important crystallographic information and also help to understand electronic structure at the nucleus.

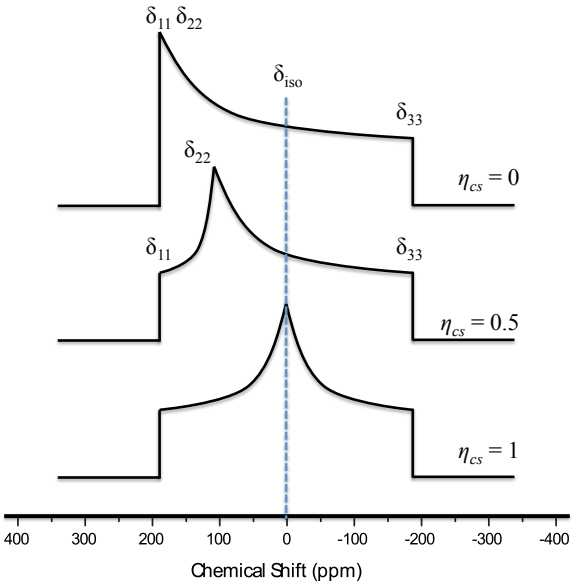

Figure 1.7. Typical CSA patterns for different η_{cs} values. Figure reproduced from Spin Dynamics.[84]

1.2.2. Magic-Angle Spinning (MAS) NMR

In liquids, rapid molecular tumbling leads to an averaging of the anisotropic interactions, such as dipolar coupling and chemical shift anisotropy, resulting in narrow resonance line shapes in the NMR spectra. In solid-state NMR, the lack of molecular motion results in spectral line broadening of NMR spectra due to the orientation dependent interactions. The spatial dependence of the dipolar coupling and CSA interaction both contain a common term; [84]

$$\frac{1}{2}(3cos^2\theta - 1) \qquad [1.13]$$

For solid samples, magic-angle spinning (MAS) was introduced to eliminate these orientation dependent interactions (dipolar coupling and CSA) by rotating the sample rotor at an angle θ (54.74°) with respect to the external field $\mathbf{B}_0$ (Fig.1.8). If the spinning frequency is much larger than the frequency of the anisotropic interactions, it will lead to a single sharp single resonance corresponding to the isotropic chemical shift in liquid states. When the MAS frequency is less than the magnitude of anisotropic interactions, the NMR spectrum contains extra peaks (spinning side bands) due to the remaining interactions. Each spinning side band is separated from the isotropic peak in intervals of the spinning speed.

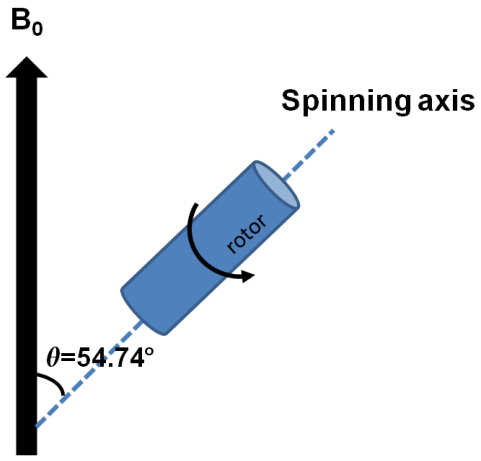

Figure 1.8. The magic-angle spinning (MAS) experiment. The rotor is spun about an axis, at the magic angle (θ=54.74°), with the respect to the external field, $\mathbf{B}_0$.

1.2.3. Knight shift

In metals, intermetallics and alloy materials, the interaction of a nuclear spin with conduction electrons affects the frequency of resonance, inducing a shift referred to as the Knight shift. The Knight shift is a type of Fermi-Contact shift and is described by,

$$K = \frac{8\pi}{3}\langle|\Psi_{r=0}|^2\rangle\,\chi_s^e, \qquad [1.14]$$

where $\langle|\Psi_{r=0)}|^2\rangle$ is the electronic density of conduction electrons at the nucleus of *s* electrons on the Fermi surface and χ_s^e is the electron spin susceptibility.[80]

Thus, the Knight shift is proportional to the s-electron density at the Fermi level, so the fractional shift only increases with nuclear charge. These interactions give rise to a large positive shift and are temperature independent.[84] ^{7}Li metal has a comparatively small Knight shift (0.0261%, approximately 260 ppm) due to the small nuclear charge.

1.3. Pair distribution function (PDF) analysis

Pair distribution function (PDF) analysis is a total scattering method, utilizing Bragg scattering and diffuse scattering in equal weighting. Thus, this is a particularly powerful technique for characterizing amorphous or nano-crystalline materials.[88]

A PDF provides a weighted atom-atom distance histogram in real-space; examination of peak positions gives information about bond-distances or larger atom-atom separations, peak intensity and area information about coordination number. The extent of well-defined peaks in a PDF corresponds to the length scale over which the structure is ordered. Using least-squares refinements against known crystallographic models, the phase fraction and unit cell information for the different chemical phases can be extracted. The intensity of peaks in the PDF is weighted by scattering amplitude of the atoms in each pair of atoms. X-rays are more sensitive to heavier elements; therefore this technique is particularly sensitive to Ge or Sn connectivity (Ge-Ge/Sn-Sn and Ge-Li/Sn-Li bonding) in the materials in this thesis.

1.3.1 Obtaining the PDF

The PDF can be obtained from the measured scattering intensity and the overall experimental scattering intensity has several components;

$$I_{tot}(Q) = I_{coh}(Q) + I_{incoh}(Q) + I_{MS}(Q) + I_{BG}(Q) \qquad [1.15]$$

where $I_{tot}(Q)$ is the total scattering, $I_{coh}(Q)$ is the coherent scattering, $I_{incoh}(Q)$ is the incoherent scattering, $I_{MS}(Q)$ is the multiple scattering, and $I_{BG}(Q)$ is the background scattering intensity. $I_{coh}(Q)$ only contains structural information, so the rest of the scattering intensities are removed by various correction steps. The total scattering structure function, $S(Q)$, is derived from the coherent part of the total diffraction intensity;[89]

$$S(Q) = \frac{I_{coh}(Q) - \sum c_i |f_i(Q)|^2}{|\sum c_i f_i(Q)|^2} + 1, \qquad [1.16]$$

where c_i is the number or concentration of atomic species i, and f_i is the atomic form factor of atomic species i. This normalized scattering structure function ($S(Q)$) is Fourier transformed to obtain the PDF, G(r), which contains information regarding the atomic correlations,

$$G(r) = \frac{2}{\pi}\int_0^{\infty} Q[S(Q) - 1]\, sin(Qr)\, dQ. \qquad [1.17]$$

$G(r)$ can also be defined as,

$$G(r) = 4\pi r\left[\rho_{(r)} - \rho_0\right], \qquad [1.18]$$

where r is the inter-nuclear distance, $\rho_{(r)}$ is the local number density and $\rho_{(0)}$ is the average number density. This gives the probability of finding two atoms at a distance r from each other.

1.3.2 Experimental aspects

There are mainly three factors that influence the quality of the experimental PDF: Fourier termination errors, resolution and counting statistics. Fourier termination ripples can be minimized by collecting total scattering with a higher Q-range.[90] The Q, the magnitude of the scattering vector, is determined by the wavelength,

$$Q = \frac{4\pi \sin\Theta}{\lambda} \qquad [1.19]$$

where θ is the scattering angle and λ is the wavelength of the x-ray source. Higher Q values lead to higher-real space resolution data, thus the PDF data needs to be collected by a synchrotron x-ray source to obtain higher Q.

1.3.3. PDF refinement

Once PDF data is obtained, information can be extracted directly in several ways.[91] The first peak position is an indication for the nearest neighbor distance and, as r increases, each peak position represents another atom-atom distance. The peak-integrated area can be used to determine the coordination number of the atom. The peak width indicates a thermal or static disorder. However, refinement of a structural model will be desired to get much more information. The calculated PDFs from a structural model, which can be compared with the experimental PDF data, can be obtained, using this relation:[90]

$$G_{cal}(r) = \frac{1}{r}\sum_i \sum_j \left[\frac{b_i b_j}{\langle b \rangle^2}\delta(r - r_{ij})\right] - 4\pi r \rho_0, \qquad [1.20]$$

where the sum goes over all pairs of atoms *i* and *j* separated by distance r_{ij}. The scattering power of atom *i* is given by the value of b_i and <*b*> is the average scattering power of the sample.

The experimental PDF data can be refined in an analogous manner as the Rietveld method using the program PDFFit2 with graphical user interface PDFGui.[92] The refinement of the PDF based on a structural model can be carried out until the difference between the model and the experimental data is minimized. The goodness of fit can be calculated from Eq. 1.21,

$$R_w = \left\{\frac{\sum w_i(r_i)\left(G_{exp}(r_i) - G_{cal}(r_i)\right)^2}{\sum w_i(r_i)\left(G_{exp}(r_i)\right)^2}\right\}^{\frac{1}{2}}, \qquad [1.21]$$

where G_{exp} and G_{cal} stand for the experimental and calculated PDFs, respectively.

R_w-factors for PDF refinements are generally higher than expected in a Rietveld refinement because the functions, which are being fit, are significantly different and cannot be compared. The residual is, however, useful as a measure of goodness of fit when comparing models fit to PDF data.

1.4. References

(1) Palacin, M. R. *Chem.soc.rev* **2009**, *38*, 2565.

(2) Ferguson, P. P.; Todd, A. D. W.; Dahn, J. R. *Electrochem. Commun.* **2008**, *10*, 25.

(3) Tarascon, J. M.; Armand, M. *Nature* **2001**, *414*, 359.

(4) Kim, T.-H.; Park, J.-S.; Chang, S. K.; Choi, S.; Ryu, J. H.; Song, H.-K. *Adv. Eng. Mater.* **2012**, *2*, 860.

(5) Park, C. M.; Kim, J. H.; Kim, H.; Sohn, H. J. *Chem. Soc. Rev.* **2010**, *39*, 3115.

(6) Zhang, W.-J. *J. Power Sources* **2011**, *196*, 13.

(7) Obrovac, M. N.; Christensen, L. *Electrochem. Solid-State Lett* **2004**, *7*, A93.

(8) Seng, K. H.; Park, M. H.; Guo, Z. P.; Liu, H. K.; Cho, J. *Nano Lett* **2013**, *13*, 1230.

(9) Park, C.-M.; Kim, J.-H.; Kim, H.; Sohn, H.-J. *Chem.soc.rev* **2010**, *39*, 315.

(10) Kasavajjula, U.; Wang, C.; Appleby, A. J. *J. Power Sources* **2007**, *163*, 1003.

(11) Morris, A. J.; Grey, C. P.; Pickard, C. J. *Phys. Rev. B: Condens. Matter Mater. Phys.* **2014**, *90*, 054111.

(12) Chan, C. K.; Zhang, X. F.; Cui, Y. *Nano Letters* **2007**, *8*, 307.

(13) Winter, M.; Besenhard, J. O. *Electrochimica Acta* **1999**, *45*, 31.

(14) Zhang, J.; Xia, Y. *J. Electrochem.Soc.* **2006**, *153*, A1466.

(15) Li, H.; Shi, L.; Lu, W.; Huang, X.; Chen, L. *J..Electrochem. Soc.* **2001**, *148*, A915.

(16) Key, B.; Bhattacharyya, R.; Morcrette, M.; Seznéc, V.; Tarascon, J.-M.; Grey, C. P. *J. Am.Chem. Soc.* **2009**, *131*, 9239.

(17) Ogata, K.; Salager, E.; Kerr, C. J.; Fraser, A. E.; Ducati, C.; Morris, A. J.; Hofmann, S.; Grey, C. P. *Nat. Commun.* **2014**, *5*, 3217.

(18) Zhang, X. W. e. a. *J. Power Sources* **2004**, *125*, 206.

(19) Magasinski, A. e. a. *Nat. Mater.* **2010**, *9*, 353.

(20) Hu, L. B. e. a. *Chem. Commun.* **2011**, *47*, 367.

(21) Cui, L. F., Ruffo, R., Chan, C. K., Peng, H. L. & Cui, Y. *Nano Lett.* **2009**, *9*, 491.

(22) Chen, J. *Materials* **2013**, *6*, 156.

(23) Lim, L. Y.; Liu, N.; Cui, Y.; Toney, M. F. *Chem. Mater.* **2014**, *26*, 3739.

(24) Fuller, C.; Ditzenberger, J. *Physical Review* **1953**, *91*, 193.

(25) Wang, D. W.; Chang, Y. L.; Wang, Q.; Cao, J.; Farmer, D. B.; Gordon, R. G.; Dai, H. J. *J. Am.Chem.Soc.* **2004**, *126*, 11602.

(26) Li, D.; Seng, K. H.; Shi, D.; Chen, Z.; Liu, H. K.; Guo, Z. *J. Mater. Chem. A* **2013**, *1*, 14115.

(27) Cui, G. G., L.; Zhi, L.; Kaskhedikar, N.; van Aken, P. A.; Muellen, K.; Maier *J. Adv. Mater.* **2008**, *20*, 3079.

(28) Lee, H.; Kim, M. G.; Choi, C. H.; Sun, Y. K.; Yoon, C. S.; Cho, J. *J. Phys. Chem. B* **2005**, *109*, 20719.

(29) Seo, M. H.; Park, M. H.; Lee, K. T.; Kim, K.; Kim, J. H.; Cho, J. *Energy Environ. Sci.* **2011**, *4*, 425.

(30) C. K. Chan; X. F. Zhang; Y. Cui *Nano Lett.* **2008**, *8*, 307.

(31) Ko, Y. D.; Kang, J. G.; Lee, G. H.; Park, J. G.; Park, K. S.; Jin, Y. H.; Kim, D. W. *Nanoscale* **2011**, *3*, 3371.

(32) Cui, G. G., L.; Kaskhedikar, N.; van Aken, P. A.; Maier, J. *Electrochim Acta* **2010**, *55*, 985.

(33) Park, M. H.; Cho, Y.; K. Kim; J. Kim; M. L. Liu; Cho, J. *Angew. Chem.* **2011**, *123*, 9821.

(34) Jia , H.; Kloepsch, R.; He , X.; Badillo, J. P.; Gao, P.; Fromm, O.; Placke, T.; Winter, M. *Chem. mater.* **2014**, *26*, 5683.

(35) Yang, L. C.; Gao, Q. S.; Li, L.; Tang, Y. D.; Wu, Y. P. *Electrochem. Commun.* **2010**, *12*.

(36) Park, M. H.; Kim, K.; Kim, J.; Cho, J. *Adv. Mater.* **2010**, *22*, 415.

(37) Lee, H.; Cho, J. *Nano Lett.* **2007,**, *7,* , 2638.

(38) Kim, M. G. C., J. *J. Electrochem. Soc.* **2009,** , *156,*, A277.

(39) Seng, K. H.; Park, M.-H.; Guo, Z. P. L., H. K.; Cho, J. *Angew. Chem.Int. Ed.* **2012**, *51*, 5657.

(40) DiLeo, R. A. F., S.; Ganter, M. J.; Rogers, R. E.; Raffaelle, R. P.; Landi, B. J. *J. Phys. Chem. C* **2011**, *115*, 22609.

(41) Wang, X.-L.; Han, W.-Q.; H. Chen; Bai, J.; Tyson, T. A.; Yu, X.-Q.; Wang, X.-J.; Yang, X.-Q. *J. Am. Chem. Soc.* **2011,** , *133,* , 20692.

(42) Sangster, J.; Pelton, A. D. *J. Phase Equilib.* **1997**, *18*, 289.

(43) Grüttner, A.; Nesper, R.; Von Schnering, H. G. *Angew. Chem., Int. Ed.* **1982**, *21*, 912.

(44) Grüttner, A.; Nesper, R.; Von Schnering, H. G. *Acta. Crystallogr.* **1981**, *A37 (Suppl)*, C.

(45) Jain, A.; Kawasako, E.; Miyaoka, H.; Ma, T.; Isobe, S.; Ichikawa, T.; Kojima, Y. *J. Phys. Chem. C* **2013**, *117*, 5650.

(46) Dupke, S.; Langer, T.; Pottgen, R.; Winter, M.; Eckert, H. *Solid State Nucl. Magn. Reson.* **2012**, *42*, 17.

(47) Pickard, C. J.; Needs, R. J. *Phys. Rev. Lett* **2006**, *97*, 045504.

(48) Pickard, C. J.; Needs, R. J. *J. Phys.: Condens. Matter* **2011**, *23*, 053201

(49) Yoon, S.; Park, C.-M.; Sohn, H.-J. *Electrochem. Solid-State Lett.* **2008**, *11*, A42.

(50) Hopf, V.; Müller, W.; Schäfer, H. *Z. Naturforsch., B: Chem. Sci.* **1972**, *27*, 1157.

(51) Gladyshevskii, E. I.; Oleksiv, G. I.; Kripyake, P. I. *Sov. Phys. Crystallogr* **1964**, *9*, 269.

(52) Tipton, W. W.; Matulis, C. A.; Hennig, R. G. *Comp. Mater. Sci.* **2014**, *93*, 133.

(53) Nesper, R. *Prog. Solid State Chem.* **1990**, *20* 1.

(54) Hopf, V.; Schäfer, H.; Weiss, A. *Z. Naturforsch., B: Chem. Sci.* **1970**, *25*, 653.

(55) Johnson, Q.; Smith, G. S.; Wood, D. *Acta Crystallogr.* **1965**, *18*, 131.

(56) E. L. Gladyshevskii; G. I. Oleksiv; Kripyakevich, P. I. *Sov. Phys. Crystallogr.* **1964**, *9*, 269.
(57) Chevrier, V. L.; Ceder, G. *J. Electrochem.Soc.* **2011**, *158*, A1011.
(58) Wang, X. L.; Han, W. Q.; Chen, J.; Graetz, J. *ACS Appl. Mater. Interfaces* **2010**, *2*, 1548.
(59) http://www.sony.net/sonyinfo/news/press/200502/05-006e.
(60) Whittingham, M. S. *Dalton T.* **2008**, 5424.
(61) Zhang JJ, X. Y. *J. Electrochem.Soc.* **2006**, *153*, A1466.
(62) Todd, A. D. W.; Ferguson, P. P.; Fleischauer, M. D.; Dahn, J. R. *Int. J. Energ. Res.* **2010**, *34*, 535.
(63) Wen, C. J.; Hugglns, R. A. *J. Electrochem. Soc.* **1981**, *128*, 1181.
(64) Hansen, D. A.; Chang, L. J. *Acta Crystallogr.,Sect. B: Struct. Sci.* **1969**, *25*, 2392.
(65) Herbert Sch¨afer, B. E., and Wiking Muller *Angew. Chem., Int. Ed.* **1973**, *12*, 695.
(66) Müller, W. *Z. Naturforsch., B: J. Chem. Sci* **1974**, *29b*, 304.
(67) Frank, U.; Müller, W.; Schäfer, H. *Z. Naturforsch., B: J. Chem.*

1975, *30b*, 1.
(68) Frank, U.; Mülle, W. *Z. Naturforsch., B: J. Chem. Sci.* **1975**, *30b*, 316.
(69) Frank, U.; Müller, W.; Schäfer, H. *Z. Naturforsch., B: J. Chem.Sci*

1975, *30b*, 6.
(70) Gladyshevski, E. I. O., G. I.; Kripyakevich, P. I. *Kristallografiya* **1964**, *9*, 338.
(71) Gladyshevski, E. I. O., G. I.; Kripyakevich, P. I. *Sov. Phys. Crystallogr.* **1964**, *9*, 269.
(72) Zalkin, A.; Ramsey, W. J. *J. Phys. Chem. C* **1958**, *62*, 689.
(73) Nesper, R.; Schnering, H. G. *J. Solid State Chem.* **1987** *70* 48.
(74) Goward, G. R.; Taylor, N. J.; Souza, D. C. S.; Nazar, L. F. *J. alloy compd* **2001**, *329*, 82.
(75) Lupu, C.; Mao, J.-G.; Rabalais, J. W.; Guloy, A. M.; Richardson, J. W. *Inorg. Chem.* **2003**, *42*, 3765.
(76) Dunlap, R. A.; Small, D. A.; MacNeil, D. D.; Obrovac, M. N.; Dahn, J. R. *J. Alloys Compd.* **1999**, *289*, 135.
(77) Robert, F.; Lippens, P. E.; Olivier-Fourcade, J.; Jumas, J. C.; Gillot, F.; Morcrette, M.; Tarascon, J. M. *J. Solid State Chem.* **2007**, *180*, 339.
(78) Haarmann, F.; Grüner, D.; Bezugly, V.; Rosner, H.; Grin, Y. *Z. anorg. allg. Chem.* **2006**, *632*, 1423.
(79) Ienco, A.; Hoffmann, R.; Papoian, G. *J.Am.Chem. Soc.* **2001**, *123*, 2317.
(80) Bekaert , E.; Robert, F.; Lippens, P. E.; Ménétrier , M. *J. Phys. Chem. C* **2010**, *114*, 6749.
(81) Rönnebro, E.; Yin, J.; Kitano, A.; Wada, M.; Sakai, T. *Solid State Ionics* **2005**, *176*, 2749.
(82) Müller, W.; Schäfer, H. *Z. Naturforsch., B : J. Chem. Sci* **1973**, *28b*, 246.
(83) Key, B.; Morcrette, M.; Tarascon, J.-M.; Grey, C. P. *J.Am. Chem. Soc.* **2010**, *133*, 503.

(84) Levitt, M. *Spin Dynamics: Basics of Nuclear Magnetic Resonance*; Wiley, 2008.

(85) Duer, M. J. *Introduction to Solid-state NMR Spectroscopy*; Blackwell, 2004.

(86) MacKenzie, K. J. D.; Smith, M. E. *Multinuclear Solid-state NMR of Inorganic Materials*; Pergamon, 2002.

(87) Mehring, M. *Principles of High Resolution NMR Spectroscopy in Solids*; 2nd ed.; Springer-Verlag: Berlin, 1983.

(88) Chupas, P. J.; Chapman, K. W.; Chen, H.; Grey, C. P. *Catal. Today* **2009**, *145*, 213.

(89) Egami, T.; Billinge, S. *Underneath the Bragg Peaks*

Structural Analysis of Complex Materials; Oxford:Pergamon press, 2004.

(90) Proffen, T.; Billinge, S. J. L.; Egami , T.; Louca, D. *Z. Kristallogra* **2003**, *218*, 132.

(91) Dinnebier, R. E.; Billinge, S. J. L. *Powder diffraction : theory and practice,*; Royal Soc. Chem., Cambridge

, 2008.

(92) Farrow, C. L. J., P.; Liu, J. W.; Bryndin, D.; Bozǐ n, E. S.; 874; Bloch, J. P., T.; Billinge, S. J. L. ; 19 *J. Phys.: Condens. Matter.* **2007**, *19*, 875.

Chapter 2

Elucidation of the Local and Long-Range Structural Changes that Occur in Germanium Anodes in Lithium-Ion Batteries

This chapter formed the basis of the publication,

Jung, H.; Allan, P. K.; Hu, Y.-Y.; Borkiewicz, O. J.; Wang, X.-L.; Han, W.-Q.; Du, L.-S.; Pickard, C. J.; Chupas, P. J.; Chapman, K. W.; Morris, A. J.; Grey, C. P. *Chemistry of Materials* **2015**, *27*, 1031.

Abstract

Metallic germanium is a promising anode material in secondary lithium-ion batteries (LIBs) due to its high theoretical capacity (1623 mAh/g) and low operating voltage, coupled with the high lithium-ion diffusivity and electronic conductivity of lithiated Ge. Here, the lithiation mechanism of micron-sized Ge anodes has been investigated with X-ray diffraction (XRD), pair distribution function (PDF) analysis, and *in/ex situ* high-resolution ^{7}Li solid-state nuclear magnetic resonance (NMR), utilizing the structural information and spectroscopic fingerprints obtained by characterizing a series of relevant Li_xGe_y model compounds. In contrast to previous work, which postulated the formation of Li_9Ge_4 upon initial lithiation, we show that crystalline Ge first reacts to form a mixture of amorphous and crystalline Li_7Ge_3 (space group $P3_212$). On further lithiation, crystalline phase Li_7Ge_3 is formed, a phase that was proposed to be stable in a recent theoretical study of the Li-Ge phase diagram. (Morris, A. J.; Grey, C. P.; Pickard, C. J. *Phys. Rev. B: Condens. Matter Mater. Phys.* **2014**, *90*, 054111.). Further lithiation results in the transformation of Li_7Ge_3, via a series of disordered phases with related structural motifs, to form a phase that locally resembles Li_7Ge_2, a process that involves the gradual breakage of the Ge-Ge bonds in the Ge-Ge dimers (dumbbells) on lithiation. Crystalline $Li_{15}Ge_4$ then grows, an over-lithiated phase - $Li_{15+\delta}Ge_4$ - being formed at the end of discharge. This study provides comprehensive experimental evidence, by using techniques that probe short, medium and long range order, for the structural transformations that occur on electrochemical lithiation of Ge anodes; the results are consistent with corresponding theoretical studies regarding stable lithiated Li_xGe_y phases.

2.1 Introduction

Lithium-ion batteries (LIBs) are the current leading technology for electrochemical energy storage and are widely used in portable electronics. The rapidly growing demand for LIBs for use in electric vehicles and large-scale energy storage systems necessitates the search for new electrode materials with higher power and increased energy densities.[1] Silicon, germanium, and tin are attractive anode materials for LIBs due to their high energy densities.[2] These elements undergo alloying processes with Li, and exhibit much higher theoretical capacities - 3579, 1623 and 993 mAh/g for silicon, germanium, and tin, respectively - compared with graphite (375 mAh/g) [3,4], driving the capacity towards that achievable by using lithium-metal anodes whilst mitigating some of the safety issues of lithium-metal anodes.[5]

Of the aforementioned elements, the bulk of research has been focused on silicon anodes because they show the highest capacity among all anode materials except Li metal, Si also having high natural abundance and low cost. The more expensive germanium anode has received little attention. However, the lithium diffusivity in bulk Ge is 400 times higher than the lithium diffusivity in Si,[6] and the electronic conductivity of Ge is two orders of magnitude larger than Si due to its smaller band gap (E_g(Ge)=0.6 eV vs E_g(Si)=1.1 eV).[7] These properties lead to far superior rate performance for Ge anodes than Si anodes in LIBs [8].

Sangster et al. reported a binary phase diagram of the Li-Ge system consisting of seven experimentally reported crystalline phases: Li_7Ge_{12}, LiGe, $Li_{11}Ge_6$, Li_9Ge_4, Li_7Ge_2, $Li_{15}Ge_4$, and $Li_{22}Ge_5$.[9] In addition, $Li_{14}Ge_6$ (Li_7Ge_3) and $Li_{12}Ge_7$ [10,11,12,13] have been reported. Recent DFT calculations by some of us have shown that the Li-Ge phase diagram is extremely rich. LiGe($I4_1/a$), Li_7Ge_3 ($P32_12$), $Li_{13}Ge_5$($P\bar{3}\ m1$), Li_8Ge_3($R\bar{3}\ m$), $Li_{15}Ge_4$($I\bar{4}\ 3d$) and $Li_{17}Ge_4$($F\bar{4}\ 3m$), were identified via the combined random structure searching[14,15] and atomic species swapping method[16] to be stable (*i.e.*, lie on a convex hull between Li and Ge), while other Li_xGe_y alloys, including, Li_5Ge_2, and $Li_{13}Ge_4$[16], are only slightly metastable with respect to disproportionation to the thermodynamic phases and hence are likely to be also present at room temperature.

Several papers have reported the behaviour of Ge in LIB. St. John *et al*[17] reported five distinct two-phase plateaus in the discharge and charge electrochemical profiles of molten salt Ge-Li batteries between 360 °C and 440 °C and associated these plateaus with the formation of LiGe, Li_9Ge_4, $Li_{16}Ge_5$, $Li_{15}Ge_4$, and $Li_{22}Ge_5$, respectively. By analogy with Si[18,19], Ge may follow a different electrochemical lithiation pathway at room temperature, possibly involving the formation of metastable and amorphous phases. A number of mechanistic studies on the electrochemical lithiation process of Ge anodes at room temperature have been reported but no consensus on the lithiated phase formed has been reached. Several authors report the formation of $Li_{15}Ge_4$ at the end of lithiation[20-23], analogous to the final phase formed on fully discharging a silicon electrode. [18,24,25] However, $Li_{22}Ge_5$ has also been reported to form at the end of lithiation[26,27].

Graetz *et al.* [26], in an *ex-situ* X-ray diffraction (XRD) study of a thin-film Ge electrode, identified the Li-Ge crystallographic phases LiGe, Li_7Ge_2, and $Li_{15}Ge_4$, and also suggested that $Li_{11}Ge_6$, Li_9Ge_4 and $Li_{22}Ge_5$ may also form in small quantities during the electrode reactions. An *ex-situ* XRD study of an electrochemically lithiated Ge metal electrode by Kim *et al.*[20] indicated that $Li_{15}Ge_4$ was formed at the end of discharge. Yoon *et al.*[27] reported a three-step lithiation mechanism (Ge→ Li_9Ge_4→Li_7Ge_2→ $Li_{15}Ge_4$ +$Li_{22}Ge_5$) for a carbon-coated germanium composite electrode based on *ex-situ* XRD and HRTEM analyses. An *in-situ* XRD analysis of lithiated Ge films prepared by both evaporation and sputtering methods by Baggetto *et al.*[21] indicated that the lithiation process occurred via the formation of a series of amorphous Li-Ge intermediates, eventually forming the fully lithiated product crystalline $Li_{15}Ge_4$. Liu *et al* [22] investigated Ge nanowire electrodes by means of *in-situ* TEM and proposed a two-step lithiation process: Ge→ amorphous Li_xGe→ crystalline $Li_{15}Ge_4$. A more recent *in situ* XRD and X-ray absorption spectroscopy (XAS) studies[23] suggested that micron sized crystalline Ge particles are initially converted into amorphous phase resembling Li_9Ge_4 , "a-Li_9Ge_4"; subsequently the residual crystalline Ge forms amorphous Ge and amorphous Li_xGe phases (mixture of a-Li_9Ge_4, a-LiGe, and a-Li_7Ge_2, from EXAFS fitting), and eventually crystalline $Li_{15}Ge_4$. The Ge-Ge bond distances extracted from EXAFS measurements indicated that the mid-lithiation amorphous phases resemble Li_9Ge_4 at 253 mV and Li_7Ge_2 below 220 mV.

Given the complexity of the phase diagram and the uncertainties of the nature of some of the crystalline and amorphous phases formed, it is clear that further structural elucidation is required, with a focus on techniques that are able to characterize any amorphous or disordered intermediates. In this paper, we probe the structure of Ge-anodes at various stages of lithiation using XRD, X-ray pair-distribution function (PDF) analysis, and high-resolution ^{7}Li solid-state nuclear magnetic resonance (NMR) spectroscopy.

Pair-distribution function analysis utilizes the total scattering from the sample, treating the diffuse scattering and Bragg scattering in parallel. Thus, whilst any long-range order is accounted for in analysis, its presence is not required to obtain structural information. It is, therefore, a particularly powerful technique for characterizing materials in which there is a considerable degree of disorder. A PDF provides a weighted atom-atom distance histogram in real-space; examination of peak positions gives information about bond-distances or larger atom-atom separations, peak intensity and area information about coordination number. The extent of well-defined peaks in a PDF corresponds to the length scale over which the structure is ordered. Using least-squares refinements against known crystallographic models, the phase fraction and unit cell information for the different chemical phases can be extracted. The intensity of peaks in the PDF is weighted by scattering amplitude of the atoms in each pair of atoms. X-rays are more sensitive to heavier elements, therefore this technique is particularly sensitive to Ge connectivity (Ge-Ge and Ge-Li bonding) in the electrodes.

Solid-state NMR is an element-specific technique that is very sensitive to the local environment of the nucleus probed, in this case ^{7}Li. *In-* and *ex-situ* solid-state ^{7}Li NMR experiments are employed here to help identify the local structures formed in disordered phases, the method having been shown to be highly sensitive to local structure and deviations from stoichiometry of the crystalline phases in the lithium-silicon system.[18,19,28] The one previous ^{7}Li NMR report of the germanide, $Li_{12}Ge_7$ suggests that ^{7}Li NMR of these systems will be similarly sensitive to local structure and lithium dynamics.[13] Via these techniques we achieve a complementary study of the elements in

the electrode to obtain comprehensive insights into the structure Ge-anodes at various degrees of lithiation.

Relevant Li-Ge model compounds (with nominal compositions Li_9Ge_4, Li_7Ge_2, $Li_{15}Ge_4$, and $Li_{22}Ge_5$) have been synthesized and characterized by XRD, solid-state NMR and PDF analysis to assist with the identification and structural determination of the Li_xGe_y phases that form during electrochemical lithiation. Through the amalgamation of short-range and long-range structural information, we obtain a detailed structural model for how micron-sized germanium particles react to form a series of lithiated germanides, the final lithiation product corresponding to $Li_{15+x}Ge_4$.

2.2. Experimental section

2.2.1. Synthesis of model compounds

The lithium-germanium model compounds (with nominal stoichiometries, Li_9Ge_4, Li_7Ge_2, $Li_{15}Ge_4$ and $Li_{22}Ge_5$) were prepared by mechanical mixing. Stoichiometric amounts of lithium foil (Aldrich) and germanium metal (Alfa Aesar, 100 mesh, 99.999%) were mixed in a stainless steel ball mill jar in an Ar-filled glove box and ball milled for 8 hours in a SPEX SamplePrep8000 Mixer/Mill high energy ball mill. The final products were stored under Argon atmosphere before characterization.

2.2.2. Synthesis of micron-sized germanium

Micron-sized Ge powders were prepared by a 2-step procedure. GeO_2 nanoparticles were first prepared via hydrolysis of $GeCl_4$.[4] 2 ml $GeCl_4$ (99.99%, Alfa Aesar) was added to 8 ml anhydrous ethanol (99.9%, Sigma Aldrich) and the mixture was stirred for 10 minutes. In a separate beaker, 10 ml de-ionised water was added to 100 ml anhydrous ethanol and stirred for 10 minutes. The $GeCl_4$ mixture was dropped into the water/ethanol solution and stirred continuously for 3 hours. The resulting powder was collected by centrifugation, washed with ethanol and dried at 100°C under air to obtain the final product GeO_2.

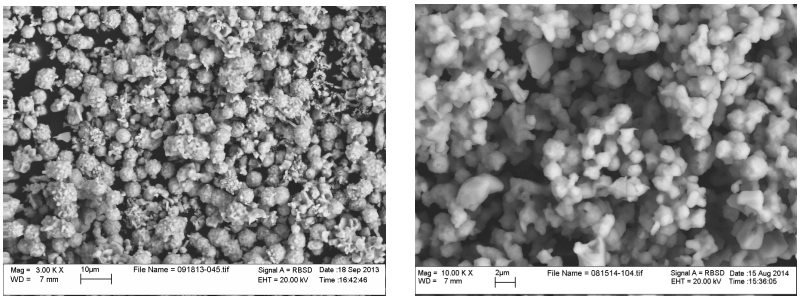

Figure. 2.1. SEM image of the synthesized micron-size germanium powder.

The GeO_2 was subsequently reduced under hydrogen gas at 700 °C for 30 min to obtain metallic micron-sized germanium.[29] The synthesized Ge particles were examined by SEM, as seen in Figure 2.1. The larger spherical Ge particles are made up of 1-3

micron-sized primary particles.

2.2.3. Electrochemistry

Electrochemically-cycled electrode samples for *ex-situ* experiments (NMR, PDF) were prepared using CR 2032 –type coin cells. The positive electrodes were formulated from 80% germanium powder as the active material, 10% Super P (Timcal) as a conducting matrix, and 10% polyvinylidene fluoride (PVDF, Kynar Flex 2801-00) as a binder. The mixture was suspended in N-methyl pyrrolidinone (NMP, 99+% Sigma-Aldrich) to form a slurry; the slurry was then coated on a Cu foil, dried at 100°C for 10 minutes in a convection oven (Grieve co.) and then at 60°C for 24 hours in a vacuum oven (Thermo scientific). Coin cells were assembled in an Ar-filled glove box using Li metal foil as the negative electrode. 1M $LiPF_6$ in a 1:1 volumetric mixture of ethylene carbonate (EC) and dimethyl carbonate (DMC) was used as the electrolyte and a porous glass fiber(GF/B, Whatman) as the separator. The cells were cycled using an Arbin instruments battery cycler with a cycling rate of C/50 (corresponding to a discharge to a theoretical capacity of 1623 mAh/g in 50 hours, assuming that $Li_{4.4}Ge$ is the final electrochemical lithiation product[26]) between 0.0 to 2.0 V at room temperature. After electrochemical cycling, each cell was dissembled and active material was washed with dimethyl carbonate (DMC, 99+% Sigma-Alrich) and dried in the Ar-filled glove box.

For *in-situ* NMR experiments, a flexible battery design was used. The positive electrodes were prepared by mixing 70% germanium, 10% super P, 20% polyvinylidene fluoride (PVDF), and dibutyl phthalate (DBP, 99% Sigma-Aldrich). The mixture was stirred in acetone (99%. J.T. Baker) and spread onto a flat glass surface and dried in air. DBP was removed by washing the film with ether (99%, Sigma-Aldrich). The dried film (4 mm (width) X 10 mm (length)) was laminated onto a carbon-coated Cu mesh and used as the positive electrode. Lithium metal foil of the same dimensions as the positive electrode film was pressed onto Cu wire mesh and used as the negative electrode. 1M $LiPF_6$ in a 1:1 volumetric mixture of ethylene carbonate (EC) and dimethyl ethyl carbonate (DMC) was used as the electrolyte and a piece of porous glass fiber as the separator. Components were assembled and sealed in a plastic bag (Kapak Corporation, type 500) inside the glove box. This flexible plastic battery cell was placed in a 5-mm in

diameter NMR coil of a static probe inside a magnet and connected with the external battery cycler. A Bio-Logic Science Instruments VSP potentiostat/galvanostat was used to electrochemically cycle the bag-cell battery within the voltage window of 0.0 - 2.0V.

2.2.4. X-ray Diffraction

Diffraction patterns were measured on a Bruker D8 diffractometer using Cu Kα irradiation (λ=1.54 Å) with a scan rate of 3°/min from a 2θ range of 10° to 80°. Samples were sealed with an air-tight cover under Ar atmosphere before being loaded into a XRD holder.

2.2.5. *Ex-situ* Pair distribution function analysis

Dried *ex situ* battery samples for PDF analysis were loaded into 1-mm diameter Kapton capillaries in an Ar-filled glovebox and sealed with epoxy. Total scattering data were acquired at the dedicated PDF beamline 11-ID-B at the Advanced Photon Source, Argonne National Laboratory. High-energy X-rays (~58 keV, λ = 0.2128 Å) were used in combination with a large amorphous-silicon based area detector (Perkin-Elmer) to collect X-ray scattering data to high values of momentum transfer ($\mathbf{Q}_{max} \approx 23$ Å). The scattering images were reduced to one-dimensional data within FIT2D[30] using CeO_2 as a calibration standard. The data were corrected for background scattering, Compton scattering and detector effects within pdfgetX2[31] and Fourier transformed to get $\mathbf{G}(\mathbf{r})$, the PDF. No attempt was made to subtract the carbon signals from the total PDF pattern. Least-squares refinements of structures against PDF data were performed in PDFGui in the distance range of 0 – 30 Å[32]. The initial value for the Q_{damp} parameter was set as 0.045 and refined against the data for crystalline Ge, and the atomic displacement parameters were set to intial values of $U_{11}=U_{22}=U_{33} = 0.005Å^2$ (constrained to be equal for all the Ge and Li atoms) and $U_{12}=U_{23}=U_{13}.=0$. Q_{damp}, lattice parameters, the linear atomic correlation factor (delta 1), and anisotropic temperature factors (U_{11}, U_{22}, U_{33}) were refined. The initial refinements of each PDF pattern assume a single pure phase, however, incorporation of a second minor phase significantly improved the refinement quality of some patterns, as indicated by reduced refinement quality factors, i.e., the R_w

values. Note that the value of R_w-factors for PDF refinements are higher than those for a Rietveld refinement of similar merit.

2.2.6. *Ex situ* ^{7}Li MAS NMR

Ex-situ battery samples were packed in 1.3 mm diameter Zirconia rotors in an Ar-filled glove box. High-resolution ^{7}Li MAS NMR spectra were acquired on a Varian InfinityPlus-500 MHz spectrometer at a magnetic field of 11.7 T, with a 1.3 mm MAS probe at a spinning speed of 50 kHz. Spectra were acquired using a rotor-synchronized spin-echo sequence (90°-τ-180°-τ-acq), where τ-values were set to be equal to one rotor period, i.e., 20 μs. The 90^o pulse length was 2.2 μs and the recycle delay 10 s. ^{7}Li spectra were referenced to a 1M ^{7}LiCl solution at 0 ppm. ^{7}Li MAS NMR spectra were normalized for analysis on the basis of the number of acquisitions and sample mass.

2.2.7. *In situ* ^{7}Li NMR

In-situ ^{7}Li experiments were carried out on a Tecmag Redstone 200 MHz spectrometer at a magnetic field of 4.7 T with a static probe. A one-pulse sequence with a 90^o pulse length of 2 μs and a recycle delay of 10 s was used. ^{7}Li spectra were referenced to a 1M ^{7}LiCl solution at 0 ppm. The Ge/Li battery was cycled at a rate of C/50.

2.3. Results

2.3.1. Li_xGe_y Alloy Model Compounds

In order to facilitate accurate identification of chemical phases formed on cycling the Ge anodes, several previously reported Li_xGe_y alloys: Li_9Ge_4, Li_7Ge_2, $Li_{15}Ge_4$, and $Li_{22}Ge_5$, were prepared with high-energy ball-milling and characterized using powder XRD, PDF analysis and *ex situ* high-resolution ^{7}Li solid-state NMR spectroscopy.

2.3.1.1. X-ray Diffraction (XRD) and Pair Distribution Function (PDF) analysis

XRD patterns of the materials with nominal compositions corresponding to the phases Li_9Ge_4, Li_7Ge_2, $Li_{15}Ge_4$, and $Li_{22}Ge_5$, are shown in Figure 2.2. Calculated PDFs with their fit to experimental data are found in Figure 2.3, and refinement statistics (residual values and phase fractions) are listed in Table 2.1.

Table 2.1. The distribution of Ge in different phases in the model compounds with corresponding R_w values for the fit to experimental data. The relative abundance of each phase is determined from the unit cell content from the fits to PDF data.

Composition	Phase 1	Phase 2	R_w
Li_9Ge_4	1 (Li_7Ge_3)	-	0.183
	0.93 (Li_7Ge_3)	0.07 (Li_9Ge_4)	0.175
Li_7Ge_2	1 (Li_7Ge_2)	-	0.178
	0.72 (Li_7Ge_2)	0.28 ($Li_{15}Ge_4$)	0.123
$Li_{15}Ge_4$	1 ($Li_{15}Ge_4$)	-	0.333
	0.70 ($Li_{15}Ge_4$)	0.30 (Li_7Ge_2)	0.085
$Li_{22}Ge_5$	1 ($Li_{22}Ge_5$)	-	0.203
	0.89 ($Li_{22}Ge_5$)	0.11(Li_7Ge_2)	0.183

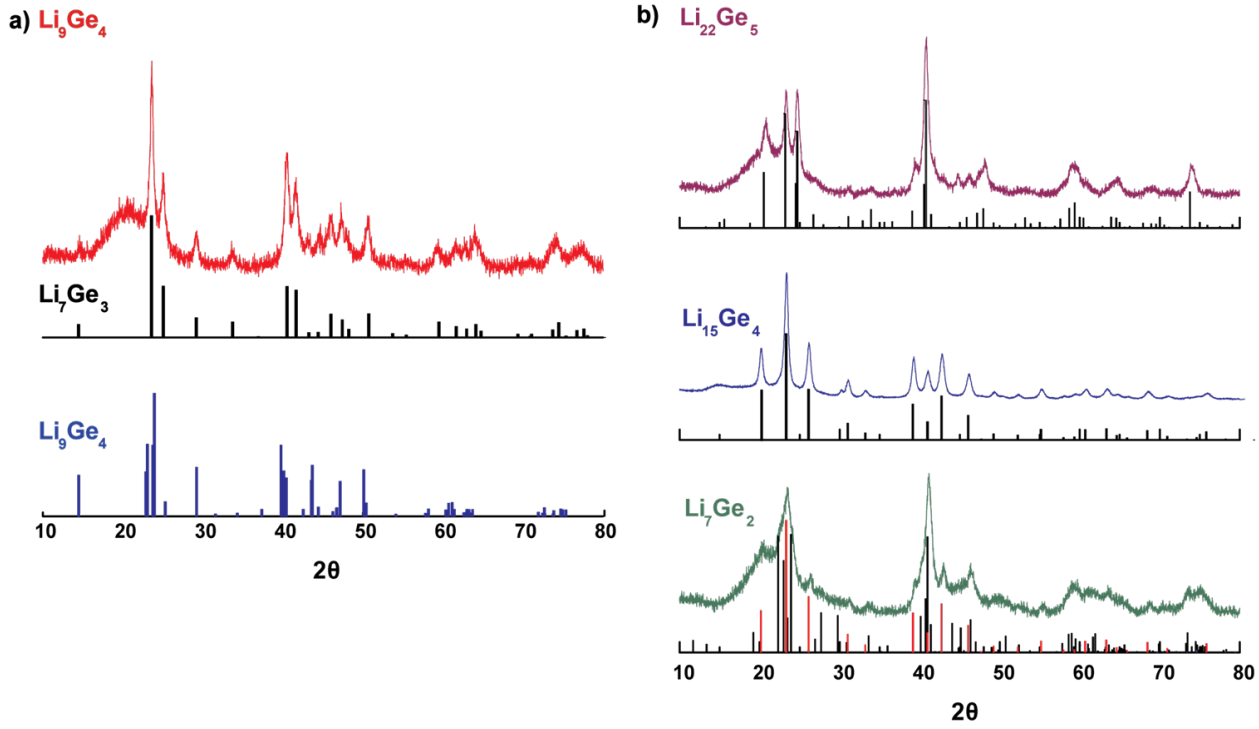

Figure 2.2. X-ray diffraction data (λ=1.54 Å) for the phases obtained by high energy ball milling with nominal stoichiometries, a) Li_9Ge_4, b)Li_7Ge_2, $Li_{15}Ge_4$, and $Li_{22}Ge_5$. The calculated peak intensities below each pattern correspond to the simulated patterns for the corresponding structures (both Li_9Ge_4 and Li_7Ge_3 ($P32_12$) tick marks being shown for the "Li_9Ge_4" experimental pattern). Li_7Ge_2 phase is not phase-pure, and contains reflections from both the Li_7Ge_2 *Cmmm* structure (black; structure from DFT calculation[16]) and $Li_{15}Ge_4$ (red tick marks). The broad background centered at 2θ = 20°, most noticeable in the patterns of the poorly crystalline phases, comes from the Kapton sample holder.

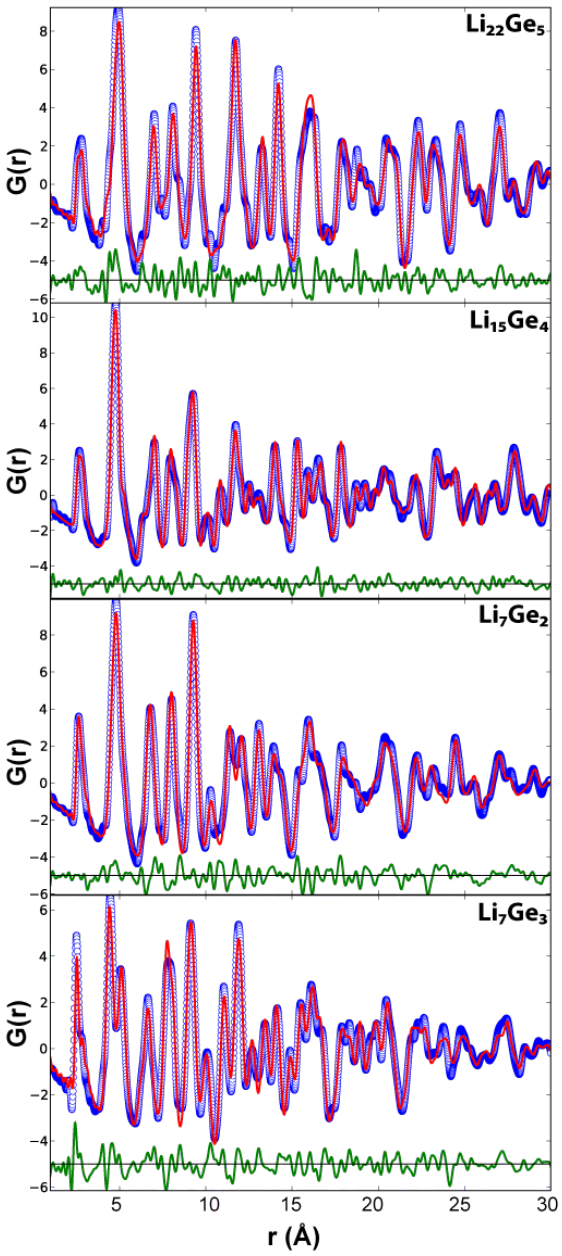

Figure 2.3. PDF (G(r)) patterns (blue) of the model compounds, Li_7Ge_3 (93% Li_7Ge_3 and 7% Li_9Ge_4) Li_7Ge_2 (72% Li_7Ge_2 and 28% of $Li_{15}Ge_4$), $Li_{15}Ge_4$ (70% $Li_{15}Ge_4$ and 30% Li_7Ge_2), and $Li_{22}Ge_5$ (89% $Li_{22}Ge_5$ and 11% Li_7Ge_2). The refinement patterns are shown in red with green lines representing the difference between the experimental and refined pattern. Further details including the chemical phases, their corresponding weighing factors, and refinement statistics are shown in Table 2.1.

The XRD reflections from $Li_{15}Ge_4$ can be indexed by the structure reported by Johnson *et al*[33]. This is further confirmed by the refinement against PDF data, which shows 70 % $Li_{15}Ge_4$ with a 30 % Li_7Ge_2 impurity that is not observed in the XRD pattern. This is unsurprising given the lack of crystallinity observed in the Li_7Ge_2 sample discussed below, which would result in limited Bragg diffraction of the minor Li_7Ge_2 impurity. The $Li_{22}Ge_5$ phase is poorly crystalline, but Bragg reflections in the XRD pattern can be indexed by the structure reported by Gladyshevskii *et al*[34]. Refinement against PDF data shows an excellent fit, indicating that the model compound is composed of 89 % $Li_{22}Ge_5$ with an 11 % Li_7Ge_2 impurity.

The X-ray pattern of the phase with nominal composition Li_9Ge_4 bears little resemblance to the pattern for the reported *Cmcm* Li_9Ge_4 phase.[35] The pattern simulated from phase Li_7Ge_3, in space group $P32_12$, identified by DFT calculations, was a good match to the experimental data[16]. A phase of this composition with the same space group has been previously mentioned in the literature but no structural or characterization data was presented.[11] A second report of a phase of this composition suggested that Li_7Ge_3 adopted a rhombohedral space group($R\bar{3}m$), [12] however the DFT results[16] have suggested that this rhombohedral phase most likely corresponds to Li_5Ge_2 or Li_8Ge_3. Li_7Ge_3(space group: $P32_12$) and Li_5Ge_2(space group : $R\bar{3}m$) show similar X-ray patterns, but Li_7Ge_3 is a more stable phase from the DFT calculations[16]. The PDF pattern of this nominal Li_9Ge_4 (Figure 3) contains correlations characteristic of Ge-Ge dumbbells (~ 2.5 Å), and a broad shoulder at ~ 2.8 Å, corresponding to the Li-Ge distances. Again, an extremely poor fit (R_w = 0.353) is obtained when a refinement using the Li_9Ge_4 structure is performed but a much improved fit (R_w = 0.183) is obtained when Li_7Ge_3 is used as an input to the structural refinement. The best fit to experimental data is obtained with a combination of 93% Li_7Ge_3 and 7% Li_9Ge_4, suggesting some slight disorder in the Li_7Ge_3 and/or the presence of a second minor phase. Our inability to prepare Li_9Ge_4 via ball-milling is consistent with the results from our prior calculations, which based on the relative stabilities of the various phases, predict that Li_9Ge_4 should disproportionate to form the Li_7Ge_3 ($P32_12$) phase[16] and a more Ge-rich phase.

The PDF pattern of the nominal Li_7Ge_2 phase can be well modelled with phase fractions of 72% for Li_7Ge_2 (*Cmmm*) and 28% for $Li_{15}Ge_4$. Of note is the change in the a

lattice parameter from 4.63 Å, reported by Hopf *et al*[36] to 4.49 Å at the end of the PDF refinement (see Table S1). The reflections calculated from the model refined against the PDF data good match to the experimental XRD pattern (shown in Figure 2).

2.3.1.2. ^{7}Li solid-state NMR

The characteristic NMR resonances for several Li_xGe_y model compounds are shown in Figure 2.4a. Reminiscent of the Li_xSi_y system[18], the phases with lower lithium content and higher Ge-Ge connectivity (in this case, Ge dumbbells) resonate at higher frequencies; Li_7Ge_3 and Li_7Ge_2 giving rise to resonances at 27, 10 ppm, respectively, while the more lithiated ones resonance at lower frequencies, $Li_{15}Ge_4$ resonating at -10 ppm. $Li_{22}Ge_5$ is metallic[18,37,38] and a Knight shift (instead of a chemical shift) results of +32 ppm. In addition to the major Li_xGe_y resonances, a peak is found in all the spectra at 2.8 ppm from Li_2O, the oxygen originating either from the surface oxide layers of the metal (Li and Ge) starting materials or from impurities introduced during the milling process. A minor Li_2CO_3 component may also be present due to reactions involving CO_2[39].

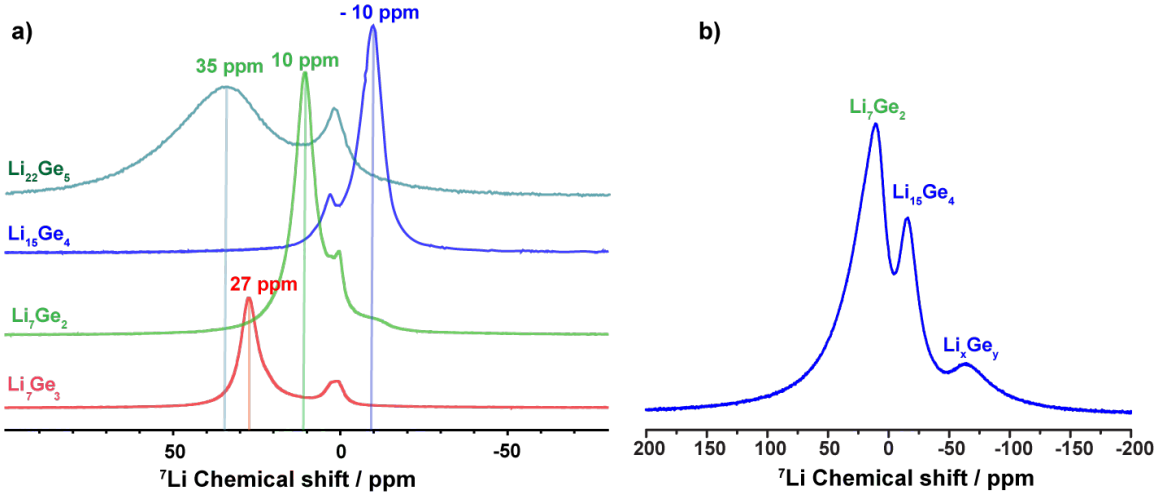

Figure 2.4. a) ^{7}Li MAS NMR spectra of synthesized Li_7Ge_3, Li_7Ge_2, $Li_{15}Ge_4$, and $Li_{22}Ge_5$. b) ^{7}Li NMR spectrum of $Li_{15}Ge_4$ 2 weeks after synthesis. Chemical shifts of major isotropic resonances are marked in a). The peaks close to 0 ppm correspond to diamagnetic (oxygen-containing) impurities. Li_xGe_y refers to a Li-rich phase that results from the decomposition of $Li_{15}Ge_4$.

The phase compositions of the synthesized Li_xGe_y model compounds obtained from PDF and NMR are mostly consistent, except that noticeable discrepancy is observed for the nominal $Li_{15}Ge_4$ phase. The PDF analysis reveals that the $Li_{15}Ge_4$ phase actually contains more than 20% Li_7Ge_2, while NMR shows no obvious ^7Li resonance from Li_7Ge_2; this might be due to the fact that PDF measurements were acquired two weeks after the synthesis of $Li_{15}Ge_4$, while NMR experiments were carried out on freshly prepared $Li_{15}Ge_4$. In order to confirm this hypothesis, ^7Li MAS NMR was carried out on the two-week old $Li_{15}Ge_4$ sample. The ^7Li NMR spectrum of aged $Li_{15}Ge_4$ (Figure 4b) now shows a dominant peak near 10 ppm, characteristic of Li_7Ge_2. In addition to the Li_7Ge_2 (10 ppm) and $Li_{15}Ge_4$ resonances (-10 ppm), another broad peak at -60 ppm suggests the formation of a Li-rich environment with a more shielded Li-environment than that found in $Li_{15}Ge_4$. Since no additional phase was observed in the PDF measurements, this suggests that this is a phase structurally related to $Li_{15}Ge_4$ (*i.e.*, it has similar short-to-medium range environments) that cannot be clearly distinguished from $Li_{15}Ge_4$ in the PDF. A more detailed analysis of $Li_{15}Ge_4$ results will be discussed in chapter 3. Two-dimensional ^7Li exchange NMR (Figure 2.5) shows that this Li-rich phase is close in space to the $Li_{15}Ge_4$ phase.

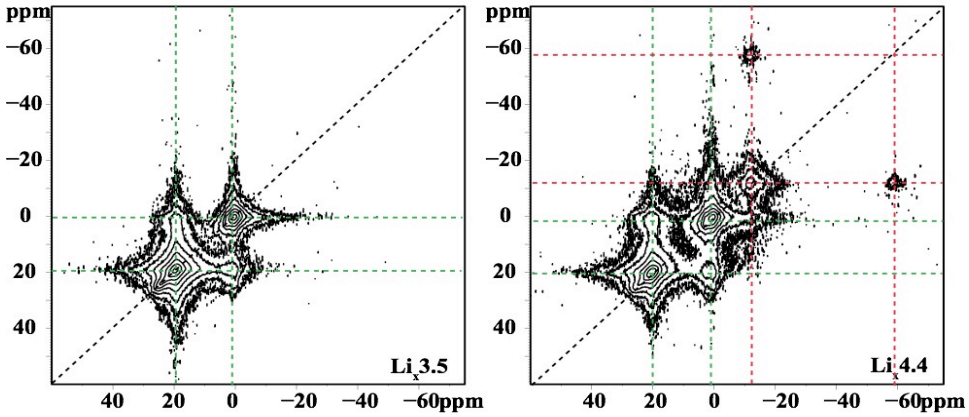

Figure. 2.5. 2D exchange ^7Li NMR of lithiated Ge anodes at 150 mV and 20 mV, with Li/Ge ratios of 3.5 and 4.4, respectively. This shows the close spatial proximity between Li_7Ge_3 (20 ppm) and SEI (~ 0-3 ppm), and $Li_{15}Ge_4$ (-13 ppm) and the Li-rich phases (-58 ppm), which is likely a product from $Li_{15}Ge_4$ decomposition. The weak intensity of the peak at -58 ppm is due to fast T_1 relaxation.

2.3.2. Micron-sized Germanium Anode

2.3.2.1. Electrochemistry

Figure 5a shows the first-lithiation electrochemical profile for crystalline germanium discharged against Li metal to 0 mV, with a current rate corresponding to C/50. The experimental discharge capacity of the first cycle is 1500 mAh/g.

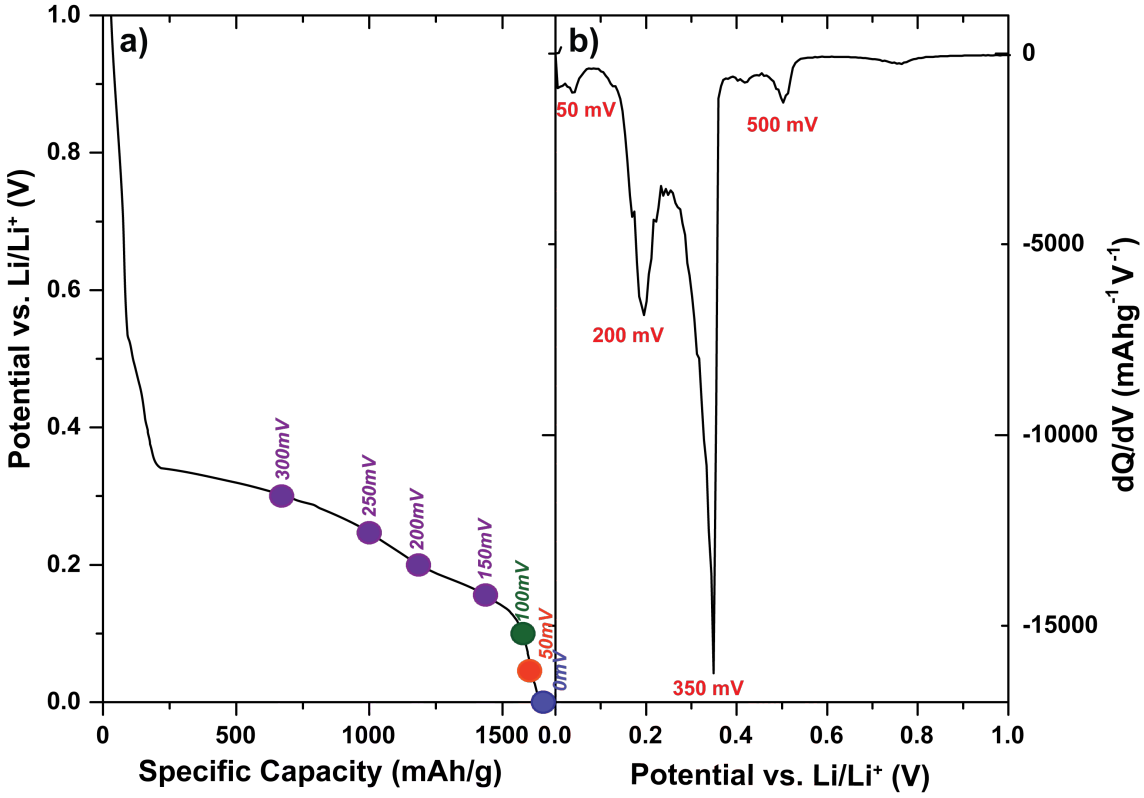

Figure 2.6. The electrochemistry plots, potential vs. capacity (left), and the differential capacity dQ/dV (right) of a Ge/Li battery obtained at a discharge rate of C/50. The filled circles designate the states of charge of the discharged electrodes disassembled for *ex situ* XRD, PDF, and NMR characterization as shown in Figures 2.7., 2.10, and 2.14, respectively.

The galvanostatic electrochemical profile (Figure 2.6) reveals four major processes, an initial fast drop in potential to 350 mV with an inflection at approximately 500 mV, followed by two flatter regions, the first at around 350 -250 mV, and the second at around 200 - 150 mV and finally a rapid drop to 0 V. The differential capacity, dQ/dV plot (Figure 2.6b), derived from the electrochemical profile (Figure 2.6a), confirms that there are four processes occurring at 500, 350, 200 and 50 mV.

2.3.2.2. XRD

XRD patterns of lithiated Ge anodes at different states of lithiation are shown in Figure 2.7. The pristine Ge electrode shows peaks corresponding to crystalline germanium ($Fd\bar{3}m$). These reflection peaks broaden upon lithium insertion, suggesting the breakdown of the crystallites or increased disorder or strain[40]. (The linewidths of the major Ge reflections for the pristine and 300 mV samples are tabulated in Table 2.2). The reflections from the Ge phase decrease in intensity on lithiation, with a corresponding growth the $P3_212$ Li_7Ge_3 phase. The Ge reflections have almost disappeared in the 250 mV sample, the Li_7Ge_3 phase dominating.

Between 250mV and 200 mV, Li_7Ge_3 transforms to a phase (or a group of phases) with a major, intense, broad, reflection at $2\theta = 41°$ and three minor ones at 24°, 59°, and 74° (λ=1.54Å). These four reflections are found in the diffraction pattern of our sample of Li_7Ge_2 (a comparison is shown in Figure 2.8), but other Li_7Ge_2 reflections are missing, indicating that the phase formed is not crystalline Li_7Ge_2. Further lithiation beyond 200 mV leads to the formation of crystalline $Li_{15}Ge_4$.

The reflections from $Li_{15}Ge_4$ continue to grow stronger until the end of discharge at 0 mV. A reduction in the full width at half maximum (FWHM; Table 2.3) of all the $Li_{15}Ge_4$ reflections suggests increased crystallinity. There is no evidence of $Li_{22}Ge_5$ or any other more highly lithiated phase. Le Bail refinements of XRD patterns of lithiated Ge anodes at 100, 50, and 0 mV (Figure 2.9 and Table 2.4) show gradually increased unit cell parameters, suggesting that the $Li_{15}Ge_4$ phase is able to accommodate a range of lithium stoichiometries, and that the final lithiation product is an overlithiated form of $Li_{15}Ge_4$.

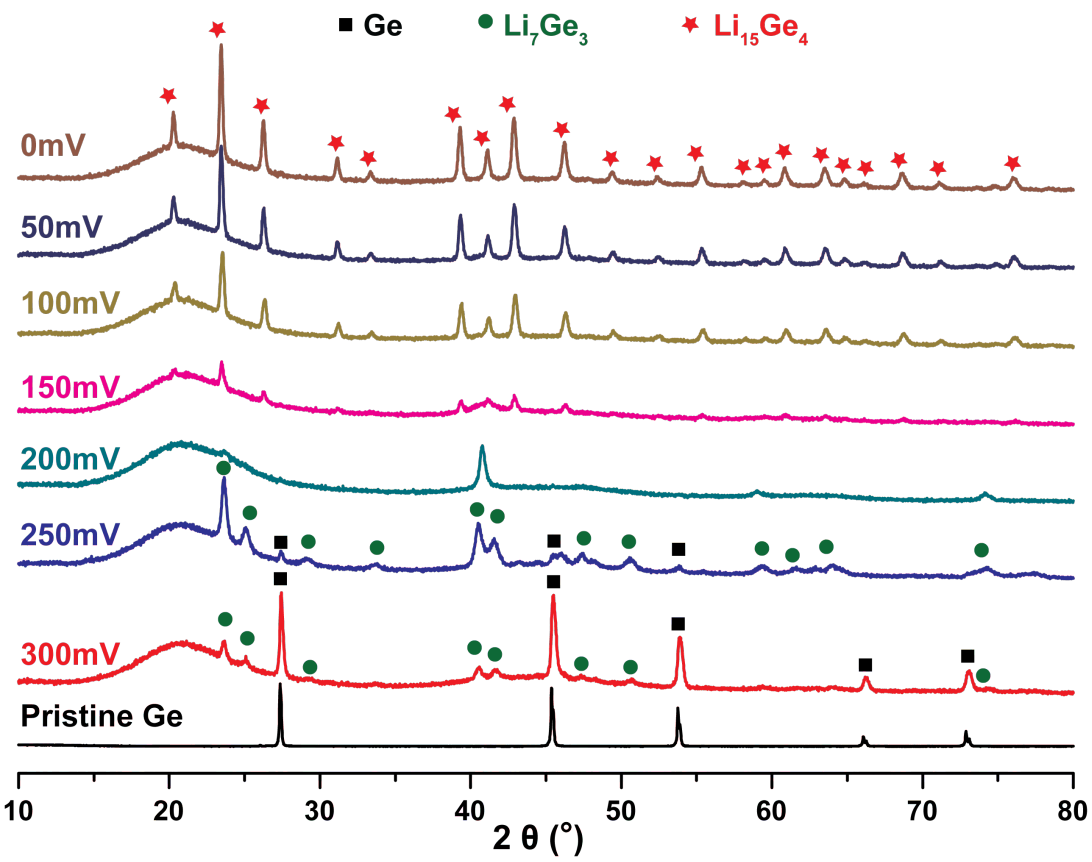

Figure 2.7. XRD patterns (λ=1.54 Å) of cycled Ge electrodes at the states of charge marked in Fig. 2.6, with corresponding potentials vs. Li/Li^+ indicated. Major reflections from Ge (▪), Li_7Ge_3 (•), and $Li_{15}Ge_4$ (□) are marked.

Table 2.2. Full width at half maximum (FWHM) of the main XRD reflections of pristine Ge and lithiated Ge at 300 mV

2θ	**27.5**	**45.6**	**54.1**	**66.5**	**73.4**
(Miller index)	**(1 1 1)**	**(0 2 2)**	**(1 1 3)**	**(0 0 4)**	**(1 3 3)**
Ge	0.16	0.23	0.24	0.28	0.28
300 mV	0.23	0.35	0.39	0.40	0.46

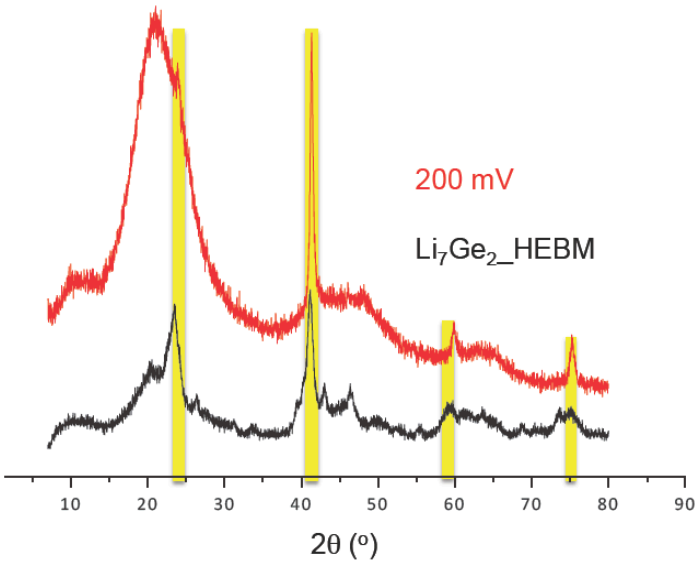

Figure. 2.8. Comparison of the XRD patterns of Li_7Ge_2 synthesized with the high-energy ball milling (HEBM) method (black, bottom and the cycled Ge anode discharged to 200 mV (red, top). (λ = 1.54 Å)

Table 2.3. FWHM of XRD reflections of lithiated Ge at 100 mV, 50 mV and 0 mV

2θ (Miller index)	**20.3 (1 1 2)**	**23.5 (0 2 2)**	**26.3 (0 1 3)**	**39.4 (2 3 3)**	**43.0 (1 3 4) /(0 1 5)**	**46.4 (1 2 5)**
100 mV	0.26	0.28	0.32	0.32	0.34	0.35
50 mV	0.26	0.24	0.26	0.29	0.33	0.35
0 mV	0.25	0.22	0.24	0.26	0.32	0.34

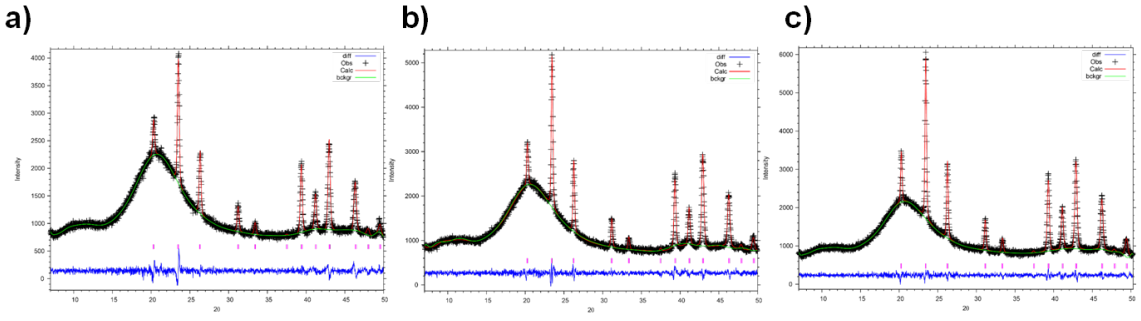

Fig. 2.9. Le Bail refinement of the XRD patterns of lithiated Ge anodes at a) 100 mV, b) 50 mV, and c) 0 mV. The refined unit cell parameters are listed in Table 2.4. (λ = 1.54 Å)

Table 2.4. The unit cell parameter of lithiated Ge anodes at 100 mV, 50 mV, and 0 mV, extracted from the Le Bail refinement shown in Fig. 2.9.

Voltage /mV	Unit cell parameter (Le Bail) /Å
100	10.7232(3)
50	10.7419(2)
0	10.7479(2)

2.3.2.3. PDF

Experimental PDF patterns, at various stages of lithiation, are shown in Figure 2.10. Visual analysis of the PDFs provides atomic-scale insights into the changes occurring on lithiation. The PDF for the pristine material shows sharp correlations out to high-r values (>100 Å). On initial lithiation, the peaks broaden significantly and the r_{max} (the maximum distance at which features are observed in the PDF) reduces to around 40 Å, indicating a loss in correlation length consistent with broadening of Bragg peaks in the XRD. The reduction in r_{max} continues to 150 mV, where significant correlations are observed only to approximately 20 Å. At further lithiation, peaks sharpen significantly, indicating the crystallisation of phases at the end of lithiation.

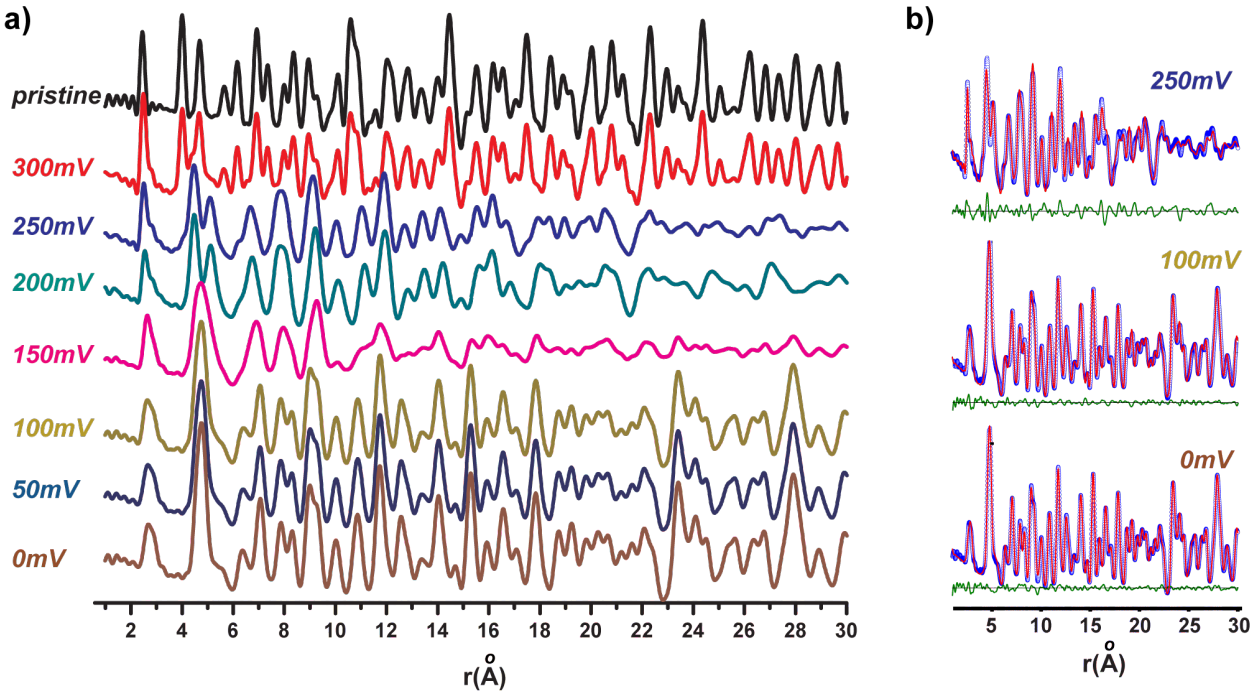

Figure 2.10. a) PDF patterns of cycled Ge electrodes at the different states of charge shown in Fig.2.6, with corresponding potentials vs. Li/Li^+ indicated. b) Representative refined patterns (red) overlapped with experimental patterns (blue) at 250, 100, and 0 mV. Difference between the experimental and simulated PDF (offset by -5) is shown in green. The phase compositions extracted from the refinement results at each state of charge are listed in Table 2.5.

Peaks corresponding the Ge-connectivity are clearly visible in the PDF, and are clear signatures of the Ge-Ge building units that are present. The sharp peak at 2.5 Å in PDFs seen in the PDF of the pristine electrode is characteristic of Ge-Ge bonds. A new broad peak at ~ 2.7 Å from Li-Ge correlations grows as a shoulder to the right of the Ge-Ge peak. Two other peaks at 3.8 and 4.4 Å from Ge-Ge next-nearest neighbour correlations in crystalline Ge shift to larger values between 300 and 250 mV, indicating an increase in Ge-Ge distances due to the insertion of Li and the breakdown of the extended Ge-framework. The Ge-Ge peaks broaden in the PDF at further lithiation; the 200 mV data suggest that the arrangement of the Ge-Ge dumbbell units in space is disordered in this voltage region. At 150 mV, one broad correlation is observed at 4.7 Å indicating that the majority of Ge is present as isolated atoms. This peak sharpens at lower voltages, indicating that the end product of this phase transition contains a narrower range of Ge-Ge (first shell, non-bonded) distances indicative of increased crystallinity, as observed in the XRD.

Quantification of the germanium phase distribution was obtained by performing least-squared refinements against the PDF data. Representative refinements of the PDF patterns at 250, 100, and 0 mV are shown in Fig. 2.10b (full refinement patterns and refinement statistics can be found in Figure 2.11 and Table 2.6) and the phase compositions at different states of charge from the refinement results are summarized in Table 2.5.

Table 2.5. Germanium distribution during cycling against lithium with corresponding R_w values. The relative abundance (by unit cell fraction) of the each Ge-containing phase was normalized based on the number of Ge atoms per unit cell.

	Li content	Ge	Li_7Ge_3	$Li_{13}Ge_5$	$Li_{13}Ge_4$	Li_7Ge_2	$Li_{15}Ge_4$	R_w
300mV	1.6	0.66	0.34					0.2090
250mV	2.5	0.06	0.94					0.1180
200mV	3.1			0.81	0.19			0.1570
				0.76		0.24		0.1790
150mV	3.9					0.76	0.24	0.1260
100mV	4.0		0.13				0.87	0.0603

50mV	3.9	0.11		0.89	0.0599
0mV	4.1		0.04	0.96	0.0618

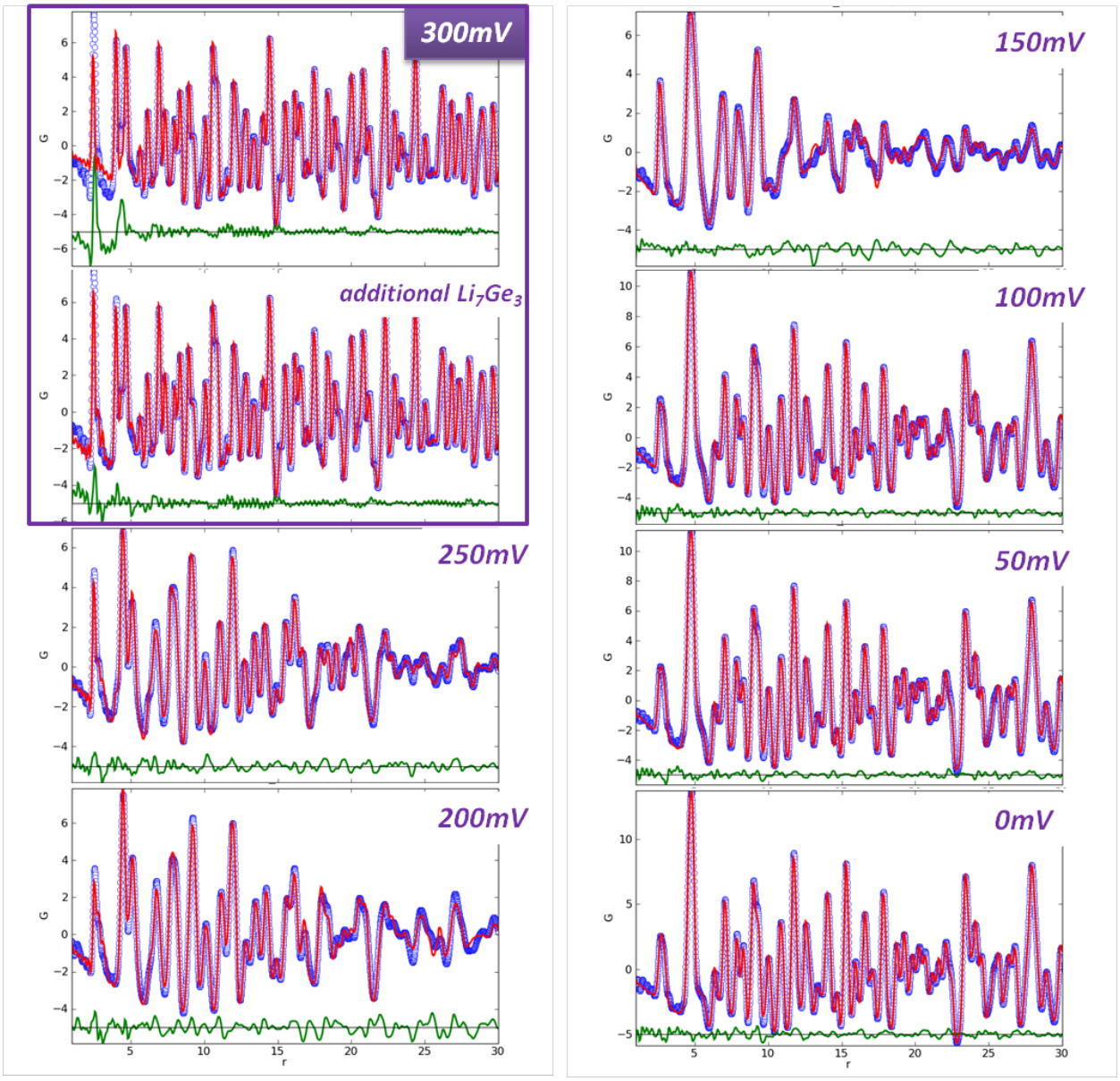

Figure 2.11. PDF refinement patterns of cycled Ge electrodes at different states of lithiation; Representative refined patterns (red) overlapped with experimental patterns (blue). The difference between simulated and experimental PDFs is shown in green (offset by -5). The phase composition extracted from the refinement results at each state of charge is listed in Table 2.5.

Table 2.6. PDF refinement statistics of lithiated Ge at 250, 100, and 0 mV.

	250mV		100mV		0mV	
	Ge	**Li_7Ge_3**	**Li_7Ge_3**	**$Li_{15}Ge_4$**	**Li_7Ge_2**	**$Li_{15}Ge_4$**
	$Fd\bar{3}m$	*$P32_12$*	*$P32_12$*	*$I\bar{4}3d$*	*Cmmm*	*$I\bar{4}3d$*
Ge distribution	0.06	0.94	0.13	0.87	0.04	0.96
Q_{damp}	-		-		0.0388	
Lattice parameters (Å)	5.6570	a=b=7.7250 c=18.4450	a/b=7.7570 c=18.4960	10.7640	a=9.2510 b=13.1820 c=4.4550	10.7670
Delta 1 (linear atomic correlation factor)	1.8390	2.4130	2.4550	1.9240	-	1.2820
Atomic displacement parameters ($U_{11}=U_{22}=U_{33}$, Å)	0.0100	Li: 0.0669	0.0155	0.0480	-	0.0459
		Ge: 0.0150	0.0142	0.0138	0.0177	0.0128
R_w	0.1180		0.0603		0.0618	

Refinement of a Ge-model structure against PDF data gives a good fit, with relatively few changes to structural parameters. The initial insertion of Li converts Ge into Li_7Ge_3; at 300 mV, there is already a significant fraction (0.34) of Li_7Ge_3 present in the PDF. Of note is the presence of an amorphous phase (additional to Ge and Li_7Ge_3) at early stages of the lithiation (Fig 2.12), characterised by a sharp peak at 2.55 Å (slightly longer than the Ge-Ge distance in crystalline Ge) and a second broad peak at 4.4 Å (Figure 2.12, Table 2.7). Addition of a second Li_7Ge_3 phase of particle diameter 6.7 Å is able to model this feature well, and reduces the R_w of the refinement from 20.4% to 11.5 %. We believe that this phase consists of short-range ordered areas of Ge-Ge dumbbells within or on the surface of the largely crystalline Ge-matrix, which form as a result of lithium incorporation into the crystalline Ge structure on initial lithiation, and act as nucleation points for the growth of Li_7Ge_3. The connectivity of this phase is certainly different to that of reported forms of amorphous-Ge, which have been found by neutron PDF to consist of a disordered tetrahedral network[41] .

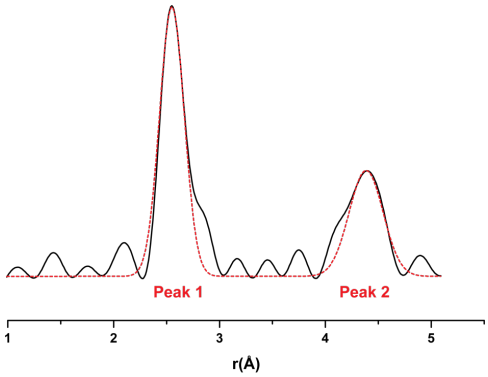

Figure. 2.12 Peak fitting of the additional amorphous Li_7Ge_3 phase at 300mV in PDF (performed in Fityk[42]). The fitting results are listed in Table 2.7.

Table 2.7. Peak fitting results of amorphous Ge phase at 300 mV.

	peak1	peak 2
r (Å)	2.55	4.38
Height	6.1	2.4
FWHM	0.27	0.38
Area	1.77	0.96

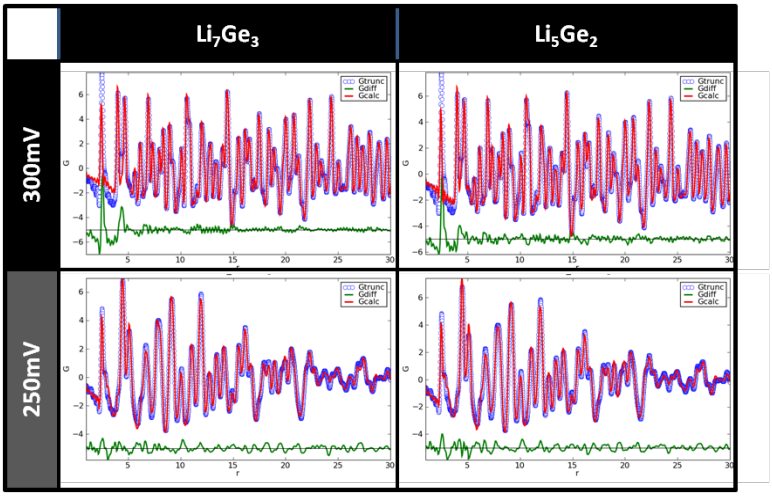

Figure. 2.13. Comparison of PDF refinement patterns with Li_7Ge_3 and Li_5Ge_2 of cycled Ge electrodes at 300 and 250 mV; Representative refined patterns (red) overlapped with experimental patterns (blue). The difference between simulated and experimental PDFs is shown in green (offset by -5). The phase composition extracted from the refinement results and refinement statistics at each state of charge is listed in Table 2.8.

Complete conversion to Li_7Ge_3 occurs at 250 mV. We assign this phase to Li_7Ge_3 as opposed to Li_5Ge_2 (a phase with a similar Li:Ge ratio (2.33 vs. 2.5) that gives rise to a very similar XRD pattern) on the basis of the larger thermal parameters obtained for refinements using Li_5Ge_2 phase, which suggest that a higher degree of disorder in the atomic positions is required to capture the information in the PDF (Figure 2.13 and Table 2.8), the lower R_w value obtained by Li_7Ge_3 for the refinement, and the DFT calculations,[16] which predict that Li_7Ge_3 is the stable phase around this composition.

Table 2.8. Comparison of PDF refinement statistics with Li_7Ge_3 and Li_5Ge_2 at 300 mV and 250 mV.

	Unit cell parameter(Å)		Ge	Li_7Ge_3	Ge	Li_5Ge_2
			a=5.6210	a=7.7047 c=18.3479	a=5.6210	a=4.4658 c=18.3320
300mV Li_x=1.6	Ge distribution		0.6644	0.3356	0.5923	0.4077
	unit cell parameter	a	5.6534	7.7179	5.6536	4.4515
		c		18.3863		18.3316
	Li thermal parameter			0.0373		0.1184
	Ge thermal parameter			0.0174		0.0415
	R_w		0.2095		0.2076	
250mv Li_x=2.5	Ge distribution		0.0599	0.9401	0.0632	0.9368
	unit cell parameter	a	5.6573	7.7254	5.6570	4.4602
		c		18.4494		18.4504
	Li thermal parameter			0.0669		0.0882
	Ge thermal parameter			0.0150		0.0199
	R_w		0.1178		0.1354	

The best fit to the PDF pattern at 200 mV with a single known or theoretically predicted[16] phase is obtained when the phase $Li_{13}Ge_5$ ($Li_{2.6}Ge$), comprising Ge-Ge dumbbells and isolated Ge, was used; this phase is predicted to be thermodynamically stable.[16] The addition of a second phase, $Li_{13}Ge_4$ ($Li_{3.25}Ge$), also containing Ge-Ge dumbbells and isolated Ge, improves the fitting quality (R_w is reduced from 0.249 to 0.157). However, several two-phase combinations of Li_xGe_y structures can fit the data without significantly compromising the quality of the refinement, the phases including Li_5Ge_2, $Li_{13}Ge_5$, Li_8Ge_3, $Li_{13}Ge_4$, and Li_7Ge_2 (*Cmmm*), the best quality fits being obtained when one of the components was $Li_{13}Ge_5$. The refinement data with various

one-phase or two-phase combinations can be found in Tables 2.5 and 2.9. The common structural feature of the compounds mentioned above is parallel-aligned Ge-Ge dumbbells with discrete Li and in some cases Ge atoms in-between, as discussed below.

Table 2.9. Possible phase combinations for the PDF refinement of lithiated Ge anode at 200 mV.

	Li_7Ge_3	Li_5Ge_2	$Li_{13}Ge_5$	Li_8Ge_3	$Li_{13}Ge_4$	Li_7Ge_2 *Cmmm*	Li_7Ge_2 $P\,3_m1$	R_w
	$Li_{2.33}Ge$	$Li_{2.5}Ge$	$Li_{2.6}Ge$	$Li_{2.67}Ge$	$Li_{3.25}Ge$	$Li_{3.5}Ge$		
200mV	1							**0.285**
		1						**0.275**
			1					**0.249**
				1				**0.319**
					1			**0.68**
	0.44		0.56					**0.196**
			0.81		**0.19**			**0.157**
			0.76			**0.35**		**0.179**
			0.85				0.15	**0.235**
	0.65			0.35				**0.209**
	0.99					0.01		**0.282**

By 150 mV, correlations from both Li_7Ge_2 and $Li_{15}Ge_4$ phases are present. Correlations from crystalline $Li_{15}Ge_4$ dominate the PDF pattern until the end of discharge, the correlations persisting out to more than 70 Å. The presence of minor Li_7Ge_3 or Li_7Ge_2 phase (< 10 % phase fraction) may result from the decomposition of metastable $Li_{15}Ge_4$ or merely be a signature of residual Ge-Ge dumbbells due to the inhomogeneous nucleation of the $Li_{15}Ge_4$ phase from the more disordered Li_xGe_y column structures (R_w is reduced from 0.0686 to 0.0618), as seen for Si[28].

2.3.2.4. *Ex situ* ^{7}Li NMR

Ex situ ^{7}Li solid-state MAS NMR provides insight into the lithium local environments at stages of lithiation (Figure 2.14). The formation of solid-electrolyte-interphase (SEI) is observed at very early stage of discharge (300mV), characterized by resonances at around ~0 ppm, due to the decomposition of electrolyte solvents (EC and DMC) on carbon and Ge anode surfaces.[26,43] A sharp resonance at ~ 22 ppm also appears, an indication of the presence of the Li_7Ge_3 ($Li_{2.33}Ge$) phase. The broader component under the 22 ppm

resonance is tentatively ascribed to lithium ions present in the crystalline Ge phase and possibly the formation of more disordered lithiated Ge phases. PDF refinements also suggest a presence of an additional amorphous phase containing short-range ordered Ge-Ge dumbbells in this region. At 250mV, the Li_7Ge_3 resonance dominates the spectrum and the broad component has essentially disappeared. The "Li_7Ge_3" resonance grows further, but has also broadened significantly and shifted slightly to a lower chemical shift value for the sample obtained at 200mV, suggesting a distribution of Li local environments, consistent with the disorder observed in both the XRD and PDF patterns.

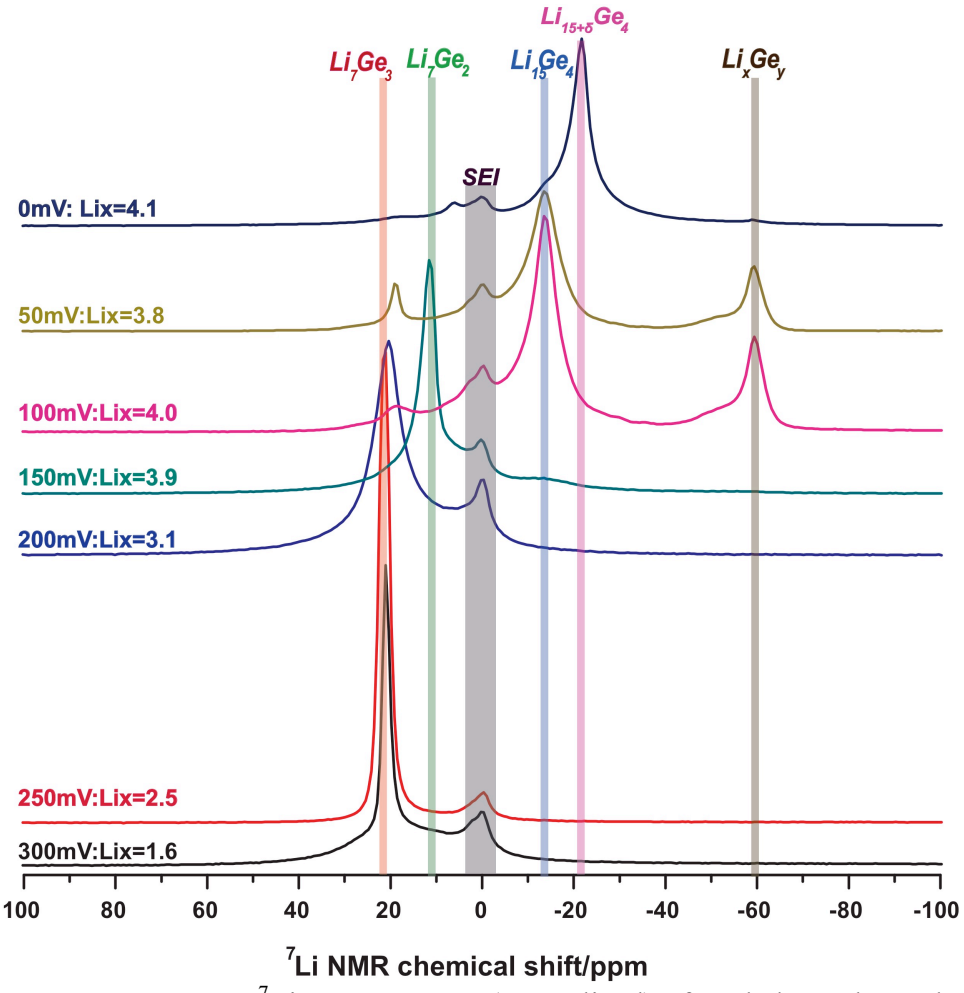

Figure 2.14. *Ex situ* ^{7}Li NMR spectra (normalized) of cycled Ge electrodes at the states of charge identified in Figure. 2.6a, with corresponding potentials vs. Li/Li^+ and Li content indicated. Relevant peak assignments are shown. Li_xGe_y refers to a Li-rich phase that results from the decomposition of $Li_{15}Ge_4$.

The lower shift is consistent with the PDF data, which indicated that $Li_{13}Ge_5$ ($Li_{2.6}Ge$) was present as a major component at this point, further lithiation and the breakage of Ge-Ge bonds all resulting in smaller ^7Li chemical shifts. At 150 mV, a single, a sharp resonance is observed at 10 ppm, characteristic of Li_7Ge_2. Upon further lithiation, Li_7Ge_2 is converted to $Li_{15}Ge_4$, (– 13 ppm). Two additional peaks are observed, a minor resonance at around 20 ppm (likely from Li_7Ge_3 or phases containing similar ^7Li local environments to those found in Li_7Ge_3), consistent with the PDF analysis, and a peak at -58 ppm. This - 58 ppm peak is also found in the ^7Li NMR spectra of the model compound $Li_{15}Ge_4$ two weeks after its synthesis, possibly a decomposition product of $Li_{15}Ge_4$. 2D exchange NMR (Figure 2.5) reveals that this – 58 ppm phase is in close proximity to $Li_{15}Ge_4$ on the nano-scale, suggesting the decomposition product is in the same phase as $Li_{15}Ge_4$ or on the surface of $Li_{15}Ge_4$. Lithiation of the Ge anode to 0 mV results in a ^7Li resonance at – 22 ppm, which is ascribed to an over-lithiated phase $Li_{15+\delta}Ge_4$, similar to the process observed in the lithiation Si anodes ($Li_{15+\delta}Si_4$) in our prior studies[18,28]. Further electrolyte decomposition is also observed at low voltages, suggested by the changes in ^7Li resonances between 0-10 ppm.

2.3.2.5. *In situ* ^{7}Li NMR

In situ ^7Li NMR was performed to understand the sequential events occurring during the lithiation process further. The advantage of this method is that the battery is not stopped during the experiment, which removes the possibility of structural relaxation of metastable phases when the voltage is removed and any possible decomposition of the products that occurs over time[18]. The spectra (Figure 2.15) all show an intense peak around 0 ppm, from the free electrolyte in the bag cell battery and SEI on the surface of the electrode.

No other discernible, well-defined signal is observed at voltages above 300 mV. A broad component with a shift of ~23 ppm, assigned to Li_7Ge_3, starts to appear below 300 mV. This resonance progressively grows in intensity and sharpens until potentials below 200 mV are reached; this corresponds to the flatter voltage region between 350 mV and approximately 200 mV in the electrochemical curve. Below 200 mV, the 23ppm resonance continuously shifts to around 10 ppm, the shift observed in the model

compound Li_7Ge_2. The continuous shift suggests a continuous structural transformation from Li_7Ge_3 to Li_7Ge_2. A weak and broad resonance starts to at around –13 ppm (overshadowed by the strong electrolyte peak at 0 ppm) around 150 mV, consistent with the formation of $Li_{15}Ge_4$. Deeper discharge to 0 mV leads to an intense peak at -22 ppm, likely from an overlithiated phase $Li_{15+\delta}Ge_4$.

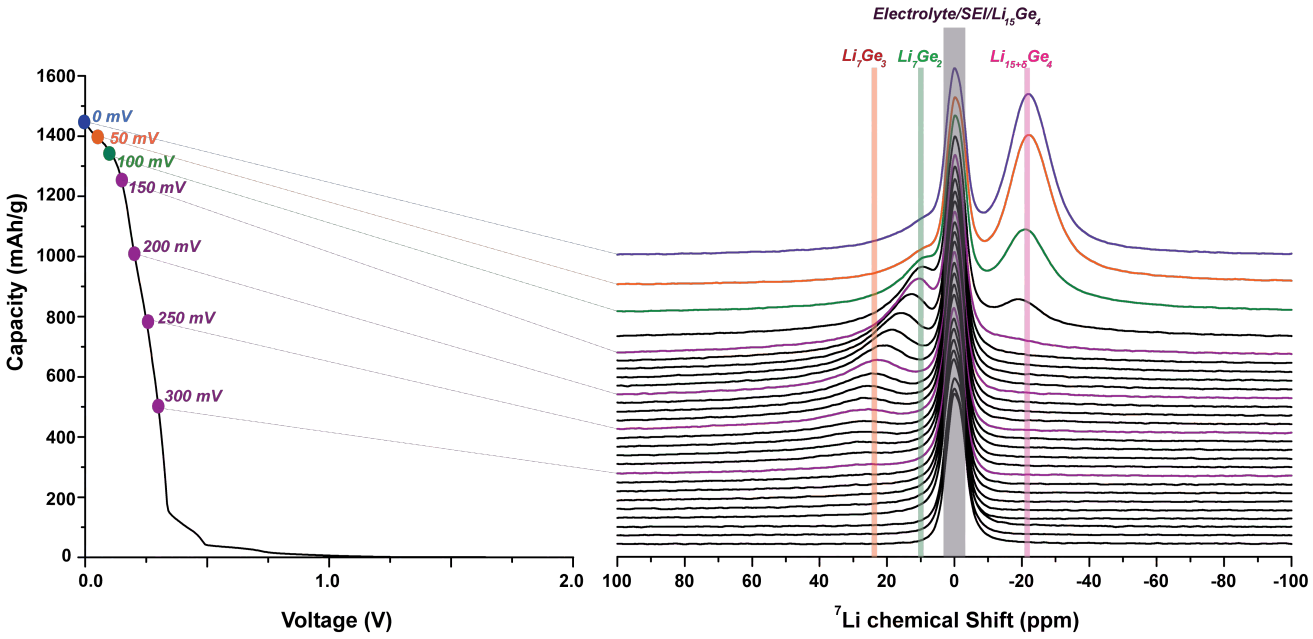

Figure 2.15. *In situ* ^{7}Li NMR spectra of a Ge/Li plastic-bag battery cycled at a rate of C/50. The corresponding states of charge for select spectrum are indicated on the electrochemical profile. Possible assignments to specific chemical phases are indicated.

2.4. Discussion

On the basis of the electrochemistry, XRD, PDF, and *in/ex situ* NMR analyses, we propose a four-step mechanism for the lithiation process of microcrystalline Ge anodes:

i.OCV – 350 mV: **Formation of SEI layer.**

Lithiation of Ge anodes starts with a steep drop in voltage to 350 mV, a small inflection appearing at 500 mV in the electrochemistry profile. The capacity (< 0.5 Li) obtained in this region is mainly from electrolyte decomposition to form an SEI layer on the surfaces of Ge/C, (with evidence from the peak at close to 0 ppm in the *ex situ* NMR), the insertion of Li within crystalline Ge, and possibly the reaction with GeO_2 impurities on the surface of Ge.

ii. 350 mV – 250 mV: Conversion from crystalline Ge to Li_7Ge_3.

A flatter voltage region is observed in the electrochemistry. Nominally, a two-phase reaction mechanism is observed in this voltage regime, as indicated by the coexistence of both Ge and Li_7Ge_3 phases, in the XRD and PDF patterns of the 300 and 250 mV samples. A single main resonance at 22-23 ppm from the Li_7Ge_3 phase in the *in/ex situ* NMR spectra with little variation in the shift position also supports a two-phase reaction mechanism. The potential should be completely flat for a two-phase reaction, the sloping potential profile being associated with the difficulty in breaking up the crystalline Ge lattice, resulting in a considerable overpotential. This is similar to that observed for Si. [44,45] A recent *in-situ* XRD study[23] showed an abrupt decrease of crystalline Ge phase between 253 mV and 210 mV. These authors attribute the change to the two-phase reaction from c-Ge to amorphous Li_9Ge_4. In contrast, our XRD and PDF analyses clearly show that Li_7Ge_3 ($P3_212$), not Li_9Ge_4 forms, Li_7Ge_3 being the stable phase at and close to this composition, on the basis of DFT calculations.[16] These phases are difficult to distinguish between with techniques such as EXAFS, both Li_9Ge_4 and Li_7Ge_3 containing Ge-Ge dumbbells, but with different spacings (or number of Li) between the dumbbells and the correspondingly slightly longer Ge-Ge dumbbell bond lengths in Li_7Ge_3.

iii. 250 mV – 150 mV: Structural transformation from Li_7Ge_3 to Li_7Ge_2.

A gradual sloping voltage region is observed in the electrochemistry. The continuous shift of the resonance in *in situ* ^{7}Li NMR implies a continuous structural transformation from Li_7Ge_3 to Li_7Ge_2. The broad ^{7}Li resonances seen in the *ex situ* NMR experiments also suggests a greater degree of local disorder compared with other regions.

Both the XRD and PDF patterns indicate considerable disorder. Nonetheless, broad Bragg reflections are still observed, indicating the existence of partial ordering along certain directions. PDF refinements suggest that specific short-range structural motifs-columns containing Ge-Ge dumbbells and isolated Ge/Li atoms-are formed in this region. These are present in all the following phases: Li_7Ge_3, Li_5Ge_2, $Li_{13}Ge_5$, Li_8Ge_3, and $Li_{13}Ge_4$ as shown in Figure 2.16, but refinement indicates that none of these phases is the sole lithiation product.

Combining the evidence from XRD, PDF, and NMR, the lithiation process at this stage likely follows a heterogeneous pathway from Li_7Ge_3 (Ge-Ge bond length: 2.50 Å) to Li_7Ge_2 (Ge-Ge bond length: 2.62 Å), via Li_5Ge_2, $Li_{13}Ge_5$, Li_8Ge_3, and $Li_{13}Ge_4$, where the common structural features of all these phase are maintained. Ge-Ge bonds are gradually broken and the fraction of Li and isolated Ge atoms increases so that by 150 mV, Li_7Ge_2 dominates. Lim *et al.* [23] also suggested that Ge-Ge bond distance are increased to 2.6 Å below 220 mV, consistent with the proposed formation of Li_7Ge_2. As shown in Figure 2.16, $Li_{13}Ge_4$ and Li_7Ge_2 lie above the convex hull (i.e., they are metastable phases). Their formation is, therefore, kinetically driven: the system reacts to form structural motifs that locally resemble $Li_{13}Ge_4$ and Li_7Ge_2 rather than forming $Li_{15}Ge_4$ directly from the thermodynamic phases $Li_{13}Ge_5$ and Li_8Ge_2; only when the Ge-Ge bonds are weak enough/present in too lower concentrations is the growth of the $Li_{15}Ge_4$ crystalline phase kinetically favored.

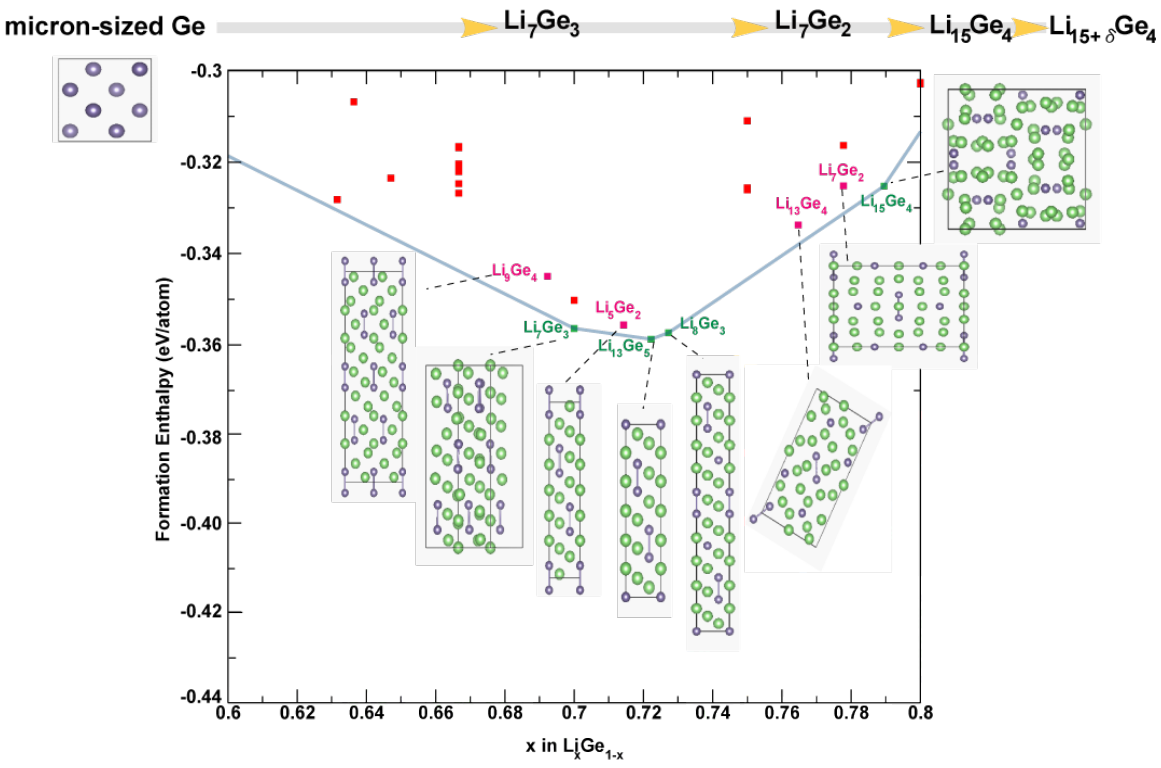

Figure 2.16. The lithiation pathway showing the common structural features of possible lithiated Ge phases between Li_7Ge_3 and Li_7Ge_2: they all contain parallel-aligned Ge-Ge dumbbells in columns with discrete Li and in some cases Ge atoms in-between them. The $Li_{15}Ge_4$ phase with isolated Ge atoms is shown for comparison. The blue line is the tie-line indicating the stable phases at 0 K predicted by DFT.[16] The squares indicate the formation enthalpy of a structure; green squares correspond to the thermodynamic phases; the red squares correspond to metastable phases (at 0 K).

iv. 150 mV – 0 mV: Transformation from Li_7Ge_2 to $Li_{15}Ge_4$ and overlithiated $Li_{15}Ge_4$.

A steep drop in voltage is observed in the electrochemistry. The appearance of sharp reflections in the XRD patterns and long-range correlations in PDF indicate the relatively high crystallinity of the $Li_{15}Ge_4$ phase. Some Li_7Ge_3 and a Li-rich phase are seen in the *ex-situ* PDF and NMR experiments, which we ascribe to the decomposition of the $Li_{15}Ge_4$ phase before the experiments are performed or a certain degree of

inhomogeneity in the lithiation process. The formation of $Li_{15}Ge_4$ from the metastable Li_7Ge_2 phase is similar to what is observed in silicon anodes, however, here, the Si-Si bonds within an amorphous (rather than partially ordered) phase need to be broken before the $Li_{15}Si_4$ phase nucleates. In a further analogy with the Si chemistry, subsequent lithiation leads to the formation of an over-lithiated phase, which shows a different Li local environment in the ^7Li NMR spectra as compared with $Li_{15}Ge_4$. This over-lithiated phase shares a similar long-/short-range structure as $Li_{15}Ge_4$ as suggested by the lack of significant change in the XRD or PDF patterns other than an increased unit cell parameter (from 10.7232(3) Å to 10.7479(2) Å). We, thus, tentatively assign this over-lithiated phase to $Li_{15+\delta}Ge_4$, its formation presumably being associated with the 50 mV process seen electrochemically. Further study will be presented in chapter 3. (The same process for silicon occurs at essentially the same potential, however, in the silicon case, it is more difficult to separate $Li_{15}Si_4$ formation from its overlithiation due to the larger kinetic barrier for crystalline $Li_{15}Si_4$ formation and the larger overpotential typically required to drive the reaction.[18,28]) No indication of $Li_{22}Ge_5$, as proposed by some prior studies[27], is found, even at the very end of discharge, the $Li_{22}Ge_5$ phase possessing distinctive signatures in both the NMR spectra and PDFs.

Finally, we note that the nature of the phases, particularly in the disordered (250 – 150 mV) region will probably vary, depending on the size of Ge nanoparticles and the lithiation rates, both of which will alter the kinetics of the various phase transformations. The region will be particularly sensitive to lithiation rates and particle sizes since there are numerous structurally related phases with very similar energies. Variations in potentials across the electrode (due to differences in electronic wiring, tortuosities of the paths for Li^+ in the electrolyte) will all affect which phases are formed during the lithiation process. Future work will focus on particle size effects and the lithiation reactions on charge and in subsequent cycles.

2.5. Conclusions

The lithiation mechanisms of micron-sized Ge anodes have been studied with XRD, PDF, and *in/ex situ* high-resolution ^{7}Li solid-state NMR spectroscopy. Relevant model compounds identified in previous studies, i.e. Li_9Ge_4, Li_7Ge_2, $Li_{15}Ge_4$, and $Li_{22}Ge_5$, were first synthesized and characterized to provide experimental signatures for identifying Li_xGe_y phases in lithiated Ge products. Li_9Ge_4 was not formed under these synthetic conditions. Instead the $P32_12$ polymorph of Li_7Ge_3 was formed, a phase that has been predicted to be thermodynamically stable by our DFT calculations[16], but not unambiguously identified experimentally previously.

The lithiation process of micron-sized Ge anodes involves the formation of Li_7Ge_3 phase initially through a two-phase reaction process. No Li_9Ge_4 was formed, contrary to previous reports. Interestingly Li_7Ge_3 converts to Li_7Ge_2 via a series of highly disordered phases, as shown in Figure 2.17, all of these phases containing columns of Li, Ge-Ge and Ge, the relative proportions varying as lithiation proceeds. Eventually Li_7Ge_2-like short-to medium range environments are observed (by NMR and PDF analysis), indicating that most of the Ge-Ge bonds have been broken. At this point, the nucleation and growth to form crystalline $Li_{15}Ge_4$ occurs. This phase can be further lithiated, likely to form $Li_{15+\delta}Ge_4$.

In conclusion, this study provides a compelling illustration of how a variety of *ex-/in-situ*, experimental techniques which probe short-, medium- and long-range structure in combination with structural and energetic predictions from DFT studies can be used to obtain comprehensive insights into complex lithiation mechanisms in alloy phases. In particular, DFT studies identified a stable polymorph for the composition Li_7Ge_3, which was then shown by experiments to represent a key structure on the lithiation pathway.

2.6. References

(1) Kim, T.-H.; Park, J.-S.; Chang, S. K.; Choi, S.; Ryu, J. H.; Song, H.-K. *Adv. Eng. Mater.* **2012**, *2*, 860.

(2) Park, C. M.; Kim, J. H.; Kim, H.; Sohn, H. J. *Chem. Soc. Rev.* **2010**, *39*, 3115.

(3) Obrovac, M. N.; Christensen, L. *Electrochem. Solid-State Lett* **2004**, *7*, A93.

(4) Seng, K. H.; Park, M. H.; Guo, Z. P.; Liu, H. K.; Cho, J. *Nano letters* **2013**, *13*, 1230.

(5) Zhang, W.-J. *J. Power Sources* **2011**, *196*, 13.

(6) Fuller, C.; Ditzenberger, J. *Phys. Rev.* **1953**, *91*, 193.

(7) Wang, D. W.; Chang, Y. L.; Wang, Q.; Cao, J.; Farmer, D. B.; Gordon, R. G.; Dai, H. J. *J. Am. Chem. Soc.* **2004**, *126*, 11602.

(8) Li, D.; Seng, K. H.; Shi, D.; Chen, Z.; Liu, H. K.; Guo, Z. *J. Mater. Chem. A* **2013**, *1*, 14115.

(9) Sangster, J.; Pelton, A. D. *J. Phase Equilib.* **1997**, *18*, 289.

(10) Grüttner, A.; Nesper, R.; Schnering, H. G. v. *Angew. Chem. Inr. Ed.* **1982**, *21*, 912.

(11) Grüttner, A.; Nesper, R.; Schnering, H. G. v. *Acta. Crystallog* **1981**, *A37 (Suppl)*, C.

(12) Jain, A.; Kawasako, E.; Miyaoka, H.; Ma, T.; Isobe, S.; Ichikawa, T.; Kojima, Y. *J.Phys.Chem. C* **2013**, *117*, 5650.

(13) Dupke, S.; Langer, T.; Pottgen, R.; Winter, M.; Eckert, H. *Solid state nuclear magnetic resonance* **2012**, *42*, 17.

(14) Pickard , C. J.; Needs, R. J. *Phys. Rev. Lett* **2006**, *97*, 045504.

(15) Pickard, C. J.; Needs, R. J. *J. Phys.: Condens. Matter* **2011**, *23*, 053201

(16) Morris, A. J.; Grey, C. P.; Pickard, C. J. *Phys. Rev. B: Condens. Matter Mater. Phys.* **2014**, *90*, 054111.

(17) Stjohn, M. R.; Furgala, A. J.; Sammells, A. F. *J. Electrochem.Soc.* **1980**, *127*, C136.

(18) Key, B.; Bhattacharyya, R.; Morcrette, M.; Seznéc, V.; Tarascon, J.-M.; Grey, C. P. *J. Am. Chem. Soc.* **2009**, *131*, 9239.

(19) Key, B.; Morcrette, M.; Tarascon, J.-M.; Grey, C. P. *J. Am. Chem. Soc.* **2010**, *133*, 503.

(20) Kim, Y.; Hwang, H.; Lawler, K.; Martin, S. W.; Cho, J. *Electrochimica Acta* **2008**, *53*, 5058.

(21) Baggetto, L. c.; Notten, P. H. L. *J. Electrochem. Soc.* **2009**, *156*, A169.

(22) Liu, X. H.; Liu, Y.; Kushima, A.; Zhang, S.; Zhu, T.; Li, J.; Huang, J. Y. *Adv.Energy Mater.* **2012**, *2*, 722.

(23) Lim, L. Y.; Liu, N.; Cui, Y.; Toney, M. F. *Chem.Mater.* **2014**, 140606104017002.

(24) Hatchard, T. D.; Dahn, J. R. *J. Electrochem. Soc.* **2004**, *151*, A838.

(25) Li, J.; Dahn, J. R. *J. Electrochem. Soc.* **2007**, *154*, A156.

(26) Graetz, J.; Ahn, C. C.; Yazami, R.; Fultz, B. *J. Electrochem. Soc.* **2004**, *151*, A698.
(27) Yoon, S.; Park, C.-M.; Sohn, H.-J. *Electrochem. Solid-State Lett.* **2008**, *11*, A42.
(28) Ogata, K.; Salager, E.; Kerr, C. J.; Fraser, A. E.; Ducati, C.; Morris, A. J.; Hofmann, S.; Grey, C. P. *Nat Commun.* **2014**, *5*, 3217.
(29) Wang, X.-L.; Han, W.-Q.; Chen, H.; Bai, J.; Tyson, T. A.; Yu, X.-Q.; Wang, X.-J.; Yang, X.-Q. *J. Am. Chem. Soc.* **2011**, *133*, 20692.
(30) Hammersley, A. P.; Svensson, S. O.; Hanfland, M.; Fitch, A. N.; Hausermann, D. *High Pressure Res.* **1996**, *14*, 235.
(31) Qiu, X.; Thompson, J. W.; Billinge, S. J. L. *J. Appl. Crystallogr* **2004**, *37*, 678.
(32) Farrow, C. L.; Juhás, P.; Liu, J. W.; Bryndin, D.; Božin, E. S.; Bloch, J.; Proffen, T.; Billinge, S. J. L. *J. Phys.: Condens. Matter* **2007**, *19*, 335219.
(33) Johnson, Q.; Smith, G. S.; Wood, D. *Acta Crystallogr.* **1965**, *18*, 131.
(34) Gladyshevskii, E. I.; Oleksiv, G. I.; Kripyake, P. I. *Sov. Phys. Crystallogr.* **1964**, *9*, 269.
(35) Hopf, V.; Schäfer, H.; Weiss, A. *Z. Naturforsch., B: Chem. Sci.* **1970**, *25*, 653.
(36) Hopf, V.; Müller, W.; Schäfer, H. *Z. Naturforsch., B: Chem. Sci.* **1972**, *27*, 1157.
(37) Bekaert, E.; Robert, F.; Lippens, P. E.; Ménétrier, M. *J. Phys. Chem. C* **2010**, *114*, 6749.
(38) Schäfer, H.; Eisenmann, B.; Müller, W. *Angew. Chem. internat. Edit* **1973**, *12*, 695.
(39) Mosqueda, H. A.; Vazquez, C.; Bosch, P.; Pfeiffer, H. *Chem. Mater.* **2006**, *18*, 2307.
(40) Ungár, T. *Scripta Materialia* **2004**, *51*, 777.
(41) Walters, J. K.; Newport, R. J. *Phys. Rev. B: Condens. Matter Mater. Phys.* **1996**, *53*.
(42) Wojdyr, M. *J. Appl. Cryst.* **2010**, *43*, 1126.
(43) Chan, C. K.; Zhang, X. F.; Cui, Y. *Nano Lett.* **2007**, *8*, 307.
(44) Obrovac, M. N.; Christensen, L. *Electrochem. Solid-State Lett.* **2004**, *7*, A93.
(45) Jamnik, J.; Maier, J. *Phys. Chem. Chem. Phys.* **2003**, *5*, 5215.

Chapter 3

Understanding the (de) lithiation mechanism of micron-sized Ge anodes by XRD, PDF, and ^{7}Li MAS NMR: beyond the first lithiation

3.1. Introduction

In the previous chapter, the lithiation mechanism of synthesized micron-sized Ge anodes was investigated with X-ray diffraction (XRD), pair distribution function (PDF) analysis, and *in/ex situ* high-resolution ^{7}Li solid-state nuclear magnetic resonance (NMR), utilizing the structural information and spectroscopic fingerprints obtained by characterizing a series of relevant Li_xGe_y model compounds. It was found that the lithiation process of micron-sized Ge anodes involves the initial formation of a Li_7Ge_3 phase (space group $P3_12$) through a two-phase reaction process. The Li_9Ge_4 phase, postulated by previous studies, was not detected.[1,2] Li_7Ge_3, converts to Li_7Ge_2 via a series of highly disordered phases. All of these phases contain columns of isolated Ge, dumbbell type Ge-Ge bonds and isolated Li, with the relative proportions varying as lithiation proceeds. Eventually, Li_7Ge_2-like short–to-medium range environments are observed, indicating that most of the Ge-Ge bonds have been broken. At this point, the nucleation and growth to form crystalline $Li_{15}Ge_4$, occurs. This phase can be further lithiated, likely to form $Li_{15+\delta}Ge_4$ at the end of lithiation. No indication of $Li_{22}Ge_5$, as proposed by one prior study[1,2], is found.

This chapter will focus on a delithiation process and the structural transformations that occur in subsequent (de) lithiation cycles. Previous studies[1,3-6] suggested the absence of crystalline Ge phase at the end of delithiation, while Graetz *et al.* [2] observed the strong crystalline Ge diffraction signals (111) upon delithiation. Yoon *et al.*[1] suggested a three-step delithiation mechanism, the reverse of the processes observed on lithiation ($Li_{15}Ge_4$ + $Li_{22}Ge_5$ → Li_7Ge_2 → Li_9Ge_4 → nano-sized Ge) for a carbon-coated germanium composite electrode, based on *ex-situ* XRD and HRTEM analyses. Most *in-situ* XRD[3], TEM[5] and XRD/XAS[6] analyses of Ge electrodes reported that the delithiation process occurred via the formation of a series of amorphous Li-Ge intermediates, eventually forming an amorphous Ge phase (crystalline $Li_{15}Ge_4$ → amorphous Li_xGe → amorphous Ge). A recent *in situ* XRD, TEM and ^{7}Li NMR study[7] proposed that a four-step lithiation process (crystalline Ge →amorphous Li_9Ge_4 →amorphous Li_7Ge_2 → crystalline $Li_{15}Ge_4$ + amorphous Li_7Ge_2 → crystalline $Li_{15+\delta}Ge_4$ (metastable) + amorphous Li_7Ge_2 (metastable)) occurs for germanium nanorods embedded in multiwall carbon nanotubes.

Upon delithiation, a reverse conversion process occurred and finally formed amorphous Ge at the end of charge.

Ge exhibits a severe volume change during cycling, which can cause cracking and a loss of reversible capacity.[8] Weker *et al*.[9] investigated the effect of particle size on capacity retention, showing that the larger particles (> 10 μm) are able to maintain electrical contacts with current collectors after the first cycle, since the larger particles have more points of contacts between germanium particles and binder/carbon matrix due to their large surface areas (per particle). This is somewhat counterintuitive as electrodes containing micron-sized Si particles generally show very poor performance.[1] In this chapter, commercial micron-sized Ge (100 mesh, <149 μm) powder was used as the active material so as to observe the subsequent cycle without significant capacity loss, instead of the smaller synthesized micron-sized Ge powder (*ave*. 1~3 μm). The results are compared with nano-sized Ge particles in the subsequent Chapter. Commercial micron-sized Ge powder is a more promising anode candidate for practical industrial application, in part motivating this study.

Recent studies have shown that a cycle stability and capacity retention are critically dependent on the binder's properties[9-11], similar to Si-based electrodes. Poly (vinylidene fluoride) (PVDF) is considered an inappropriate binder for silicon-based anodes (alloying materials) because it is attached to active materials with only van der Waals forces, which are too weak to accommodate severe volume changes during cycling.[12] Several groups reported that sodium carboxylmethyl cellulose (CMC) and poly (acrylic acid) (PAA) binder show enhanced cycling behavior due to hydrogen bonding between carboxyl groups in CMC or PAA and hydroxyl groups on the Ge surface compared with PVDF binder. [12-15] In addition, PAA offers an increase of elastic modulus in binder system, and copolymerization between CMC and PAA can lead to an improvement of mechanical properties.[12,15]

The aim of this chapter is to provide a deeper understanding of the delithiation process and the structural transformation in subsequent cycles by using *ex-situ* XRD, *ex-situ* PDF, ^{7}Li solid-state NMR, both *in situ* and *ex situ* MAS. SEM analysis of two different micron-sized Ge samples is first performed and then various binders were screened so as to optimize the electrochemistry. *Ex-situ* XRD was used to probe the

long-range structural changes, while *ex-situ* solid-state ^{7}Li NMR and *ex-situ* PDF experiments are employed to help identify the local structures formed in the disordered or amorphous phases, the method having been shown to be highly sensitive to local structure and deviations from stoichiometry of the crystalline phases in the lithium-silicon system.[16-18] By combining two techniques that are sensitive to local Li environments and long-range structural order, we obtain comprehensive insights into the structure of Ge-anodes at various degrees of lithiation/delithiation in the first and subsequent cycles.

3.2 Experimental section

3.2.1. Binder screening test

100 mesh commercial Ge powder (< 149 μm, Alfa Aeser 99.999%) was first analyzed by SEM to confirm particle sizes (A LEO1550, Germany SEM, operating at 20
kV with a Robinson backscatter detector was used.). Binder-screening tests (using PVDF, CMC, and CMC/PAA) were then performed to identify electrode formulations with optimum capacity retention. For consistency, all electrodes were prepared using the same electrode formulation (AM (active material): SP (super P): Binder=70:15:15) and cycled at the same current rate (C/50). Electrodes were fabricated using the slurry coating method and the details of the slurry mixing conditions are shown in Table 3.1.

Table 3.1. Electrode fabrication conditions

Binder	Solvent	Mixing method
PVDF (polyvinylidene fluoride) Kynar Flex 2801-00	NMP (0.12mg PVDF/1ml NMP)	Magnetic stirring/overnight mixing
CMC (carboxylmethyl cellulose sodium salt) *ave*. M_w=700,000, Aldich	Water (10mg CMC/1ml water)	High Energy ball milling/10min
CMC:PAA=1:1 PAA (Polyacrylic acid) 25wt %, Alfa Aesar	Water (10mg CMC/1ml water)	High Energy ball milling/10min

3.2.2. Electrochemistry

Electrochemically-cycled electrode samples for *ex-situ* experiments (XRD, NMR and PDF) were prepared using CR 2032 –type coin cells. The positive electrodes were formulated from 70% germanium powders (100 mesh, Alfa Aeser 99.999%) as the active material, 15 % Super P (Timcal) as a conducting matrix, and 15% mixed binder, *i.e*., CMC (sodium carboxylmethyl cellulose with *ave*. M_w=700,000, Aldich): PAA (Polyacrylic acid 25wt %, Alfa Aesar) in a 1:1 in weight ratio. The mixture was placed into a zirconia ball-milling jar and 1 mg water per 10 mg of CMC was added. The mixture was milled for 10 min in a SPEX SamplePrep8000 Mixer/Mill high-energy ball mill to form homogeneous slurry. This slurry was coated on a Cu foil, dried at 100 °C for 10 minutes in a convection oven (Grieve co.) and then at 60°C for 24 hours in a vacuum oven (Thermo scientific). Coin cells were assembled in an Ar-filled glove box using Li metal foil as the negative electrode. 1M $LiPF_6$ in a 1:1 volumetric mixture of ethylene carbonate (EC) and dimethyl carbonate (DMC) was used as the electrolyte and a porous glass fiber (GF/B, Whatman) as the separator. The cells were cycled using an Arbin instruments battery cycler with a cycling rate of C/50 (corresponding to discharge to a theoretical capacity of 1623 mAh/g in 50 hours, assuming that $Li_{4.4}Ge$ is the final electrochemical lithiation product[2]) between 0.0 V to 2.0 V at room temperature. After electrochemical cycling to specific cut-off voltages, each cell was dissembled and active material was washed with dimethyl carbonate (DMC, 99+% Sigma-Aldrich) and dried in an Ar-filled glove box.

For *in-situ* NMR experiments, a flexible battery design was used. The positive electrodes were prepared with the same slurry mixture. (100mesh Ge: Super P: CMC/PAA = 70:15:15 in water). The mixture was spread onto a flat glass surface and dried in air.

The dried film (4 mm (width) X 10 mm (length)) was laminated on a carbon-coated Cu mesh and used as the positive electrode. Lithium metal foil of the same dimensions as the positive electrode film and was pressed onto Cu wire mesh and used as the negative electrode. 1M $LiPF_6$ in a 1:1 volumetric mixture of ethylene carbonate (EC) and dimethyl ethyl carbonate (DMC) was used as the electrolyte and a piece of porous glass fiber as the separator. Components were assembled and sealed in a plastic bag

(Kapak Corporation, type 500) inside the glove box. This flexible plastic battery cell was placed in a 5-mm in diameter NMR coil of a static probe inside a magnet and connected with the external battery cycler. A Bio-Logic Science Instruments VSP potentiostat/galvanostat was used to electrochemically cycle the bag-cell battery within the voltage window of 0.0V -2.0V.

3.2.3. X-ray Diffraction

Diffraction patterns were measured on a Bruker D8 diffractometer using Cu Kα irradiation (λ=1.54 Å) with a scan rate of 3°/min from a 2θ range of 10° to 80°. Samples were sealed with an airtight cover under Ar atmosphere before being loaded into a XRD holder.

3.2.4. *Ex-situ* Pair distribution function analysis

Dried *ex situ* battery samples for PDF analysis were loaded into 1-mm diameter Kapton capillaries in an Ar-filled glovebox and sealed with epoxy. Total scattering data were acquired at the dedicated PDF beamline 11-ID-B at the Advanced Photon Source, Argonne National Laboratory. High-energy X-rays (~58 keV, λ = 0.2128 Å) were used in combination with a large amorphous-silicon based area detector (Perkin-Elmer) to collect X-ray scattering data to high values of momentum transfer ($\mathbf{Q}_{max} \approx 23$ Å). The scattering images were reduced to one-dimensional data within FIT2D[19] using CeO_2 as a calibration standard. The data were corrected for background scattering, Compton scattering and detector effects within pdfgetX2[20] and Fourier transformed to get **G**(**r**), the PDF. No attempt was made to subtract the carbon signals from the total PDF pattern. Least-squares refinements of structures against PDF data were performed in PDFGui in the distance range of 0 – 30 Å[21]. The initial value for the Q_{damp} parameter was set as 0.045 and refined against the data for crystalline Ge, and the atomic displacement parameters were set to intial values of $U_{11}=U_{22}=U_{33} = 0.005Å^2$ (constrained to be equal for all the Ge and Li atoms) and $U_{12}=U_{23}=U_{13}.=0$. Q_{damp}, lattice parameters, the linear atomic correlation factor (delta 1), and anisotropic temperature factors (U_{11}, U_{22}, U_{33}) were refined. The fractional coordinates factors (x, y, z) were not refined here. The initial refinements of each PDF pattern assume a single pure phase, however,

incorporation of a second minor phase significantly improved the refinement quality of some patterns, as indicated by reduced refinement quality factors, i.e., the R_w values. Note that the values of R_w-factors obtained for PDF refinements are higher than those for a Rietveld refinement of similar merit.

3.2.5. *Ex situ* ^{7}Li MAS NMR

Ex-situ battery samples were packed in 1.3 mm diameter Zirconia rotors in an Ar-filled glove box. High-resolution ^{7}Li MAS NMR spectra were acquired on a Varian InfinityPlus-500 MHz spectrometer at a magnetic field of 11.7 T, with a 1.3 mm MAS probe at a spinning speed of 50 kHz. Spectra were acquired using a rotor-synchronized spin-echo sequence (90°-τ-180°-τ-acq), where τ-values were set to be equal to one rotor period, i.e., 20 μs. The 90^o pulse length was 2.2 μs and the recycle delay 10 s. ^{7}Li spectra were referenced to a 1M ^{7}LiCl solution at 0 ppm. ^{7}Li MAS NMR spectra were normalized for analysis on the basis of the number of acquisitions and sample mass.

3.2.6. *In situ* ^{7}Li NMR

In-situ ^{7}Li experiments were carried out on a Tecmag Redstone 200 MHz spectrometer at a magnetic field of 4.7 T with a static probe. A one-pulse sequence with a 90^o pulse length of 2 μs and a recycle delay of 10 s was used. ^{7}Li spectra were referenced to a 1M ^{7}LiCl solution at 0 ppm. The Ge/Li battery was cycled at a rate of C/50.

3.3. Results and Discussion

3.3.1. Particle and Binder screening

SEM images were collected to investigate the particle sizes and morphologies of commercial 100 mesh Ge and synthesized micron-sized Ge (Figure 3.1).

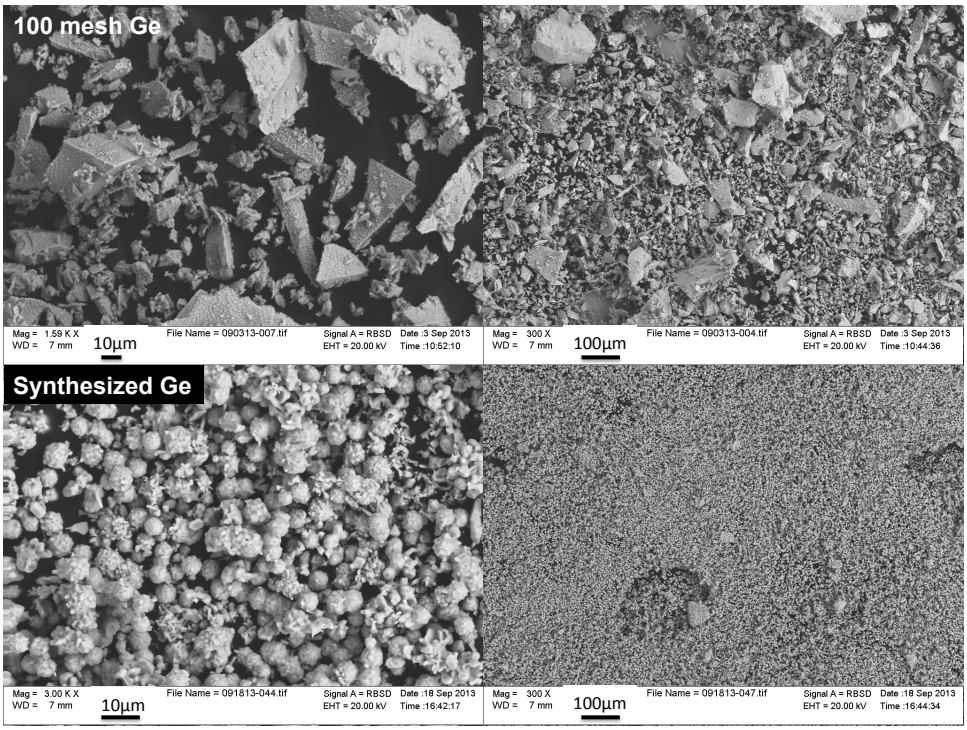

Figure 3.1. SEM images showing the particle size distribution of each Ge powder. Upper images are a 100 mesh commercial Ge power and lower images are synthesized Ge powder.

Commercial Ge powder, which will be referred to a 100mesh Ge in the subsequent text, has a broad particle size distribution. As shown in Figure 3.2a, the best capacity retention in the first delithiation is obtained when using CMC/PAA binder. The capacity retention of both CMC/PAA and PVDF binder systems at a C/50 rate was tested and the results are shown in Figure 3.2b.

The capacity of CMC/PAA binder system remained relatively stable until 10 cycles, while significant capacity fade in PVDF binder system was observed after the first cycle. Thus, electrodes with CMC/PAA binder for *ex-situ* experiments were employed for further investigations.

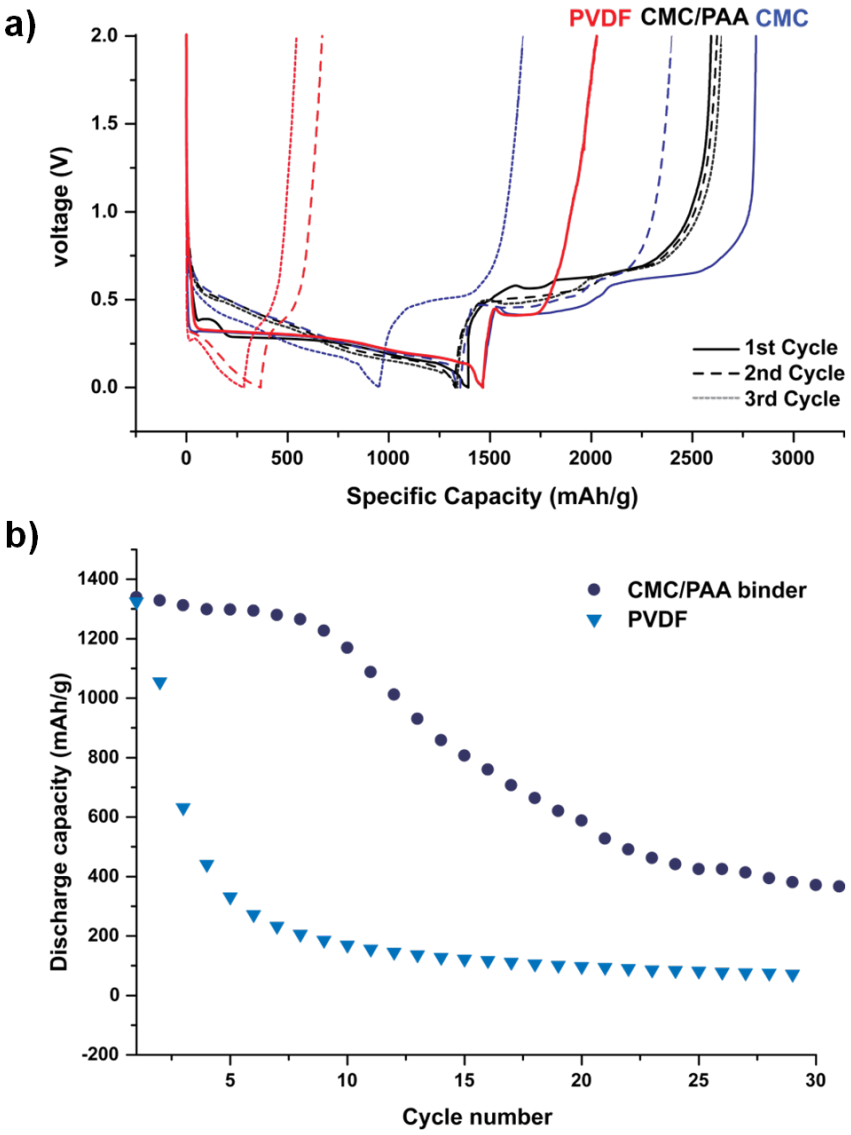

Figure 3.2. a) Voltage profiles of the 100mesh Ge with different binder systems at a C/50 rate. b) Discharge capacity vs. cycle number for 100mesh Ge with CMC/PAA and PVDF binder. All cells were tested in the voltage range of 0.0~2.0 V versus Li/Li^+.

3.3.2. Electrochemistry

Figure 3.3a shows the 1st and 2nd cycle electrochemical profile of 100mesh Ge vs. Li/Li^+ down to 0 mV with a rate of C/50. At the first discharge, consistent with previous studies[22] of the synthesized micron-sized Ge (chapter 2), lithiation starts with an initial steep drop in potential to 260 mV with an inflection appearing at approximately 350 mV. Two flatter regions are followed, the first flatter region is at around 300~200mV and the second at around 200~100mV, and finally a fast drop to 0mV. The overall voltage profile ranges in the first discharge are lower than the synthesized micron-sized Ge (chapter 2), indicating a particle-size dependence of the initial lithiation potential consistent with prior work.[9,23] A recent *in-situ* TXM study,[9] (hard X-ray transmission X-ray microscopy), suggested that larger particles show the beginning of fracture at a lower voltage than smaller particles due to the barrier for volume expansion upon lithiation. 100 mesh Ge has a broader particle size distribution and much larger primary particles (SEM images are shown in Figure 3.1), thus average initial lithiation voltage ranges are lower than for synthesized micron-sized Ge (Chapter 2).

The first charge process starts with a steep rise in potential to approximately 450mV with an inflection appearing at around 480mV; this is followed by the first flatter region between 440 and 480mV, after which the potential rises gradually until 600mV. This first steep rise on charge is similar to that observed for Si,[17,18] suggesting a large overpotential due to the difficulty of the formation of amorphous Ge phase from crystalline $Li_{15}Ge_4$ phase. The second flatter region appears at around 600 and 700 mV and the potential rises again until it reaches the upper limit used here of 2.0 V.

The specific capacities of the subsequent discharge/charge cycle are slightly reduced. On the second discharge, lithiation processes start with a rapid drop in potential to 550mV, which is followed by a sloping region between 500 and 100mV, indicating that the initial lithiation process is easier than in the first cycle due to the reduced particle size, increased porosity of particles, and the amorphous nature of the Ge formed at the top of charge, accelerating the Li^+ diffusion. [6,9,24] This sloping region consists of a sloping region at 500~300mV and a flatter region at 300~100mV. The potential then drops rapidly to 0V. The first sloping region (500~300mV) shows a more sloping potential profile compared with the first discharge, (see dQ/dV plot) suggesting that the

lithiation process may happens at a range of potentials, indicating a range of germanium environments with a range of reactivity, unsurprising considering the amorphous Ge matrix. The dQ/dV plot shows that the 300 –100 mV process is similar in the 1st and 2nd discharges. The voltage profile on delithiation in the second cycle is similar to that on the 1st charge, starting with a steep rise to 450mV and followed by the two flatter regions with a smaller inflection at around 500mV.

Differential capacity (dQ/dV) profiles of the 1st and 2nd cycles show the characteristic Ge lithiation processes and are plotted in Figure 3.3b. On the first discharge, the lithiation pathway of 100 mesh Ge resembles the synthesized micron-sized Ge (chapter 2), except a lower voltage range and four clearly defined processes occur at 350, 270, 150, and 100 mV, where structural phase transformations take place (compared to 500, 350, 200, and 50 mV for the synthesized micron-sized Ge). By analogy with the results presented in Chapter 2, the first process at 350 mV is associated with a SEI formation and reaction with GeO_x and the sharp peak at 270mV related to the formation of Li_7Ge_3. The broad shoulder at 150 mV corresponds to a gradual structural transformation from Li_7Ge_3 to Li_7Ge_2 and the peak at 100 mV is most likely due to the formation of crystalline $Li_{15}Ge_4$ phase. During the delithiation process in the first cycle, one sharp peak and broad bump appears at 450 and 640 mV, respectively.

Lim *et al.*[6] also observed the two peaks at 497 and 630 mV in dQ/dV plot upon delithiation and suggested that the peak at 497 mV indicates the phase transformation from crystalline $Li_{15}Ge_4$ to a heterogeneous amorphous Li_xGe phase based on the decreasing the intensity of crystalline $Li_{15}Ge_4$ (310) diffraction peak. The peak at 630mV corresponds to the formation of amorphous Ge phase as evidenced from EXAFS fittings. In the second discharge, the peak at 350mV disappears, supporting the formation of SEI in the first cycle, and three broad lithiation processes exist at approximately 400, 150, and 100mV, indicating a similar lithiation pathway occurs in a subsequent cycle. The second charge dQ/dV plot also shows similar two peaks (a sharp peak and a broad hump) to the first charge differential capacity profile.

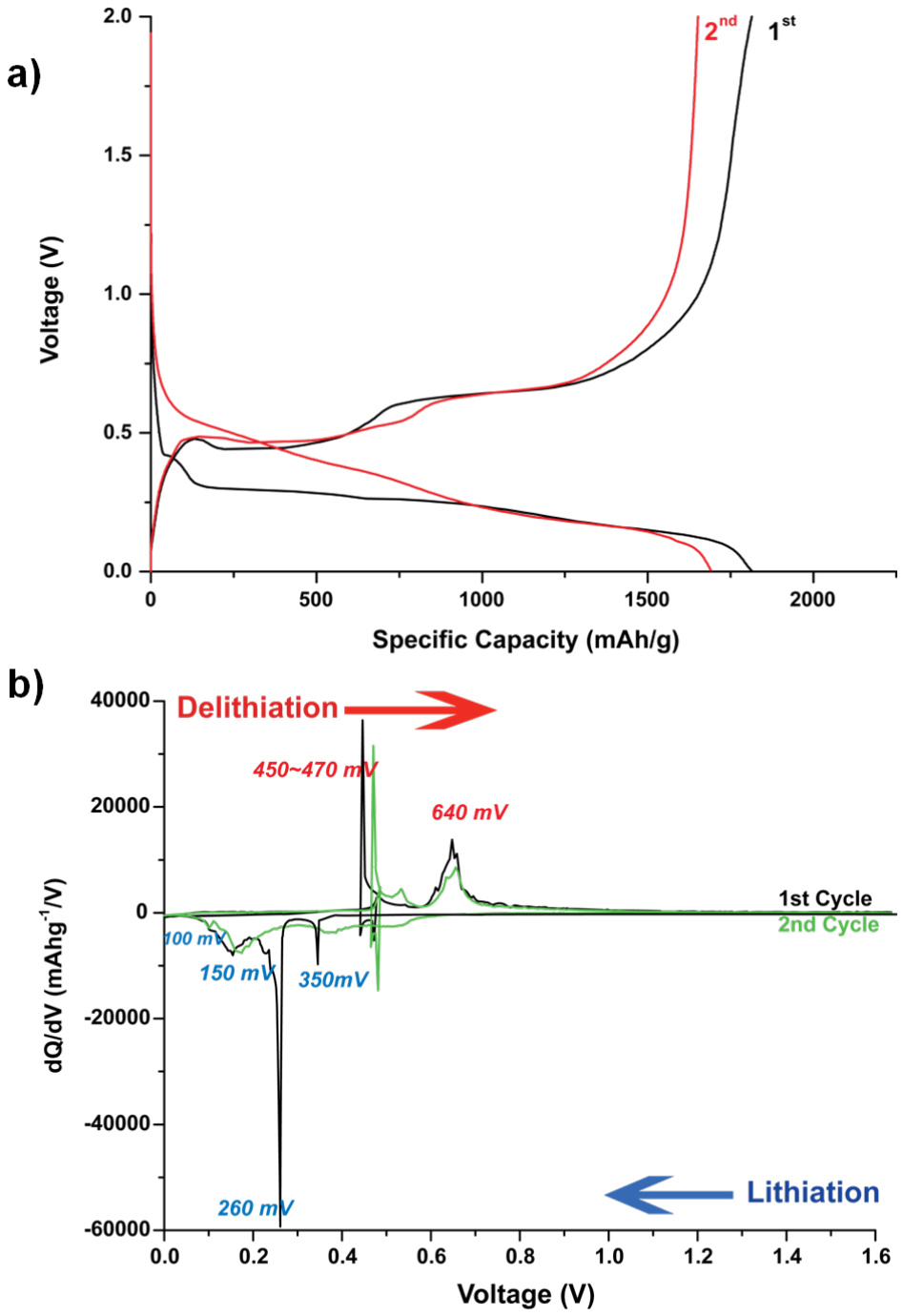

Figure 3.3. a) Voltage profiles of the 1st and 2nd (de) lithiations of 100mesh Ge at a C/50 rate. b) The differential capacity dQ/dV plot of 1st and 2nd cycle 100mesh Ge. All the cells were tested in the voltage range of 0.0~2.0V versus Li/Li^+.

3.3.3. X-ray Diffraction (XRD)

XRD patterns of the first and second cycles Ge anodes obtained at different voltages are shown in Figure 3.4. Reminiscent of the first discharge observed for the synthesized micron-sized Ge (Chapter 2), at the start of the first discharge, the reflections from the crystalline Ge phase ($Fd\bar{3}m$) dominate but decrease in intensity on lithiation, and disappear completely by 200mV indicating full conversion of the crystalline Ge to other species. The reflections from the $P3_12$ Li_7Ge_3 phase appear at 250mV and are dominant at 200 mV. These reflections decrease in intensity at 150mV.

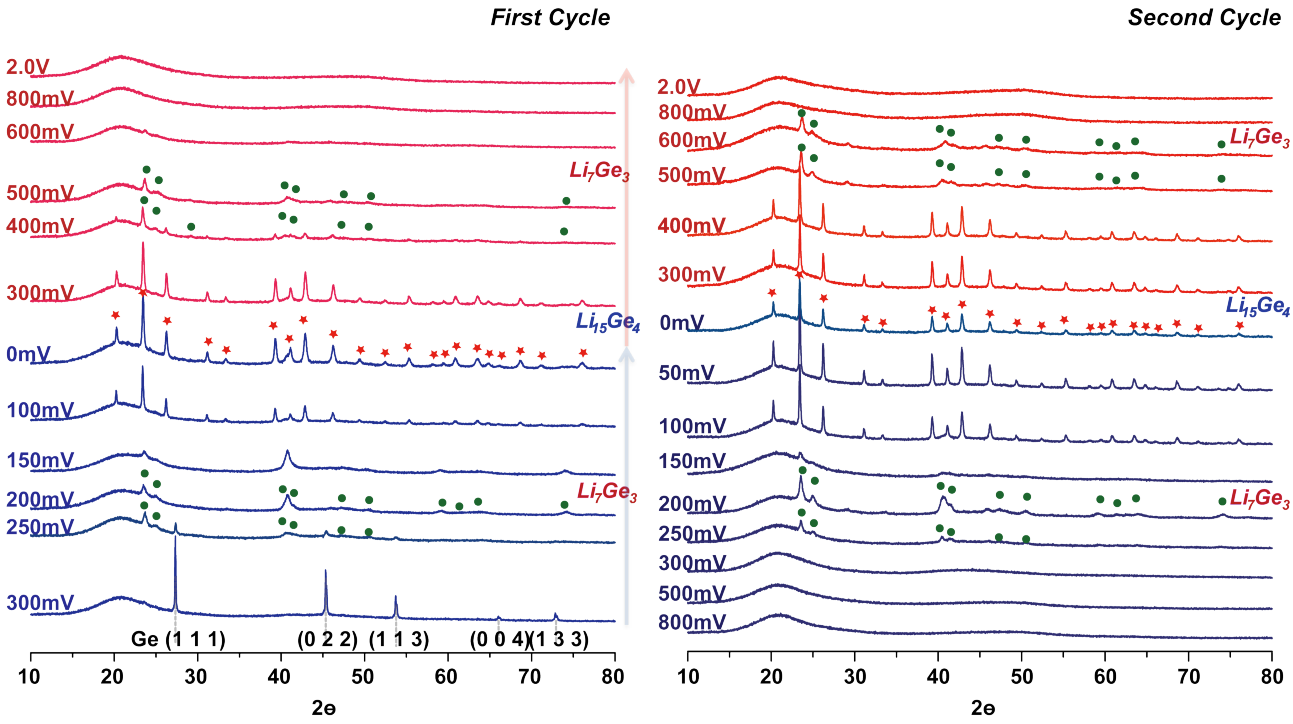

Figure 3.4. *Ex-situ* XRD patterns (λ=1.54 Å) of the first/second (de) lithiation of 100mesh Ge electrodes at a rate of C/50 (lithiation: blue; delithiation: red). The corresponding states of charge for the selected XRD patterns are indicated on the electrochemical profiles. Major reflections from Ge are indexed and major reflections from Li_7Ge_3 (•), $Li_{15}Ge_4$ (★) are marked. The broad background centered at 2θ=20° comes from the sample holder.

Between 200 and 100 mV, the reflections from Li_7Ge_3 start to decrease and almost disappear at 150mV, and a new phase with a major intense broad reflection at 2θ=41° and three minor traces at 24°, 59°, and 74° (λ=1.54 Å) suggesting that Li_7Ge_3 converts to Li_7Ge_2 via a series of disordered phases based on our previous study (chapter 2) and dQ/dV plot (Figure3.3b). This is a similar to that the observed for the synthesized micron-sized Ge (chapter 2, at 200mV), however, here, a potential range (150mV) is lower due to the effect of having a range of particle sizes: the potential at which this solid-solution like mechanism takes place is highly dependent on the size of the particles. The reflections from crystalline $Li_{15}Ge_4$ emerge at 100mV and are present until the end of discharge at 0mV.

Upon delithiation, the intensities of crystalline $Li_{15}Ge_4$ reflections decrease and almost disappear at ~400mV in the steep rising voltage region before the first plateau. The first flatter region with a sharp peak in the dQ/dV plot is observed in the electrochemical profile, indicating a two-phase reaction occurs. Li_7Ge_3 reflections emerge at 400mV and dominate at 500mV at this region A recent *in-situ* XRD and XAS study[6] suggested the conversion from $Li_{15}Ge_4$ to various amorphous Li_xGe phase at 370~492mV. In this study, we can tentatively attribute this flatter region to the two-phase reaction from crystalline $Li_{15}Ge_4$ to Li_7Ge_3 based on our XRD results.

Between 600mV and 800mV, the second flatter region with a broad hump in the dQ/dV plot exists, suggesting that Li_7Ge_3 transforms to amorphous Ge-phase. No crystalline Ge signals are detected beyond 600mV. Figure 3.5 shows a comparison between the XRD patterns of crystalline Ge at 300mV and amorphous Ge phase at 2V at the end of the 1st charge.

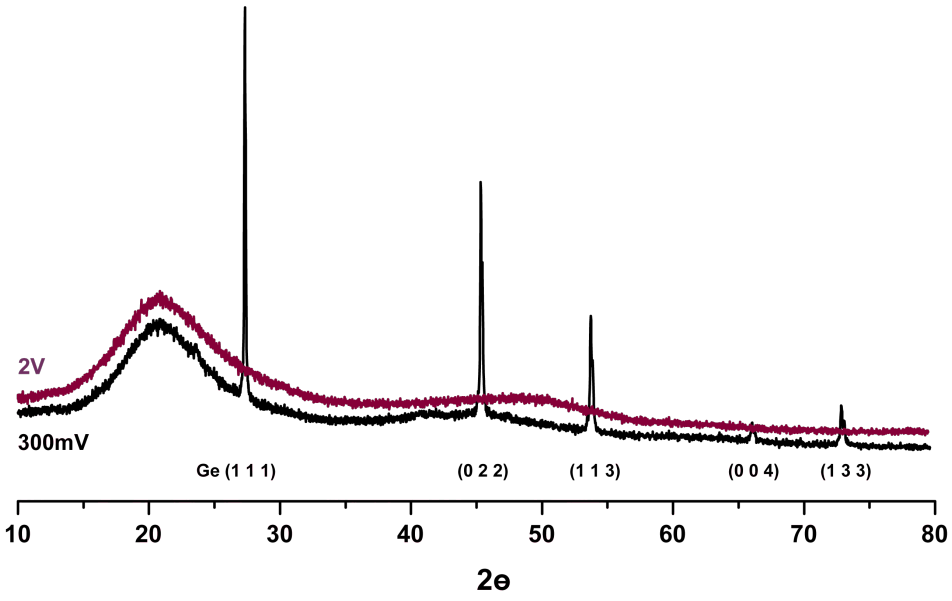

Figure 3.5. A comparison of XRD patterns (λ=1.54Å) between at 300 mV (lithiation) and at 2V(delithiation) of the first cycled 100 mesh Ge electrodes at a rate of C/50. The broad background centered at 2θ=20° comes from the airtight sample holder.

After the first cycle, crystalline Ge phase was completely amorphized since no crystalline Ge reflections are observed at the end of delithiation (at 2V) in XRD, so lithiation in the second cycle occurs in amorphous Ge network and lithium diffusivity is also much faster due to increased the porosity than crystalline Ge matrix.

No reflections are detected until 250 mV, indicating that the second cycle commences in an amorphous Ge matrix. The reflections from Li_7Ge_3 phases appear at 250mV and continue to grow stronger at 200mV. Between 200 and 100mV, Li_7Ge_3 transforms to an amorphous phase. At 150mV, almost no other crystalline phase is observed, except that there is a trace of the reflection from Li_7Ge_3 phase at around 2θ=24°. On the basis of the previous study and dQ/dV plot, we postulate the transformation to Li_7Ge_2 occurs in this region. This is further discussed in the context of the PDF and NMR results later in this chapter. During the first discharge, broad Bragg reflections (a major and broad reflection at 2θ=41° and three minor ones at 24°, 59°, and 74°) are still observed at 150mV, indicating the existence of partial ordering along certain directions. However, no major and broad reflection at 2θ=41° is observed in the second

cycle, in contrast to the first cycle, only the trace of the reflection from Li_7Ge_3 exists, suggesting the absence of partial ordering within the amorphous Li_7Ge_2-like phase. Further lithiation beyond 150mV, the $Li_{15}Ge_4$ crystalline phase reappears at 100mV and is maintained until the end of discharge.

On the second charge, a steep rise region between 0 and 400mV contains reflections from crystalline $Li_{15}Ge_4$ phase. Following this, the reflections from Li_7Ge_3 are detected and decrease at the first flatter region between 500 and 600 mV. This supports a two-phase process from crystalline $Li_{15}Ge_4$ to Li_7Ge_3 at this region. Further delithiation follows a similar pathway to the first cycle.

3.3.4. *Ex-situ* PDF analysis

Experimental PDF patterns, obtained at various stages of (de) lithiation for the first and second cycles, are shown in Figure 3.6 and 3.7 (extended ranges). The clear PDF patterns of crystalline Ge are observed below 40 Å. The sharp peak at 2.5 Å is characteristic of crystalline Ge-Ge bond and two other peaks at 3.8 Å and 4.4 Å correspond to the next nearest Ge-Ge correlations in crystalline cubic Ge. On initial lithiation at 350 and 300mV, r_{max} reduces to around 40 Å, indicating a loss of correlation between more distant Ge atoms. As the discharge proceeds to 150mV, the peak at 2.5 Å decreases in intensity, while a new broad peak at 2.7 Å from Li-Ge correlations emerges. Two other peaks at 3.8 and 4.4 Å are shift to larger values, indicating the formation of Ge-Ge dumbbells local structures with some degree of alignment, such as Li_7Ge_3 or $Li_{13}Ge_5$ and Li_8Ge_3.

Upon further lithiation to 0mV, the peak at 2.5 Å is barely visible and a new broad peak at 4.7 Å is observed, which is characteristic of the first Ge-Ge nonbonded distance in Li_7Ge_2 and $Li_{15}Ge_4$, indicating that the majority of Ge exists as isolated atoms.

On charge to 300mV, the signature peak at 4.7 Å of non-bonded Ge-Ge is still observed, suggesting the presence of isolated Ge phases at the steep rising region in electrochemical profiles. At 400mV, still during the steep plateau, the broad peak at 4.7 Å splits into two peaks with the peak at 2.5 Å growing, indicating the formation of Ge-Ge dumbbell correlations, consistent with the results from XRD. The reformation of this peak in conjunction with the intense peak at 2.5 Å indicates the formation of Li_7Ge_3. There is no significant evidence in this *ex situ* study for Li_7Ge_2 being reformed in this region. This is in contrast to the work of Tang *et al*,[7] who showed the brief reformation of Li_7Ge_2 on charge. However, as Li_7Ge_2 is a metastable phase, observation of this phase using *ex situ* measurements is more difficult than *in-situ* experiments. The peak at 2.5 Å is more intense at 500mV. Beyond 600mV, two peaks merge and shifting to a broad peak around 4 Å.

At the end of charge, the r_{max} significantly reduces to around 12 Å and the only three peaks at 2.5 (sharp), 4 and 6 Å (broad) are observed, indicating that crystalline cubic Ge phase is completely absent. These dominant peaks correspond to distances in amorphous Ge[25], which has been studied by neturon PDF, and proposed to consist of a

disordered tetrahedral network. After the first cycle, the total loss of long-range order indicates that almost complete amorphization of crystalline Ge structure.

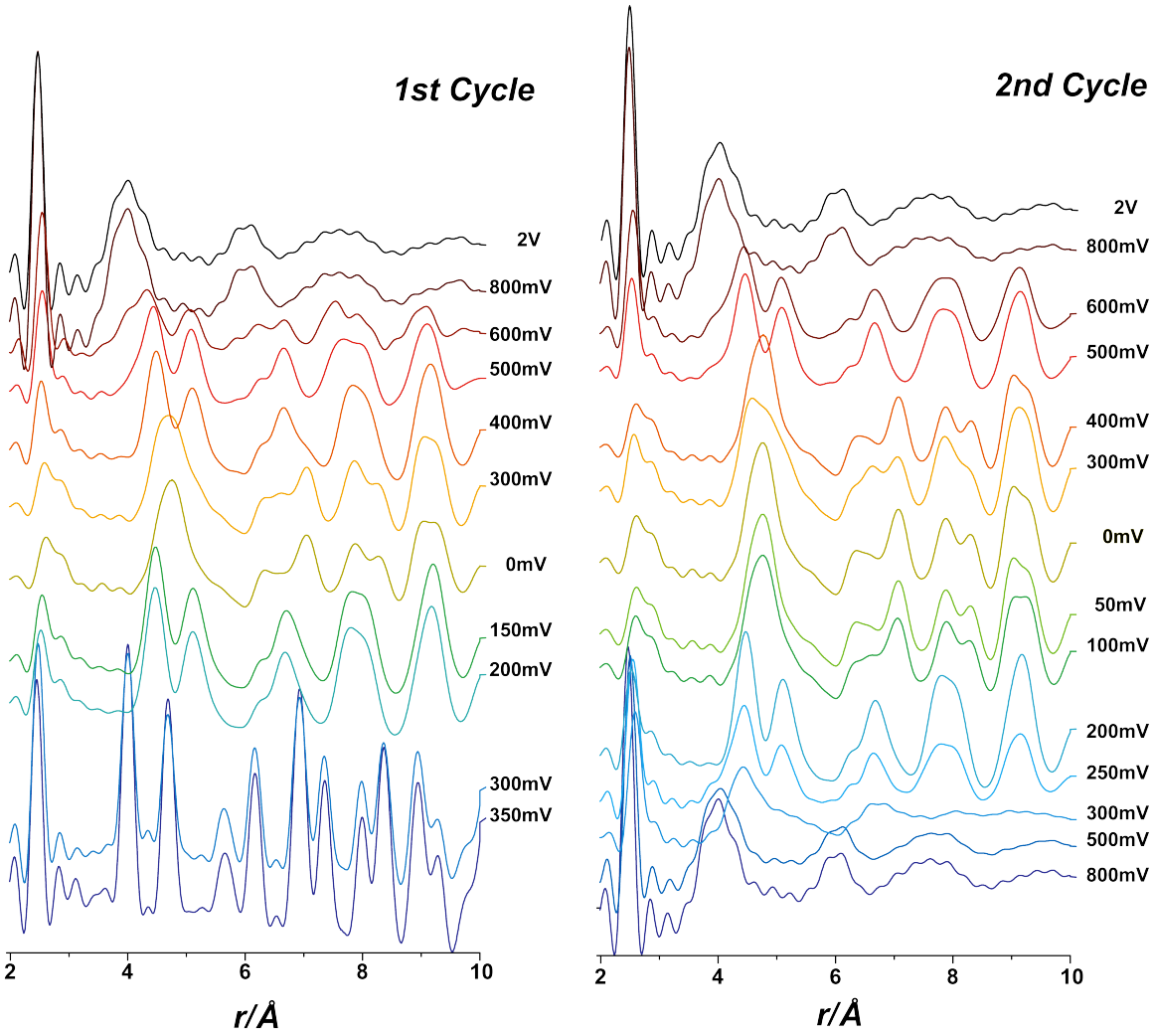

Figure 3.6. *Ex-situ* PDF patterns of the first/second (de) lithiation of 100mesh Ge electrodes at a rate of C/50.

During the second lithiation, XRD results suggest that a similar lithiation pathway to the first cycle occurs. At the early stages of discharge, the PDF patterns of amorphous Ge are only observed at 800 and 500mV. The peak at 4 Å shifts to larger values at 300mV and splits into two peaks at 250mV. On further lithiation to 200mV, these two peaks at 4.3 and 5.1 Å continue to grow stronger. Beyond 100mV, two peaks merge into the broad characteristic peak at 4.7 Å, indicating the formation of isolated Ge phases. In addition, the sharp peak at 2.5 Å, corresponding to Ge-Ge bonds, also disappears by

200mV; the broad peak at 2.7 Å from Li-Ge correlations grows and is clearly visible after 100mV. At the second charge, delithiation pathway is similar to the process observed in the first delithiation.

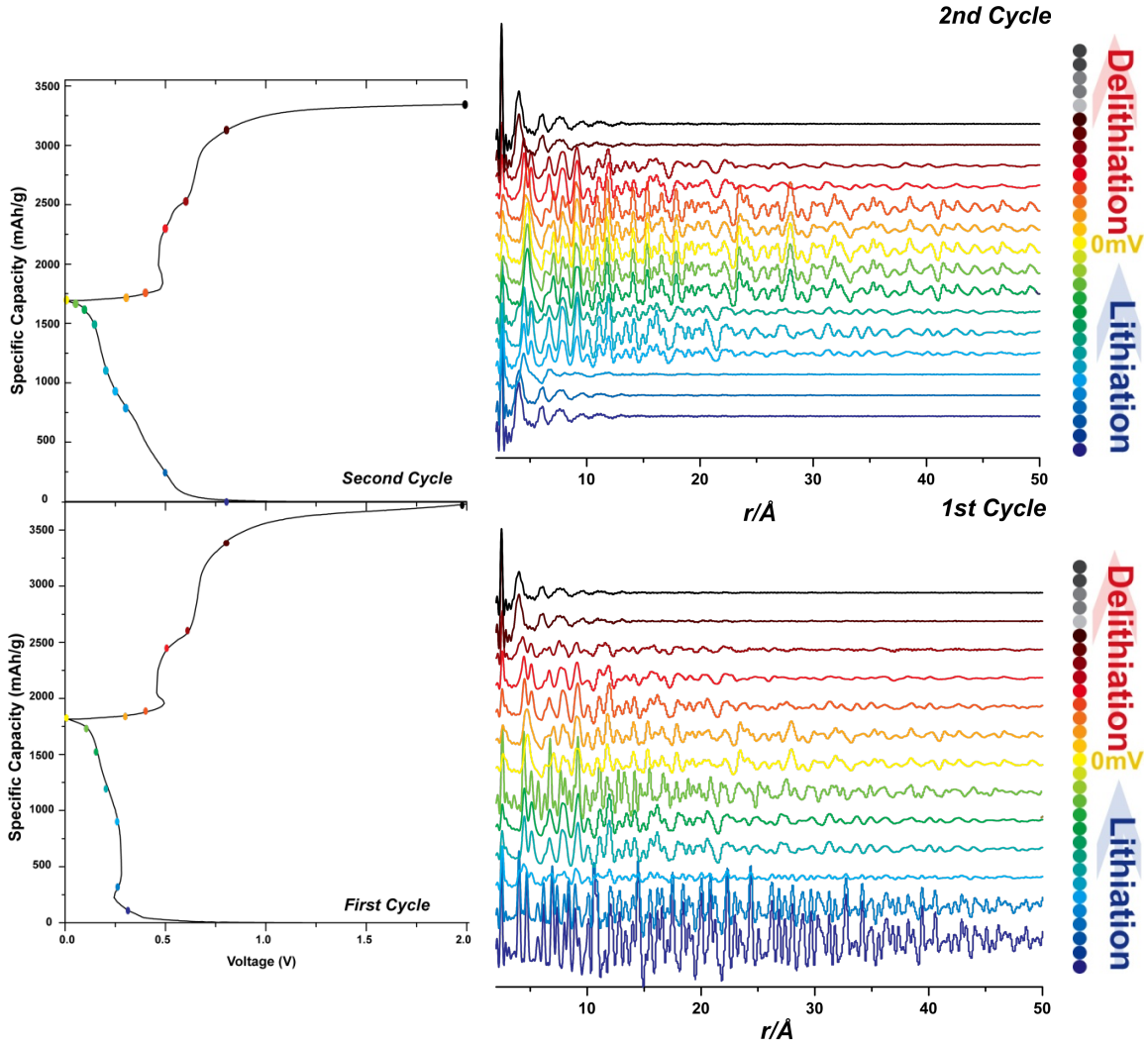

Figure 3.7. *Ex-situ* PDF patterns of the first and second (de) lithiation of 100 mesh Ge electrodes at a rate of C/50.

Quantification of the ratio of phases present was obtained by performing least-squared refinements against PDF data. The phase compositions at different (de) lithiation states from the refinement results are summarized in Table 3.2 (first cycle) and 3.3 (second cycle). Refinement of a Ge-model structure against PDF data for the pristine electrode gives a good fit, with relatively few changes to structural parameters.

At early discharge (350mV), the crystalline Ge phase exists, but the long-range of Ge-Ge correlations are weak as the long-range structure breaks down. As lithium inserts Ge matrix, Ge is converted into Li_7Ge_3 and at 300mV, there is already a significant fraction (0.35) of Li_7Ge_3 present. At 200mV, complete conversion to Ge-Ge dumbbells structures and isolated Ge atoms occurs and the best fit to the PDF pattern is obtained when the phase Li_8Ge_3, comprising of Ge-Ge dumbbells with a bond distance of 2.53 Å and isolated Ge, which was added as a second phase (phase fraction: 0.27). Li_8Ge_3 is a thermodynamically stable phase (on the basis of the DFT studies[26]).The isolated Ge atoms and the Ge-Ge dumbbells in this structure are alternatively aligned and separated by 4 Li atoms along the c-axis. The addition of a $Li_{13}Ge_5$ as a second phase (phase fraction: 0.36), which also contains Ge-Ge dumbbells and isolated Ge, shows a similar fitting result, indicating the commencement of gradual breakage of Ge-Ge bond in Ge-Ge dumbbells. This is in contrast to the micrometric results in Chapter 2, which the best fitting were obtained with $Li_{13}Ge_5$ (major phase) and $Li_{13}Ge_4$ (minor phase). However, the Ge building units in all these phases are similar, and they are all very similar in energy[26], which means that the exact nature and ratio of phases formed is likely to depend on the exact point where the battery is stopped and the overpotential present in the electrode.

Upon further lithiation to 0mV, crystalline $Li_{15}Ge_4$ is observed as a major phase (0.84) along with minor dumbbells. The presence of minor phases may be residual Ge-Ge dumbbell-containing Li_7Ge_3 due to the inhomogeneous nucleation of the $Li_{15}Ge_4$ phase. It is kinetically easier to nucleate and grow the crystalline $Li_{15}Ge_4$ phase from disordered phases (isolated Ge atoms and Ge-Ge dumbbells) than the breakage of Ge-Ge dumbbells (Li_7Ge_3 contains only Ge-Ge dumbbells), by analogy with Si system.[18]

On charge, the initial removal of Li converts $Li_{15}Ge_4$ into Li_7Ge_3, and at 400mV, before the onset of the flat plateau, a significant fraction (0.8) of Li_7Ge_3 is already formed. Further delithiation to 500mV~600mV, a significant loss in correlation length (r_{max} reduces to around 20 Å) is observed and the R_w is increased. This suggests a formation of amorphous phases from Li_7Ge_3. Beyond 800mV, correlations from amorphous Ge phase dominate the PDF patterns and r_{max} significantly reduces to 12 Å. No attempt has been made to model the germanium phases using PDFGui, due to the inherently amorphous

nature of the phases making the use of a crystalline unit cell non-ideal. Further work will include the modeling of these phases using big-box models such as Reverse Monte Carlo methods.

In the second cycle, at the early stages of the lithiation by 300mV, the correlations from amorphous Ge are dominant below 10 Å. As seen in the first discharge, the initial insertion of Li converts a-Ge (0.66) into Li_7Ge_3 (0.34) at 250mV and complete conversion to Ge-Ge dumbbells and isolated Ge structures (dominant Li_7Ge_3 phase and minor $Li_{13}Ge_5$ or Li_8Ge_3) occurs at 200mV. Upon further lithiation, theses mixture of Ge-Ge dumbbells and isolated Ge atoms are converted to crystalline $Li_{15}Ge_4$ phase along with minor Li_7Ge_3 contents until the end of discharge. The correlations from crystalline $Li_{15}Ge_4$ show a significantly increased r_{max} (>50 Å), indicating that nucleation of the crystalline phase becomes easier on increased cycling.

On the second charge, the phase transformations appear to be similar to the first charge process. (Crystalline $Li_{15}Ge_4$→ Li_7Ge_3→ amorphous Ge)

Table 3.2. Germanium phases obtained following the first cycle against Lithium to different voltages cutoffs, with the corresponding R_w values. (Phase ratio is based on mass ratio).

1st Cycle	*a*-Ge	Ge	Li_7Ge_3	$Li_{13}Ge_5$	Li_8Ge_3	Li_7Ge_2	$L_{15}Ge_4$	R_w
2V	1							
800mV	1							
600mV			1					0.7750
500mV			1					0.3874
400mV			0.80				0.20	0.1755
300mV			0.27				0.73	0.1143
0mV			0.16				0.84	0.1595
150mV			0.74		0.26			0.1587
			0.64	0.36				0.1596
200mV			0.73		0.27			0.1379
			0.64	0.36				0.1384
300mV		0.75	0.25					0.1544
350mV		1						0.1098

Table 3.3. Germanium phases obtained following the second cycle against Lithium to different voltages cutoffs, with the corresponding R_w values. (Phase ratio is based on mass ratio).

2nd Cycle	*a*-Ge	Ge	Li_7Ge_3	$Li_{13}Ge_5$	Li_8Ge_3	Li_7Ge_2	$L_{15}Ge_4$	R_w
2V	1							
800mV	1							
600mV			1					0.4953
500mV			0.94	0.06				0.2511
400mV			0.13				0.87	0.1040
300mV			0.37				0.63	0.1172
0mV			0.13				0.87	0.1045
50mV			0.14				0.86	0.1037
100mV			0.23				0.77	0.1117
200mV			0.69	0.31				0.1419
			0.77		0.23			0.1431
250mV			1					0.2375
300mV								
500mV	1							
800mV	1							

3.3.5. *Ex-situ* ^{7}Li NMR

High-resolution solid-state ^{7}Li MAS NMR provides a unique tool for examining local structures and identifying chemical phases, especially, amorphous phases. The characteristic NMR resonances for several Li_xGe_y model compounds were determined in chapter 2. *Ex-situ* ^{7}Li NMR spectra, obtained at various stage of the first and second cycle are shown in Figure 3.8. and Figure 3.9., respectively.

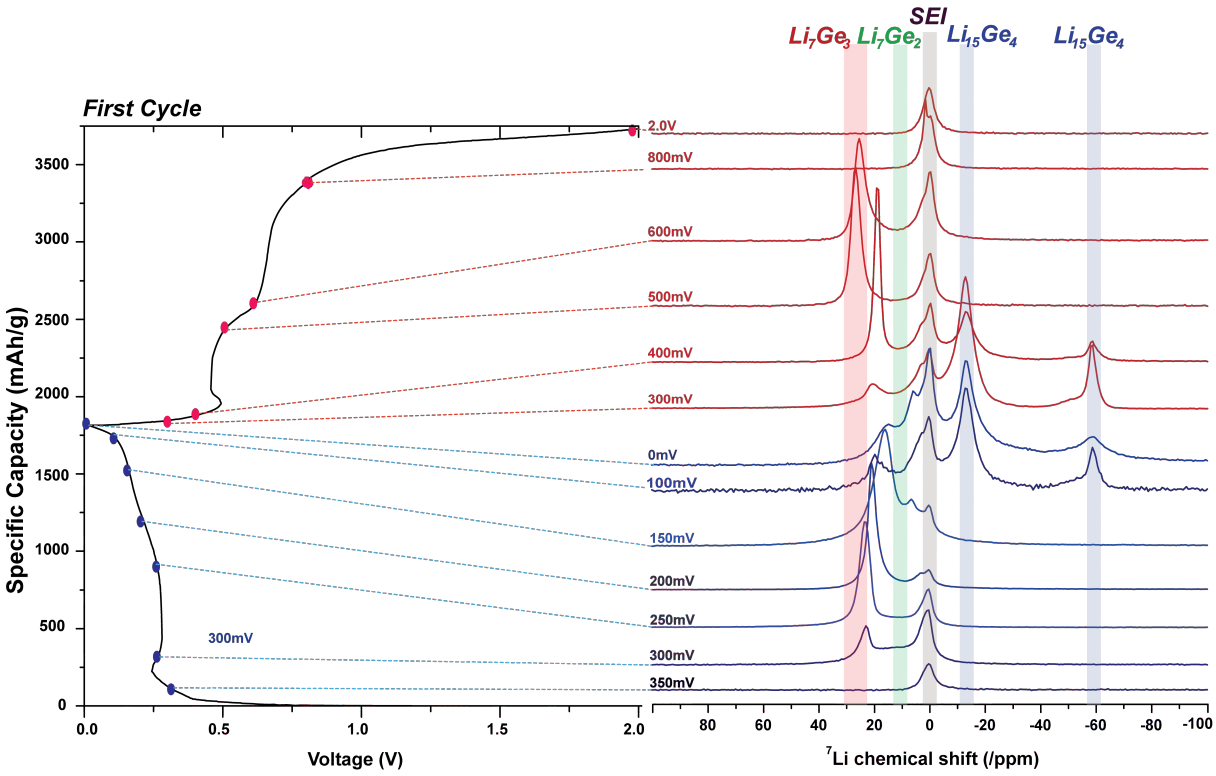

Figure 3.8. *Ex-situ* ^{7}Li NMR spectra of the first (de) lithiation of 100 mesh Ge electrodes at a rate of C/50. The corresponding states of charge for the selected NMR spectra are indicated on the electrochemical profiles. Relevant peak assignments are shown.

The formation of solid-electrolyte-interphase (SEI) is observed as a steep drop in voltage region at 350mV, and is characterized by resonances at around ~0 ppm, due to the decomposition of electrolyte solvents (EC and DMC) on carbon and Ge anode surfaces.[2,27] A small resonance at ~ 22 ppm appears at 300mV, an indication of the

presence of the Li_7Ge_3 phase. A broader component under the 22 ppm resonance also exists and is tentatively ascribed to the formation of more disordered lithiated-Ge phases. The XRD also shows dominant reflections from crystalline Ge phase and minor reflections from Li_7Ge_3 and PDF refinements also suggest the presence of Li_7Ge_3 phase (0.25 fraction). At 250mV, the Li_7Ge_3 resonance dominates the spectrum and grows further, consistent with XRD and PDF results. On the basis of XRD, PDF and NMR results, the first flatter region (300~200mV) and a sharp peak (260mV) in the dQ/dV plot can be ascribed to the formation of Li_7Ge_3 from crystalline Ge phase. Between 200 and 150mV, the resonances shift to a lower chemical shift and also broaden significantly, suggesting a distribution of Li local environments, consistent with the disordered reflections observed in the XRD and the mixture phases (Ge-Ge dumbbells and isolated Ge atoms) observed in the PDF. This second flatter region (between 200 and 100mV) was ascribed to the formation of Li_7Ge_2 via a series of disordered phases (in Chapter 2), but we could not clearly observe the characteristic resonance (10 ppm) of Li_7Ge_2 at 150mV, compared with the synthesized micron-sized Ge, probably because lithiation reactions are slower than the synthesized Ge due to particle size effects. The PDF refinements also support the absence of Li_7Ge_2 phase. At 100 mV, two major resonances are observed at -13 and -58 ppm, characteristic of $Li_{15}Ge_4$ and a minor resonance at around 20 ppm is also observed, suggesting phases containing similar ^7Li local environment as that in Li_7Ge_3 (dumbbell type Ge-Ge bonds), consistent with the PDF analysis. These two main resonances (-13 and -58ppm) remain until the end of discharge and a minor resonance shifts to a lower frequency, indicating the more breakage of Ge-Ge bonds occurs upon further lithiation. No resonance at -20 ppm assigned to the overlithiated Ge phase is detected. The lithiation mechanism of 100 mesh Ge and the synthesized Ge are very similar, except the resonance (-22ppm) from overlithiated Ge phase ($Li_{15+\delta}Ge_4$).

On charge, a steep rise in voltage is observed in the electrochemistry between 0 and 400mV. Consistent with XRD and PDF results, intensities of crystalline $Li_{15}Ge_4$ resonances (-13 and -58ppm) decrease and disappear at ~400mV indicating that $Li_{15}Ge_4$ is broken down on this first steep section of the electrochemistry. The dominant resonance at around 20 ppm appears at 400mV, indicating the formation of Ge-Ge

dumbbell structures from all isolated Ge found in $Li_{15}Ge_4$. The resonance seen at 400mV appears at a lower frequency, compared with the characteristic resonance of Li_7Ge_3 at 23~25 ppm, is accompanied by the reflections from Li_7Ge_3 in XRD, suggesting the formation of Li_7Ge_3-like short-to-long range environments such as Li_8Ge_3 or $Li_{13}Ge_5$. However, the PDF refinements show the best fit is obtained when the Li_7Ge_3 phase is used. At 500mV, this resonance shifts to about 22 ppm, a characteristic shift of the Li_7Ge_3 phase and the signals from $Li_{15}Ge_4$ completely disappear. On the basis of the electrochemistry, XRD, PDF and NMR results, we tentatively attribute a two-phase reaction at around 450mV to the phase transformation from crystalline $Li_{15}Ge_4$ to Li_7Ge_3. The peak at 22 ppm has broadened at 600mV and disappears at 800mV, suggesting the phase transformation from Li_7Ge_3 to amorphous Ge phase at the second plateau (500~700mV), consistent with XRD and PDF results.

In the second cycle, a very broad resonance centered around 19ppm starts to appear at 300mV. During this region, no reflections are observed in XRD and the broad ^{7}Li resonance indicates that the lithium in this phase is extremely disordered. The broad peak at 4 Å from amorphous Ge shifts to a larger r-value in the PDF. Hence, this broad resonance is tentatively ascribed to the formation of disordered lithiated Li_xGe phases in an amorphous Ge matrix or the formation of small domains of Li_7Ge_3. A sharp resonance at 20 ppm appears, which broadens between 250 and 200mV, and can be assigned a Li_7Ge_3-like phase. This phase transformation occurs at a more positive (higher) potential compared to the first cycle, indicating a faster lithiation. By analogy with Si[17], a lower overpotential for Si-Si bond breakage in amorphous Si was observed in the subsequent cycle. A recent TXM study[9] also observed the fracturing during lithiation and the formation of porous structure during lithium extraction result in agglomerates of smaller particles from a large particle. This will reduce the kinetic barriers and speed up the (de) lithiation kinetics.[7,18] Upon discharging to 150mV, the resonance at 10 ppm clearly appears, a characteristic resonance of Li_7Ge_2 and only minor reflections from Li_7Ge_3 in XRD was observed. This supports the reproducible formation of an additional Li_7Ge_2-like phase via transformation from Li_7Ge_3. At 100mV, three major peaks are observed at 10, -13 and -58ppm and can be assigned to Li_7Ge_2 (10ppm) and $Li_{15}Ge_4$ (-13 and -58ppm), while XRD patterns show the only crystalline $Li_{15}Ge_4$ phase and PDF

refinements suggest the presence of minor Li_7Ge_3 and major $Li_{15}Ge_4$ phase. The NMR and PDF results show a discrepancy of phase assignment for peak at the 10ppm. The same batch of *ex-situ* sample was used for NMR and PDF analysis, but the PDF measurement occurred a month afterwards. A recent *in-situ* NMR study[7] reported that Li_7Ge_2 and overlithiated $Li_{15}Ge_4$ phases are electrically driven, metastable phases. When the external electrical contact was removed, these two phases immediately disappeared and were converted to Ge-Ge dumbbells structures. During the time lag, metastable phases might be decomposed and converted to the thermodynamically stable phase. Beyond 100mV, the characteristic resonances of $Li_{15}Ge_4$ are present until the end of discharge to 0V. The resonance at around -22ppm was not observed at 0V and this will be further discussed in the following sections.

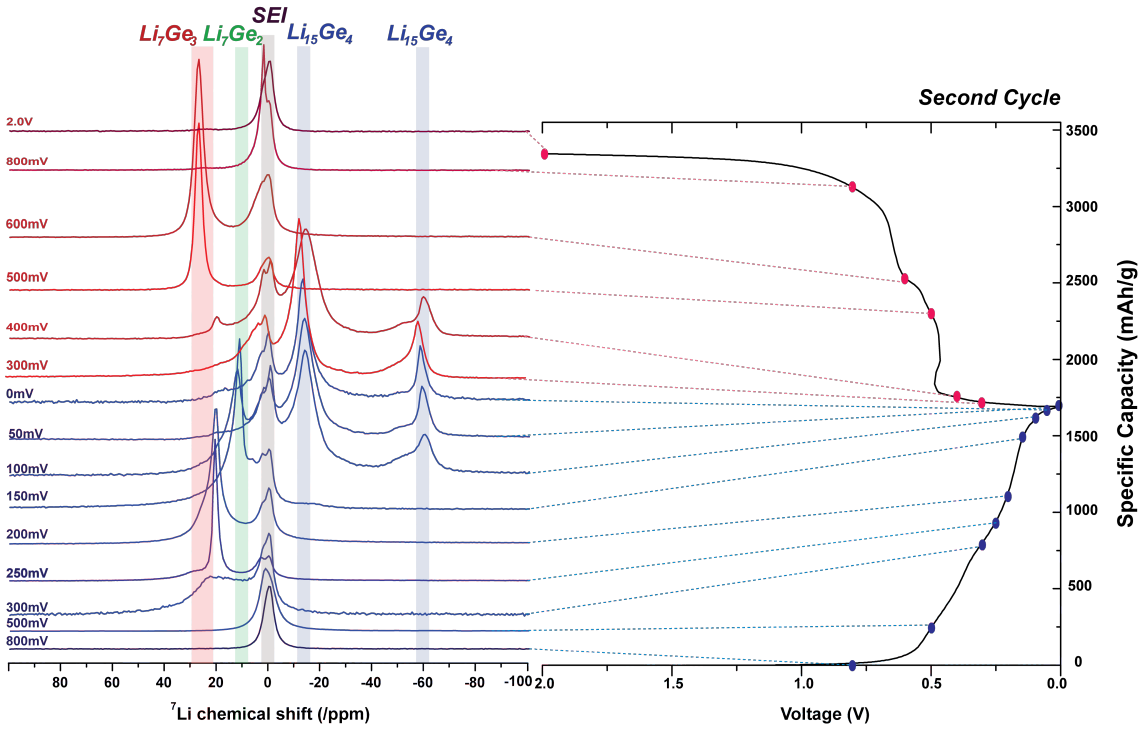

Figure 3.9. *Ex-situ* ^{7}Li NMR spectra of the second (de) lithiation of 100 mesh Ge electrodes at a rate of C/50. The corresponding states of charge for the selected NMR spectra are indicated on the electrochemical profiles. Relevant peak assignments are shown.

On the second charge, the phase transformations appear to be similar to the first charging process, crystalline $Li_{15}Ge_4 \rightarrow Li_7Ge_3 \rightarrow$ amorphous Ge, each resonance being clearer and narrower in the second cycle.

3.3.6. *In-situ* ^{7}Li NMR

In situ ^{7}Li NMR was carried out to understand the detailed local structural evolution in real-time. Here, we note that poor electrochemistry was observed beyond 470 mV upon the first charge which we ascribe to the loss of electrical contacts between Ge particles and the current collector.[9] The spectra (Figure 3.10) all show an intense peak at around 0 ppm, from the free electrolyte in the bag cell battery and SEI on the surface of the electrode. No other well-defined signal is observed at voltages above 175 mV. A broad component with a shift of ~23 ppm, assigned to Li_7Ge_3, starts to appear below 175 mV. This resonance progressively grows in intensity and sharpens until 100 mV. Below 100 mV, the 23ppm resonance continuously shifts to around 10 ppm, the shift observed in the model compound Li_7Ge_2. The continuous shift suggests a continuous structural transformation from Li_7Ge_3 to Li_7Ge_2 between 100 and 20 mV. At the end of discharge, a weak and broad resonance at -22ppm appears at 0 mV, accompanied by an intense resonance from Li_7Ge_2 indicating that full conversion to $Li_{15}Ge_4$ is not achieved.

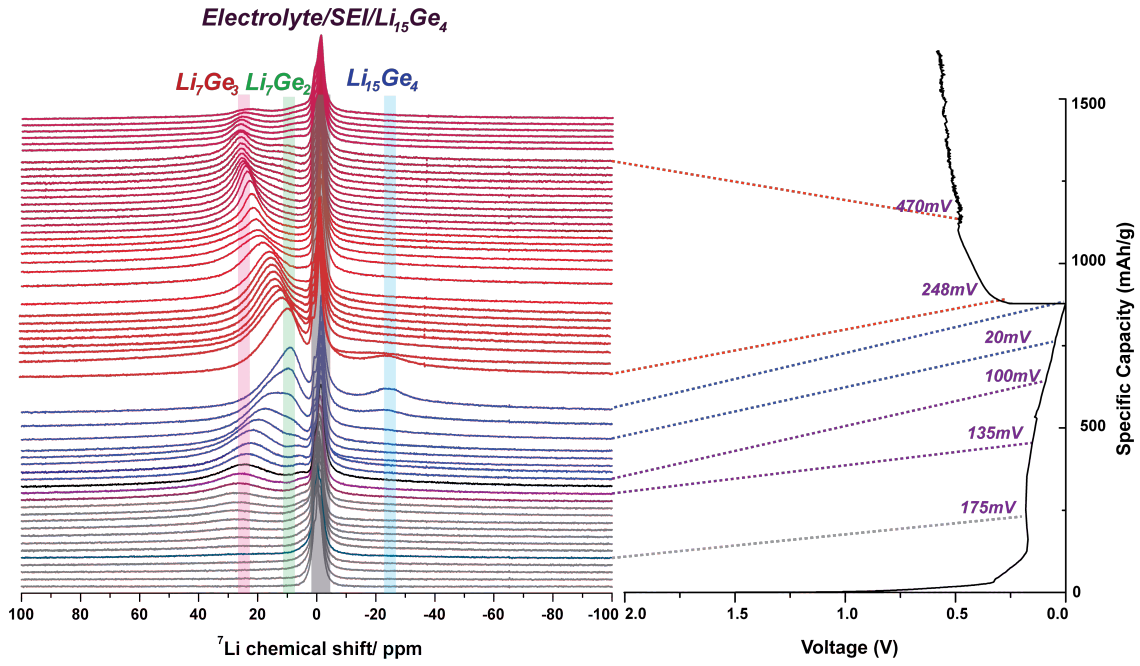

Figure 3.10. *In situ* ^{7}Li NMR spectra of a Ge/Li plastic battery cycled at a rate of C/50. The corresponding state of charge for each spectrum is indicated on the electrochemical profile. Possible assignments to specific chemical phases are indicated.

In contrast to the *ex-situ* NMR, PDF and XRD results, we did not observe a complete phase transformation of Li_7Ge_2 to the $Li_{15}Ge_4$ phase at 0mV, probably because of the difficulty of breaking up all of the Ge-Ge bonds to form fully isolated Ge ions, in the high-resistance bag cell anode design. Furthermore, the distinct existence of the Li_7Ge_2 phase during discharging is only observed in the *in-situ* NMR data. A recent *in-situ* ^{7}Li NMR study[7] also suggested that the peak at -24ppm (assigned to the over-lithiated $Li_{15+\theta}Ge_4$) and the peak at 13ppm (assigned to the amorphous Li_7Ge_2) are electrochemically driven metastable phases. Both phases vanished immediately after the external electrical contact was removed.

On charge, the resonance at -22ppm disappears completely by 250mV (end of the initial steep rise), while the resonance at 10ppm continuously shifts back to 23ppm, indicating the conversion of Li_7Ge_2 to Li_7Ge_3 via a solid-solution type mechanism; this corresponds to the first flatter region in the electrochemical curve. Good reversibility in the charge/discharge cycle was observed via ^{7}Li *in-situ* NMR.

In addition, an apparent discrepancy between the results obtained from *ex-situ* and *in-situ* NMR is observed for the $Li_{15}Ge_4$ phase, at low voltages. The resonance at -22 ppm was only seen in the *in-situ* NMR spectra, while the double resonances at -13 and -58ppm were observed for $Li_{15}Ge_4$ phase in the *ex-situ* NMR spectra. Tang *et al* [7]also observed the resonance at -22 ppm at the end of discharge and assigned this to the over-lithiated phase $Li_{15+\theta}Ge_4$ ($0<\theta<1$) on the basis on their *in-situ* ^{7}Li NMR. This assignment is analogous to our previous study.[22]

$Li_{15}Ge_4$ (space group, $I\bar{4}3d$) has 1 Ge and 2 Li crystallographic sites (Li2; 48e and Li1; 12a), containing all isolated Ge atoms in Li matrix. Figure 3.13 shows the deconvolution results for the fully lithiated Ge in the 2nd cycle. Their integral ratio is well matched with the number of crystallographic site for Li in $Li_{15}Ge_4$ phase. This suggests that the resonances at -13 and -58ppm correspond to the two crystallographic sites for Li in $Li_{15}Ge_4$ phase. (Two-dimensional (2D) ^{7}Li exchange NMR presented in the previous chapter suggested that -13 and -58ppm resonances are in close proximity on the nano-scale).

$Li_{15}Ge_4$	integration %	Crystallographic site
-13ppm	80%	Li2(48e)
-58ppm	20%	Li1(12a)

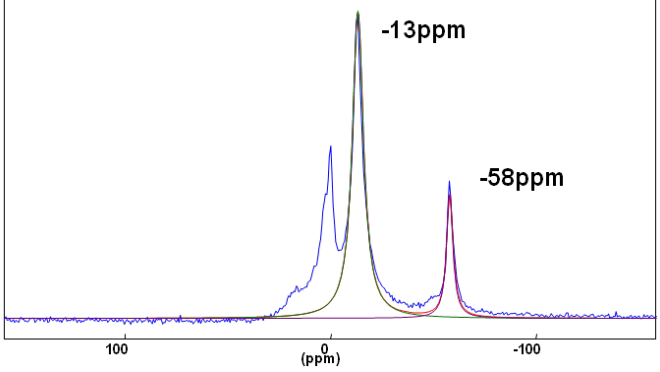

Figure 3.11. Deconvolution results of the 2nd discharge at 0V, showing the peak position (ppm) and integral (%).

Of note, these two resonances are also observed when the model compound $Li_{15}Ge_4$ was aged for 2 weeks (Chapter 2), along with a resonance from Li_7Ge_2. The aged ball-milled $Li_{15}Ge_4$ and *ex-situ* samples must have relaxed sufficiently so that the Li ions occupy the thermodynamically stable sites and form the more ordered phases. In chapter 2, the resonance at -22ppm was detected in *ex-situ/in-situ* NMR and assigned to overlithiated phase $Li_{15+\delta}Ge_4$ based on the increased unit cell parameters at 0mV. This resonance (-22ppm) is only monitored in *in-situ* NMR in 100mesh Ge system and a recent *in-situ* NMR study[7] suggested this resonance was an electrochemically driven meta-stable phase. However, given that this resonance corresponds to the average of the -13 and -58 ppm resonances, weighted by their relative intensities, was now ascribe this to Li ions undergoing rapid exchange between the Li 1 and Li2 sites. Both sites (Li1 and Li2) are close enough that a fast hopping of lithium ion between the crystallographic sites can occur. This motional average process can be tentatively ascribed to kinetically driven more disordered phase. Further VT (variable-temperature) NMR experiments are required to provide more detailed information on the structure and dynamics in this system.

3.3.7. Discussion of the (de) lithiation mechanism

This chapter presents *ex situ* XRD, PDF and *in/ex situ* NMR analyses of (de) lithiation pathways in 100 mesh Ge in the first and second cycles. By correlating *ex situ* XRD, PDF, *in/ex situ* NMR and electrochemical results, we can propose a (de) lithiation pathway (the first and second cycle) of 100 mesh Ge.

Table 3.4. Summary of structural phase transformation of 100 mesh Ge

Lithiation			**Delithiation**		
Voltage	1st Cycle	2nd Cycle	Voltage	1st Cycle	2nd Cycle
2V~300mV	c-Ge/SEI	a-Ge	2V~650mV	a-Ge	a-Ge
300~200mV	c-Ge/Li_7Ge_3	a-Ge/Li_7Ge_3	450~650mV	a-Ge/Li_7Ge_3	a-Ge/Li_7Ge_3
200~100mV	a- Li_7Ge_2	a- Li_7Ge_2	0~450mV	a- Li_7Ge_2	a- Li_7Ge_2
100~0mV	c-$Li_{15}Ge_4$	c-$Li_{15}Ge_4$		c-$Li_{15}Ge_4$	c-$Li_{15}Ge_4$

The first cycle,

On discharge: c-Ge → Li_7Ge_3 → a-Li_7Ge_2 → c- $Li_{15}Ge_4$

On charge: a-Ge ← Li_7Ge_3 ($Li_{13}Ge_5$, Li_8Ge_3) ← a-Li_7Ge_2 ← c-$Li_{15}Ge_4$

The second cycle,

On discharge: a-Ge → a- Li_7Ge_3 + a-Ge??? → Li_7Ge_3 → a-Li_7Ge_2 → c- $Li_{15}Ge_4$

On charge: a-Ge ← Li_7Ge_3 ($Li_{13}Ge_5$, Li_8Ge_3) ← a-Li_7Ge_2 ← c-$Li_{15}Ge_4$

During the first discharge, similar lithiation processes of the previous chapter for 100 mesh Ge occur at lower potential ranges due to larger particle sizes. Between 300 and 200mV, a sharp peak at 260mV (a flatter region in electrochemical profile) is observed in dQ/dV plot, suggesting a two-phase reaction. A conversion reaction from c-Ge to Li_7Ge_3 phases is observed in this voltage region, supported by XRD, PDF and NMR results. A gradual sloping voltage region (200~100mV) is followed in the electrochemistry. In this region, both the XRD and PDF results show considerable disorder. PDF refinements suggest a mixture of Ge-Ge dumbbells and isolated Ge phases (Li_7Ge_3 and Li_8Ge_3 or $Li_{13}Ge_5$), indicating the gradual Ge-Ge bond breakage. Broad ^{7}Li

resonances and the continuous shifting of the resonances are observed in *ex-situ* NMR and *in-situ* NMR, respectively. On the basis of the previous study of synthesized Ge, the lithiation process at this voltage region proceeds via a heterogeneous pathway from Li_7Ge_3 to Li_7Ge_2. Dumbbell type Ge-Ge bonds are gradually broken ($Li_7Ge_3 \rightarrow Li_{13}Ge_5 \rightarrow Li_8Ge_3$) and eventually, Li_7Ge_2-like environments are formed. However, in contrast to the previous study, there is no obvious evidence for formation of Li_7Ge_2 in the *ex-situ* XRD, PDF and ^{7}Li NMR. Only *in-situ* NMR detected the distinctive existence of Li_7Ge_2 phase. This apparent discrepancy is possibly due to the limitation of the results obtained from *ex-situ* studies.[6] The Li_7Ge_2 phase is known to be a electrochemically driven and metastable phase,[7] so *ex-situ* samples were sufficiently relaxed to convert the thermodynamic stable phases such as $Li_{13}Ge_5$ or Li_8Ge_3.

A rapid drop in voltage between 100 and 0mV is observed in the electrochemical cell. The sharp reflections and long-range correlations from $Li_{15}Ge_4$ in XRD and PDF patterns indicated the formation of crystalline $Li_{15}Ge_4$ phase from the metastable Li_7Ge_2 phase in this region. The ^{7}Li resonances difference between *ex-situ* and *in-situ* NMR results of $Li_{15}Ge_4$ phase is also possibly due to phase stability.

On charge, an apparent voltage curve hysteresis is observed[23] and this voltage difference is ascribed to the different lithiation pathway taken on charge and discharge.[18] Crystalline $Li_{15}Ge_4$ is converted to Li_7Ge_3 phase at the first flatter region as evidenced by the PDF peaks found at distances corresponding to Ge-Ge dumbbell and further alignment distanced at 4.3 and 5.1 Å. This is followed by the phase transformation of Li_7Ge_3 to amorphous Ge at the second flatter region. A noticeable difference between *ex-situ* and *in-situ* studies is found with the existence of Li_7Ge_2 in the *in situ* NMR study. In prior DFT calculations,[26] Li_7Ge_2 lies above the convex hull (*i.e.* it is a metastable phase), therefore, its formation is kinetically driven upon lithiation. In addition, a recent *in-situ* ^{7}Li NMR study[7] shows that Li_7Ge_2, at 13 ppm, and over-lithiated $Li_{15+\delta}Ge_4$, at -24 ppm, are electrochemically driven and metastable. If delithiation follows the thermodynamic pathway, delithiation of crystalline $Li_{15}Ge_4$ may lead to form the thermodynamically stable phases directly, $Li_{13}Ge_5$, Li_8Ge_3, Li_7Ge_3, locally resemble structures with all containing Ge-Ge dumbbells and isolated Ge atoms. However, the *in-situ* NMR results show the transformation from $Li_{15}Ge_4$ to Li_7Ge_2 and then, the continuous shifting from

Li_7Ge_2 (10 ppm) to Li_7Ge_3 (23ppm), so these discrepancies are also possible artifacts from *ex-situ* studies. *In-situ* ^{7}Li NMR results presented here, and the recent study by Tang *et al*[7], indicated that (de) lithiation pathways are reversible.

In the second cycle, the amorphous Ge matix has a more open porous structure caused by lithium extraction and fracturing on the basis of the recent TXM study[9]; therefore, it helps to speed up the reaction kinetics of lithiation, by analogy with crystalline Si.[17,18] (De) lithiation pathways show consistency with the first cycle, except the lithiation occurs at a higher potential indicating faster kinetics, attributed to the porous and smaller particles. The formation of disordered Li environments occurs initially, and then Li_7Ge_3 phase is observed, indicated by *ex-situ* NMR and PDF.

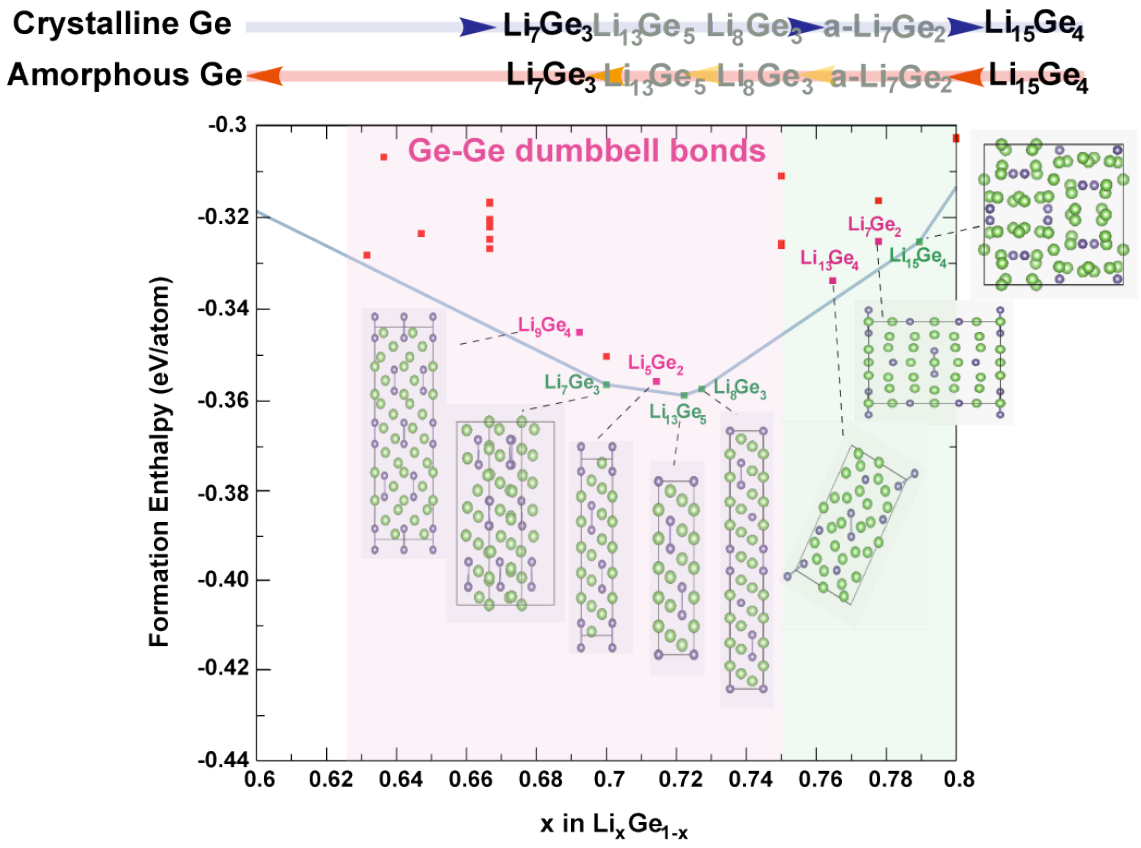

Figure 3.12. The (de) lithiation pathway showing the common structural features of possible lithiated Ge phases: The red shadows are all possible (de) lithiated phases containing parallel-aligned Ge-Ge dumbbells in columns. The blue line is the tie-line indicating the stable phases at 0K predicted by DFT calculation.[26] The green squares correspond to the thermodynamic phase.

3.4. Conclusions

The (de) lithiation mechanisms of 100 mesh Ge anodes have been studied with *ex situ* XRD, PDF and *in/ex situ* high-resolution ^{7}Li solid-state NMR spectroscopy. The lithiation of 100 mesh Ge anodes involves the formation of Li_7Ge_3 initially through a two-phase reaction process, followed by conversion to Li_7Ge_2 via a series of highly disordered phases. Finally, the formation of crystalline $Li_{15}Ge_4$ occurs below 100mV. On charge, crystalline $Li_{15}Ge_4$ delithiates and starts to form the thermodynamically stable Ge-Ge dumbbell phases (Li_7Ge_3-like short to long range environments are confirmed by *ex-situ* XRD, PDF and NMR analyses) and, eventually, forms amorphous Ge. The subsequent cycle follows a similar (de) lithiation pathway to the first cycle.

3.5. References

(1) Yoon, S.; Park, C.-M.; Sohn, H.-J. *Electrochem. Solid-State Lett.* **2008**, *11*, A42.

(2) Graetz, J.; Ahn, C. C.; Yazami, R.; Fultz, B. *J. Electrochem.Soc.* **2004**, *151*, A698.

(3) Baggetto, L. c.; Notten, P. H. L. *J. Electrochem. Soc.* **2009**, *156*, A169.

(4) Chan, C. K.; Zhang, X. F.; Cui, Y. *Nano Lett.* **2008**, *8*, 307.

(5) Liu, X. H.; Liu, Y.; Kushima, A.; Zhang, S.; Zhu, T.; Li, J.; Huang, J. Y. *Adv.Energy Mater.* **2012**, *2*, 722.

(6) Lim, L. Y.; Liu, N.; Cui, Y.; Toney, M. F. *Chem. Mater.* **2014**, *26*, 3739−3746.

(7) Tang, W.; Liu, Y.; Peng, C.; Hu, M. Y.; Deng, X.; Lin, M.; Hu, J. Z.; Loh, K. P. *J. Am.Chem. Soc.* **2015**, *137*, 2600.

(8) Park, C. M.; Kim, J. H.; Kim, H.; Sohn, H. J. *Chem. Soc. Rev.* **2010**, *39*, 3115.

(9) Weker, J. N.; Liu, N.; Misra, S.; Andrews, J. C.; Cui, Y.; Toney, M. F. *Energy Environ. Sci.* **2014**, *7*, 2771.

(10) Bridel, J. S.; Azaïs, T.; Morcrette, M.; Tarascon, J. M.; Larcher, D. *Chem. Mater.* **2009**, *22*, 1229.

(11) Guy, D.; Lestriez, B.; Guyomard, D. *Adv. Mater.* **2004**, *16*, 553.

(12) Magasinski, A.; Zdyrko, B.; Kovalenko, I.; Hertzberg, B.; Burtovyy, R.; Huebner, C. F.; Fuller, T. F.; Luzinov, I.; Yushin, G. *ACS Appl. Mater. Interfaces* **2010**, *2*, 3004.

(13) Hochgatterer, N. S.; Schweiger, M. R.; Koller, S.; Raimann, P. R.; Wöhrle, T.; Wurm, C.; Winter, M. *Electrochem. Solid-State Lett.* **2008**, *11*, A76.

(14) Erk, C.; Brezesinski, T.; Sommer, H.; Schneider, R.; Janek, J. *ACS Appl. Mater. Interfaces* **2013**, *5*, 7299.

(15) Koo, B.; Kim, H.; Cho, Y.; Lee, K. T.; Choi, N.-S.; Cho, J. *Angew. Chem. Int. Ed.* **2012**, *51*, 8762.

(16) Key, B.; Bhattacharyya, R.; Morcrette, M.; Seznéc, V.; Tarascon, J.-M.; Grey, C. P. *J. Am. Chem. Soc.* **2009**, *131*, 9239.

(17) Key, B.; Morcrette, M.; Tarascon, J.-M.; Grey, C. P. *J. Am. Chem. Soc.* **2010**, *133*, 503.

(18) Ogata, K.; Salager, E.; Kerr, C. J.; Fraser, A. E.; Ducati, C.; Morris, A. J.; Hofmann, S.; Grey, C. P. *Nat. Commun.* **2014**, *5*, 3217.

(19) Hammersley, A. P.; Svensson, S. O.; Hanfland, M.; Fitch, A. N.; Hausermann, D. *High Pressure Research* **1996**, *14*, 235.

(20) Qiu, X.; Thompson, J. W.; Billinge, S. J. L. *J. Appl. Crystallogr* **2004**, *37*, 678.

(21) Farrow, C. L.; Juhás, P.; Liu, J. W.; Bryndin, D.; Božin, E. S.; Bloch, J.; Proffen, T.; Billinge, S. J. L. *J. Phys.: Condens. Matter* **2007**, *19*, 335219.

(22) Jung, H.; Allan, P. K.; Hu, Y.-Y.; Borkiewicz, O. J.; Wang, X.-L.; Han, W.-Q.; Du, L.-S.; Pickard, C. J.; Chupas, P. J.; Chapman, K. W.; Morris, A. J.; Grey, C. P. *Chem. Mater.* **2015**, *27*, 1031.

(23) Zhang, W.-J. *J. Power Sources* **2011**, *196*, 877.
(24) Jia, H.; Kloepsch, R.; He, X.; Badillo, J. P.; Gao, P.; Fromm, O.; Placke, T.; Winter, M. *Chem.Mater.* **2014**, *26*, 5683.
(25) Walters, J. K.; Newport, R. J. *Phys. Rev. B: Condens. Matter Mater. Phys.* **1996**, *53*.
(26) Morris, A. J.; Grey, C. P.; Pickard, C. J. *Phys. Rev. B: Condens. Matter* **2014**, *90*, 054111.
(27) Chan, C. K.; Zhang, X. F.; Cui, Y. *Nano Lett.* **2007**, *8*, 307.

Chapter 4

Chemical Phase Evolution of nano-sized Ge anodes in Lithium-Ion Batteries

4.1. Introduction

Silicon, germanium, and tin are attractive anode materials for LIBs due to their high energy densities and safety characteristics.[1] They undergo alloying processes with Li and exhibit much higher theoretical capacities, (silicon (4200 mAh/g), germanium (1623 mAh/g), and tin (993 mAh/g), compared with graphite (375 mAh/g)). Moreover, they mitigate safety issues associated with using Li metal as anodes.[2]

Recently, germanium has been considered as a promising anode material for next-generation lithium ion batteries due to its high capacity, fast lithium diffusion[3], and high electronic conductivity.[4] These properties lead to much better rate performance of Ge anodes than that of Si anodes used in LIBs.[5] However, the practical application of germanium is hindered by a severe volume changes during lithium insertion and extraction. A recent in situ TXM study showed that this gives rise to a structural disintegration, pulverization, loss of electrical conductivity and consequently a rapid capacity fading upon cycling.[6]

Several approaches have been reported to improve capacity retention. Morphologies of germanium have been modified to have better structural stability, such as nano-particles[7,8], nano-wires[9-11], nano-tube[12,13] and macroporous[14]/mesoporous[15]/porous[16] structures. Furthermore, germanium based composites (tin-germanium nano-composites[17,18], germanium/carbon composites[12,19,20]) and nano-sized germanium oxides[21] are also promising candidates for improving capacity retention.

Decreasing the Ge particle size to the nano-scale can reduce the stress/strain generated during lithiation/delithiation, suppressing the fracture, and facilitating diffusion of the Li ions, leading to high rate capability. However, larger surface area will lead to the formation of excessive SEI, resulting in irreversible capacity loss. Moreover, certain nanometer range Ge particles aggregate each other during cycling and show significant capacity fading.[22] To overcome these nano-size related issues, various Ge/C composites materials[23-26] have been synthesized. Seng. *et al*[27] reported a facile synthesis method to produce Ge/C nanostructures by carbon coating, prohibiting particle aggregation and improving a conductivity, good capacity retention was seen over 50 cycles and along with an exceptionally high rate capability. The author suggested that the lithiation pathway is similar to those seen in previous studies.[28]

In the previous chapters, we reported the electrochemical lithiation/delithiation mechanism of micro-sized crystalline G anodes; synthesized (chapter 2) and 100 mesh commercial Ge (chapter 3). The electrochemical lithiation mechanism of nano-sized Ge remains unclear due to the formation of amorphous phases during cycling and the detection limit of analytical tools. The aim of this chapter is to elucidate the structural transformation of nano-sized Ge/C sample, provided by Park *et al*,[19] during lithiation and delithiation. *Ex-situ* ^{7}Li MAS NMR and *in-situ* PDF analysis were used to probe the local structural variations. By correlating *ex-situ* ^{7}Li NMR data and *in-situ* PDF analysis during electrochemical cycling, we are able to track the lithiated germanium phases and structural changes of Ge upon cycling.

4.2. Experimental section

4.2.1. Synthesis of carbon coated nano-sized Germanium

Pristine material (nano-sized Ge) was provided by M-H. Park.[19] Carbon coated nano-sized germanium powders were prepared by a 3-step procedure. GeO_2 nanoparticles were first prepared via hydrolysis of $GeCl_4$[29]. Subsequently, the carbon coating process was carried out under 10% acetylene gas in Argon at 620 °C for 1 hr, followed by reduction under hydrogen gas at 620 °C for 6 hr to obtain carbon-coated nano-sized germanium.[30] This sample will be refered to an n-Ge in the subsequent text.

The hydrolysis of $GeCl_4$ was carried out as described in the following: 2 ml $GeCl_4$ (99.99%, Alfa Aesar) was added to 8 ml anhydrous ethanol (99.9%, Sigma Aldrich) and stirred for 10 minutes. In a separate beaker, 10 ml de-ionized water was added to 100 ml anhydrous ethanol and left to stir for 10 minutes. The $GeCl_4$ mixture was dropped into the water/ethanol solution. This mixture was stirred continuously for 3 hours. The resulting powder was collected by centrifugation, washed several times with ethanol and dried at 100°C to obtain the final product GeO_2.

4.2.2. Electrochemistry

Electrochemically-cycled electrode samples for *ex-situ* experiments (NMR) were prepared using CR 2032 –type coin cells. The positive electrodes were formulated from 60% germanium powder as the active material, 20% Super P (Timcal) as a conducting matrix, and 20% polyvinylidene fluoride (PVDF, Kynar Flex 2801-00) as a binder. The mixture was suspended in N-methyl pyrrolidinone (NMP, 99+% Sigma-Aldrich) to form a slurry; the slurry was then coated on a Cu foil, dried at 100°C for 10 minutes in a convection oven (Grieve co.) and then at 60°C for 24 hours in a vacuum oven (Thermo scientific). Coin cells were assembled in an Ar-filled glove box using Li metal foil as the negative electrode. 1M $LiPF_6$ in a 1:1 volumetric mixture of ethylene carbonate (EC) and dimethyl carbonate (DMC) was used as the electrolyte and a porous glass fiber (GF/B, Whatman) as the separator. The cells were cycled using an Arbin instruments battery cycler with a cycling rate of C/15 (corresponding to a discharge to a theoretical capacity of 1623 mAh/g in 15 hours, assuming that $Li_{4.4}Ge$ is the final

electrochemical lithiation product[31]) between 0.0 to 2.0 V at room temperature. After electrochemical cycling, each cell was dissembled and the electrode were washed with dimethyl carbonate (DMC, 99+% Sigma-Alrich) and dried in the Ar-filled glove box.

4.2.3. *In-situ* Pair distribution function analysis

For in situ PDF measurements, electrode pellets of carbon coated n-Ge were prepared. The positive electrodes were formulated from 60% germanium powder, 20% Super P (Timcal), and 20% polyvinylidene fluoride (PVDF, Kynar Flex 2801-00). The mixture was suspended in N-methyl pyrrolidinone (NMP, 99+% Sigma-Aldrich) to form a slurry; the slurry was then coated on a Cu foil, dried at 100°C for 10 minutes in a convection oven (Grieve co.) and then at 60°C for 24 hours in a vacuum oven (Thermo scientific). The dried film was collected as a powder and formed into pellets (10 mm diameter, 120–180 μm thick).

The electrode pellets were assembled into an electrochemical cell suitable for in situ measurements (the "AMPIX" electrochemical cell)[32] with a glass fiber separator (Whatman GF/A), Li metal foil and liquid electrolyte (1 M $LiPF_6$ in 1:1 v:v ethylene carbonate:dimethylcarbonate (EC:DMC) from Tomiyama Pure Chemical Industries) within an Ar atmosphere glovebox. Cells were cycled galvanostatically against lithium at constant current of 0.29 mA/g (C/15) in the range 2.0–0.0 V. X-ray total scattering data suitable for PDF analysis were collected using 5 min exposures at 60 min intervals. Data were collected during the first discharge–charge cycle. The cycling rates and number of discharge–charge cycles used were ultimately limited by the allocated beamtime.

Total scattering data (Bragg diffraction and diffuse scattering data) were collected at the dedicated PDF beamline 11-ID-B at the Advanced Photon Source, Argonne National Laboratory. High-energy X-rays (~58 keV, $\lambda = 0.2128$ Å) were used in combination with a large amorphous-silicon based area detector (Perkin-Elmer) to collect total scattering data to high values of momentum transfer ($Q_{max} \approx 18$ Å)[33,34]. The scattering images were reduced to one-dimensional data using FIT2D[35] using CeO_2 as a calibration standard. The data were corrected for background scattering, Compton scattering and detector effects within pdfgetX2 and Fourier transformed to get $\mathbf{G}(\mathbf{r})$, the PDF.[36] No attempt was made to subtract the carbon and binder signals from the total PDF pattern due to their relatively small contribution to the X-ray scattering. Least-squares refinements of structures against PDF data were performed in

PDFGui[37] in the distance range of 0 – 30 Å. Initial value for Q_{damp} parameter was set to be 0.045, and the atomic displacement parameters were set as $U_{11}=U_{22}=U_{33}$ = 0.005Å^2 (constrained to be equal for all Ge and all Li atoms) and $U_{12}=U_{23}=U_{13}.=0$. Q_{damp} was refined on the initial crystalline germanium sample, and then fixed for futher refinements. Lattice parameters, the linear atomic correlation factor (delta 1), and anisotropic temperature factors (U_{11}, U_{22}, U_{33}) were refined. The fractional coordinates factors (x, y, z) were not refined here. The initial refinements of each PDF pattern assume a single pure phase; however, incorporation of second minor phases has significantly improved the refinement quality, as indicated by reduced refinement quality factors, i.e., the R_w values. Note that R_w-factors for PDF refinements are generally higher than what expected in a Rietveld refinement because the functions, which are being fit, are significantly different and cannot be compared. The residual is, however, useful as a measure of goodness of fit when comparing models fit to PDF data. Residuals of greater than 15% are common even in well-ordered materials.

4.2.4. *Ex situ* ^{7}Li MAS NMR

Ex-situ battery samples were packed in 1.3 mm diameter Zirconia rotors in an Ar-filled glove box. High-resolution ^{7}Li MAS NMR spectra were acquired on a Varian InfinityPlus-500 MHz spectrometer at a magnetic field of 11.7 T, with a 1.3 mm MAS probe at a spinning speed of 50 kHz. Spectra were acquired using a rotor-synchronized spin-echo sequence (90°-τ-180°-τ-acq), where τ-values were set to be equal to one rotor period, i.e., 20 μs. The 90° pulse length was 2.2 μs and the recycle delay 10 s. ^{7}Li spectra were referenced to a 1M ^{7}LiCl solution at 0 ppm. ^{7}Li MAS NMR spectra were normalized for analysis on the basis of the number of acquisitions and sample mass.

4.2. Results

4.3.1. Ge electrochemistry: comparison of different particle sizes

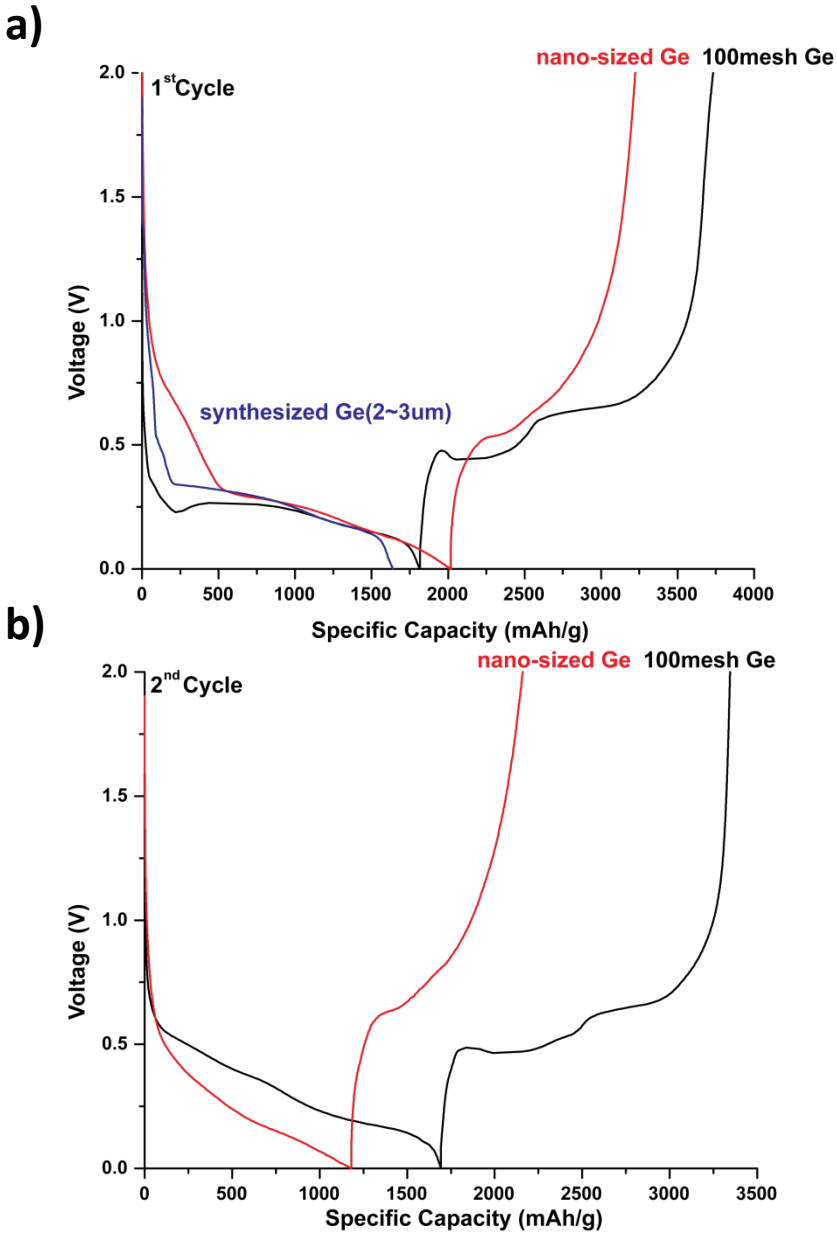

Figure 4. 1. a) The electrochemical profiles for the first cycle (a) and second cycle (b) of synthesized Ge (blue line; 1st discharge only), 100mesh Ge (black line) and n-Ge (red line). (The experiments were peroformed with coin cells)

The electrochemical performance of n-Ge was investigated in the voltage range 2.0-0.0 V versus Li/Li^+ at a rate of C/15. The Figure 4.1 shows a comparison between the voltage profiles of n-Ge and different particle sized Ge, synthesized micrometric (2-3μm), and commercial micrometric 100mesh (<149μm) germanium at a C/50 rate.

The potential of n-Ge drops initially by 750mV and an approximately linear decrease in the voltage is observed at around 750~350mV, contrary to micron-sized germanium (synthesized and 100 mesh germanium), suggesting greater SEI formation due to a larger surface area in the nano-sized particles.[6,38] Flatter region at around 350~250mV is consistent with a lithiation process as observed for micron-sized Ge, and is followed by a sloping potential region at around 250~100 mV. In contrast to micron-sized Ge (synthesized and 100 mesh Ge) where the potential quickly decreases from 200 mV to 0 V, the potential drops progressively to 0V for n-Ge.

Upon delithiation, the voltage profiles show a similar trend to 100 mesh Ge, starting with a steep rise to 540mV. Unlike 100mesh Ge, there is not a distinguishable inflection point at 540mV. Small flatter region around 540 mV to 600 mV, and then the potential rises again until the upper limit used here at 2.0 V.

There is a large irreversible capacity of n-Ge (coulombic efficiency of 65%) compared to micron-sized particles (coulombic efficiency of 94%). This is due to the large surface area of n-Ge, resulting in more lithium being used in the solid electrolyte interphase (SEI) layer, irreversibly formed in the first cycle.[27] The second discharging voltage profile features more gradual processes than the first discharge, resulting from smaller particle size and amorphous Ge matrix. Upon delithiation in the second cycle, a similar voltage trend is observed.

The corresponding dQ/dV profiles of n-Ge are plotted in Figure 4.2. During the first discharging process, a broad peak around 700mV is observed, associated with SEI formation, as well as one sharp peak at 280mV and a broad shoulder at 150mV. These are similar to those found in micron sized Ge (chapter 2), in contrast, no distinguishable third process corresponding the formation of c-$Li_{15}Ge_4$ from amorphous Li_7Ge_2 is observed, unlike in micron-sized germanium where this. As seen in Figure 4.2, the relative peak intensities are much weaker than micron-sized Ge indicating that the smaller particle size of n-Ge may result in differences in the electrochemical mechanism. Thus, further investigation of the electrochemical processes is required.

On the first delithiation, a prominent sharp peak appears at 540mV and this is also accompanied by a lower intensity, broad peak around 600mV. In Si anodes, this sharp delithiation peak corresponded to the delithiation of crystalline $Li_{15}Si_4$ and broader peaks were produced when delithiation proceeded in amorphous Li_xSi phases.[39] Lim *et al*[40], in an *in-situ* X-ray diffraction (XRD) and X-ray absorption spectra (XAS) study of a micron-sized Ge electrode, also reported these two delithiation processes and suggested that the sharp peak at 450mV corresponds to the phase transformation from c-$Li_{15}Ge_4$ to a heterogeneous amorphous Li_xGe phase and that the broad peak at 640mV is due to the formation of an amorphous Ge phase.

There are several differences between the 1st and 2nd (de) lithiations. The broad peak at 700mV disappears, indicating that it is a first cycle irreversible process due to breakdown of electrolyte on the electrode surface. The sharp peak at 280mV no longer appears and is replaced by a broad peak with low intensity centered around 400mV. During Li-extraction process, the two prominent peaks shift to higher potentials.

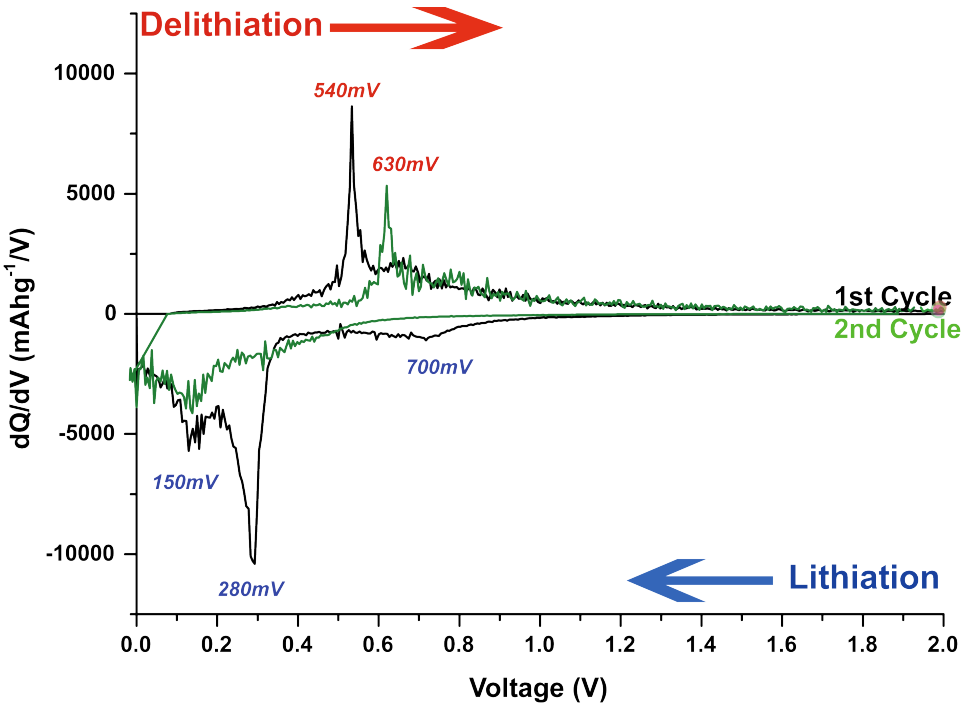

Figure 4. 2 The differential capacity dQ/dV plot for the 1st and 2nd cycle of n-Ge. All the cells were tested in the voltage range of 0.0~2.0V versus Li/Li^+.

4.3.2. *In-situ* Pair Distribution Function (PDF) Analysis and *ex-situ* ^{7}Li NMR studies.

To investigate the phase transformation in n-Ge, *in-situ* PDF analysis and *ex-situ* ^{7}Li NMR are employed. The experimental *in-situ* PDFs for the first discharge/charge and second discharge/charge are shown in Figure 4.3 and 4.10, respectively. (Figure 4.7 and 4.12 show PDF data at an extended distance range.) *Ex-situ* ^{7}Li NMR spectra, obtained at various stages of the first and second cycles, are shown in Figure 4.8 and 4.13, respectively.

The First Cycle

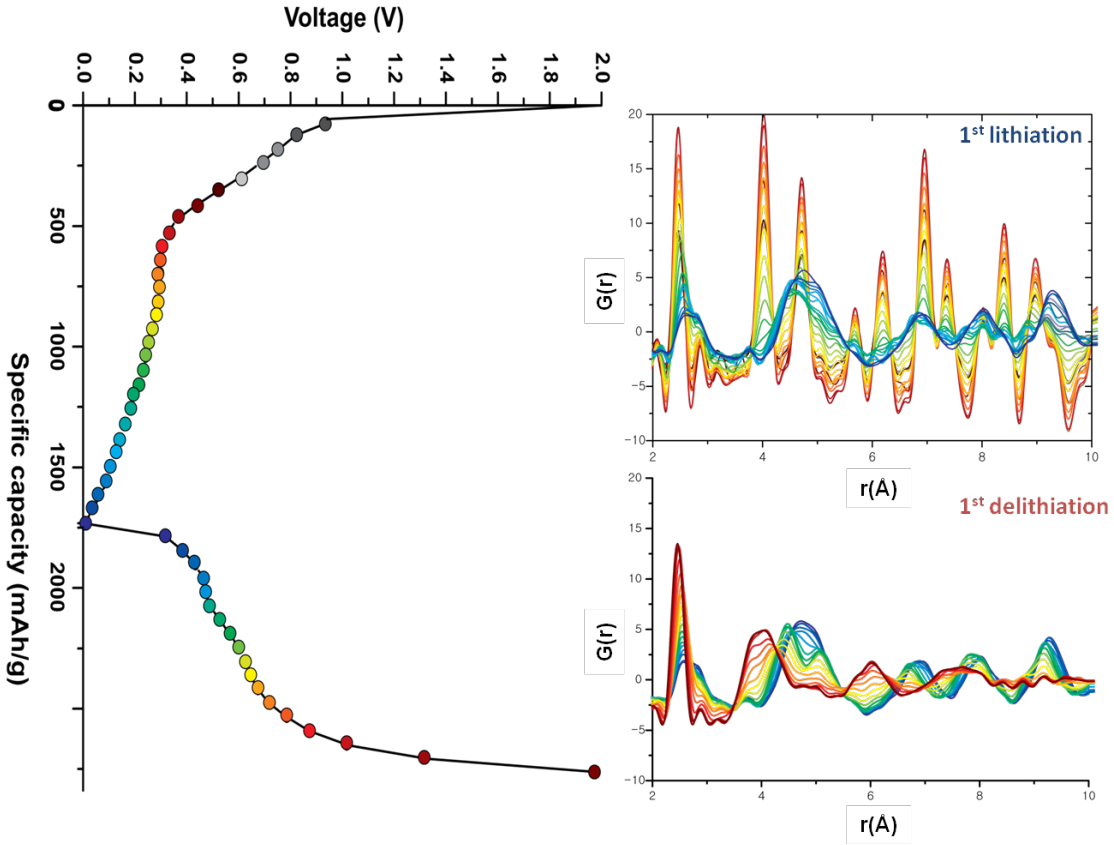

Figure 4.3. *In-situ* PDF patterns for n-Ge of the first (de) lithiation at a rate of C/15. The corresponding electrochemical discharge-charge curves are plotted using the same color-coding. Full PDF patterns are shown in Figure 4.7.

The PDF for the pristine n-Ge shows sharp correlations out to high-r values (>100 Å), indicating the presence of a crystalline n-Ge phase. During lithiation, the r_{max} (the maximum distance at which features are observed in the PDF) reduces to around 40 Å, showing the breakdown of the crystalline phase.(Figure 4.7) At the beginning of the discharge, the PDF patterns are dominated by the pristine Ge phase. The first peak at 2.43 Å corresponds to Ge-Ge bonds and the two other peaks at 3.9 Å, and 4.6 Å are from Ge-Ge next-nearest neighbor correlations. At 366 mV, at the end of the sloping process, there is no significant change to the structure of the electrode. Refinement results are shown in Figure 4.4.

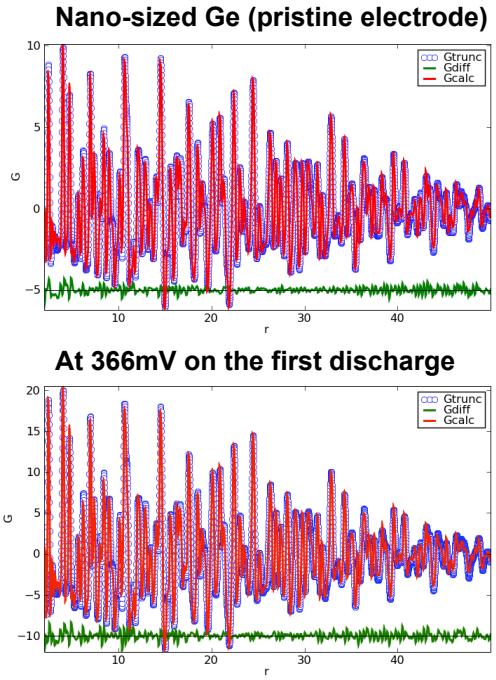

Figure 4.4. PDF refinement patterns of the pristine Ge (R_w=0.0762) and cycled Ge electrodes at 366mV (R_w=0.0947); Representative refined patterns (red) overlapped with experimental patterns (blue). The difference between simulated and experimental PDFs is shown in green (offset by -5 and -10).

Below 250mV, there is a gradual loss of intensity of the peaks in the PDF, indicating that crystalline germanium is broken down. Between 250 and 150 mV, the first Ge-Ge correlation at 2.43 Å gradually decreases and shifts to a larger value. Ge-Ge bond distances increase upon lithiation (from 2.43 Å in Ge to 2.62 Å in Li_7Ge_2) The intensities of two other peaks at 3.9 Å and

4.6 Å gradually decrease and shift to larger values due to the insertion of Li and the breakdown of the Ge-framework.

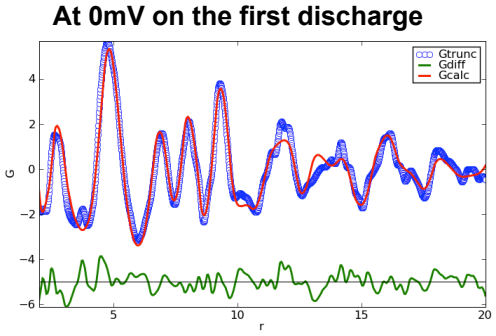

Figure 4.5. PDF refinement patterns of the lithiated n-Ge electrode at 0mV (R_w=0.2363).

Upon further lithiation, the intensity of the Ge-Ge peak decreases and the broad peak at 2.7 Å from Li-Ge correlations is dominant at 0 mV. Two other peaks at 3.9 Å and 4.6 Å merge to a broad peak at 4.7Å, which is characteristic of the closest nonbonded Ge-Ge correlations from Li_7Ge_2 and $Li_{15}Ge_4$. Least-squared refinements at the end of lithiation indicate that the final lithiation product is a mixture of major Li_7Ge_2 (0.80) and minor $Li_{15}Ge_4$ (0.20) phases (Figure 4.5).

Upon delithiation, two distinct changes are observed in the PDF, between 0 mV and 600 mV and 600 mV and the end of delithiation. These can be linked with the processes observed in the electrochemical curve. During the first process, between 500 and 600 mV (a sharp process at 540mV is observed in the dQ/dV plot), the peak at 2.62 Å shifts to a lower value and gradually grows. The broad peak at 4.7 Å splits into two peaks, which represent the characteristic correlations from parallel-aligned Ge-Ge dumbbells along the c-axis in lithiated Ge phases (such as Li_7Ge_3, $Li_{13}Ge_5$, and Li_8Ge_3), indicating the formation of where all the germanium exists as dumbbells. Beyond 600mV, two peaks shift and merge to a broad peak around 4 Å signifying the reformation of extended Ge-networks. At the end of charge, r_{max} significantly reduces to around 12 Å and only three peaks at 2.5, 4 and 6 Å are present, indicating that the crystalline cubic Ge phase is completely absent. Cho *et al*[41], in an e*x-situ* XRD study of amorphous/crystalline GeS_x, reported the formation of the metastable tetragonal Ge phase (ST12) after delithiation and this phase persisted after 100 cycles, suggesting that the tetragonal Ge

phase may be formed on delithiation. However, a poor fit (R_w=0.3044) in this n-Ge system was obtained when a refinement using the tetragonal Ge phase[42] is performed, with the fit of the peaks at 4 and 8 Å being particularly poor. It suggests that the phase formed cycling of n-Ge is not related to tetragonal Ge. (Figure 4.6) The observed peaks are very similar to those distance found in an amorphous Ge synthesized by vapor evaporation[43], which have been studied by neutron PDF[44] and modeled as a disordered tetrahedral network.

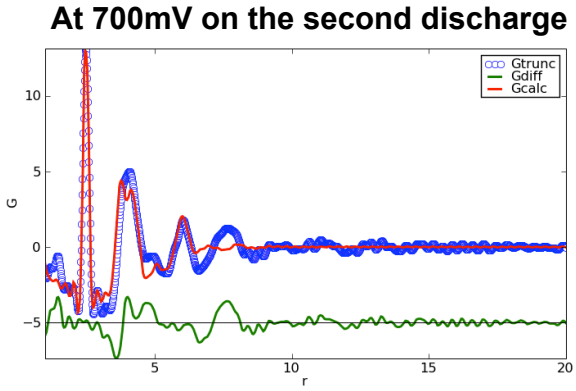

Figure 4.6. PDF refinement patterns of the lithiated n-Ge electrode at 700mV (R_w=0.3044).

In the dQ/dV plot, a broad peak at 650 mV is also observed, indicating the conversion of the Ge-Ge dumbbells phase to amorphous Ge. Further work to model the amorphous phase formed on delithiation will be performed.

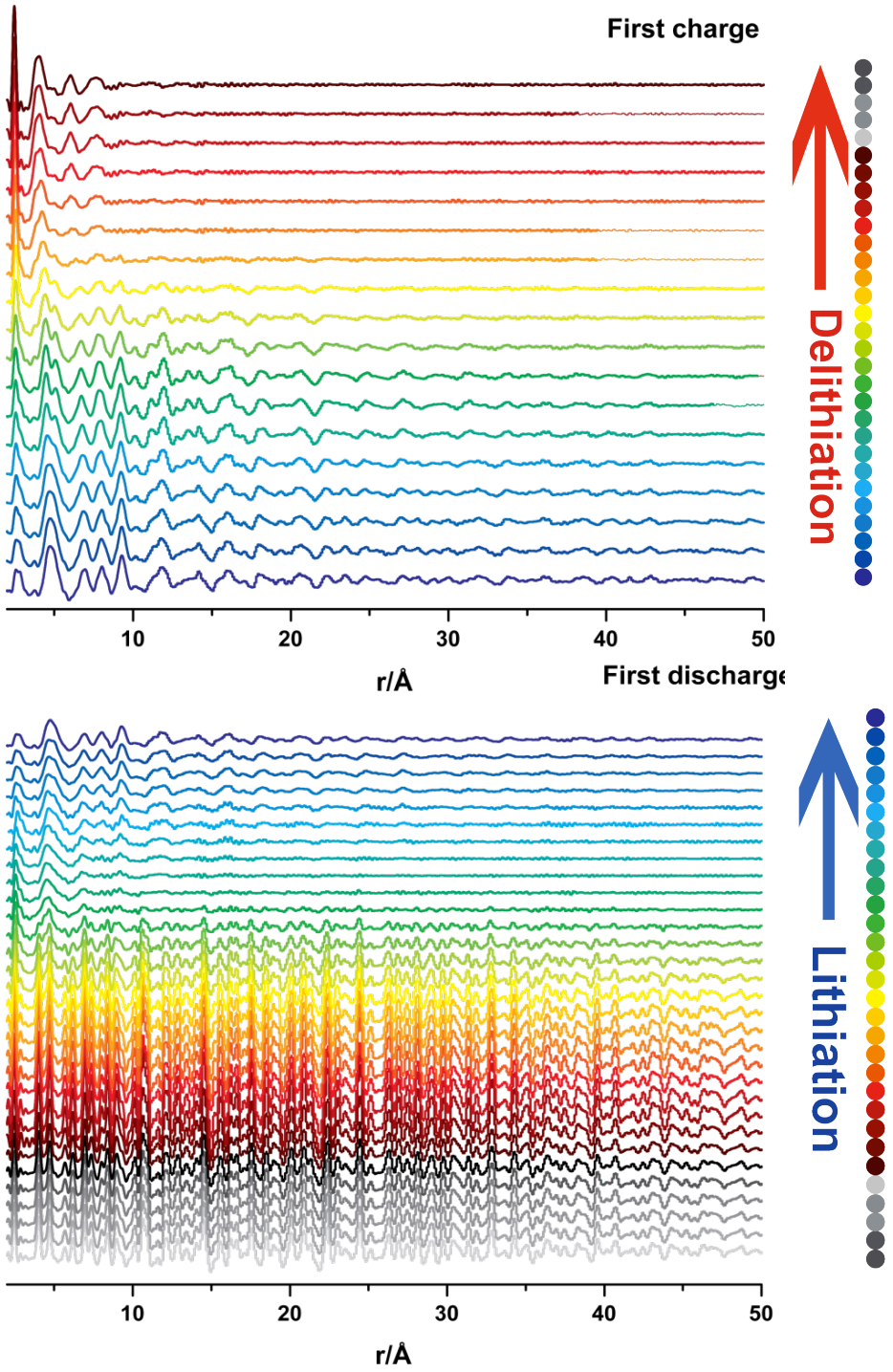

Figure 4.7. *In-situ* PDF patterns for n-Ge observed during the first (de) lithiation at a rate of C/15 out to 50Å.

Ex-situ NMR analysis was performed to identify ^{7}Li signals originating from (de) lithiated n-Ge phases. (Figure 4.8)

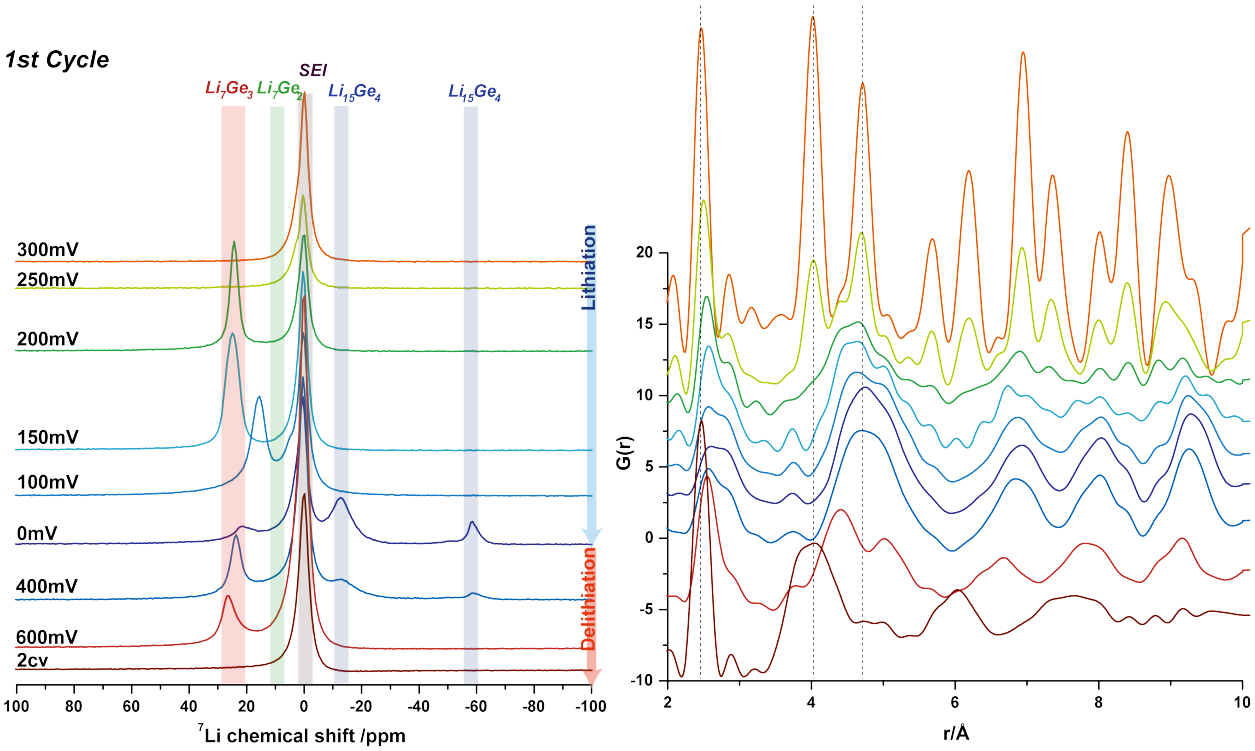

Figure 4.8. *Ex-situ* ^{7}Li NMR spectra of the first (de) lithiation of n-Ge electrodes at a rate of a C/15. Relevant NMR peak assignments are shown. The corresponding *in situ* PDF patterns for the selected NMR spectra are also plotted. The dashed lines in PDF patterns indicate the first, second, and third coordination shells of the crystalline cubic Ge phase.

The ^{7}Li NMR spectra at the early stage of discharge (~250 mV) are dominated by the characteristic SEI resonance around 0 ppm. The corresponding *in-situ* PDFs show the clear Ge-Ge correlations of cubic Ge phase at 300mV and the intensity of all Ge-Ge peaks decreases at 250 mV, indicating the reduction of the relative abundance of Ge-Ge bonds. A sharp resonance at 22 ppm appears, an indication of the formation of the Li_7Ge_3 phase. Unlike the synthesized Ge phase (Chapter 2), no broad component under the 22ppm peak is observed.

At 150 mV, the peak at 22 ppm is broadened and shifted to a lower chemical shift value at 15 ppm for the sample obtained at 100mV. In the previous study (Chapter 2), it was proposed that Li_7Ge_3 converts to Li_7Ge_2 via a series of the Ge-Ge dumbbell phases: $Li_{13}Ge_5$ and Li_8Ge_3. Therefore we propose that the resonance at 15 ppm can be tentatively assigned to an intermediate

phase, containing this Ge-Ge dumbbell structures and isolated Ge atoms, between Li_7Ge_3 and Li_7Ge_2. As the lithiation proceeds, Ge-Ge bonds are gradually broken and form the isolated Ge atoms.

Upon discharging to 0 mV, two major resonances are observed at -13 and -58 ppm, which can be assigned to $Li_{15}Ge_4$ phase, and a minor resonance at around 20 ppm is also observed, suggesting phases containing similar ^{7}Li local environment to that in Li_7Ge_3 remain. In contrast to the micron-sized Ge and a recent *in-situ* ^{7}Li NMR study[45], the resonance at -22 ppm was not observed. This resonance was ascribed to the overlithiated $Li_{15}Ge_4$ phase which is known as an electrochemically driven metastable phase[45]. This is an apparent discrepancy between the results obtained from *ex-situ* and *in-situ* NMR. As discussed in Chapter 3, the resonance at -22ppm can be the average positions of both crystallographic sites of $Li_{15}Ge_4$ phase due to fast exchange phenomenon of Li ion during *in-situ* experiment and the resonances at -13/-58 ppm possibly corresponding to each crystallographic site of $Li_{15}Ge_4$ phase.

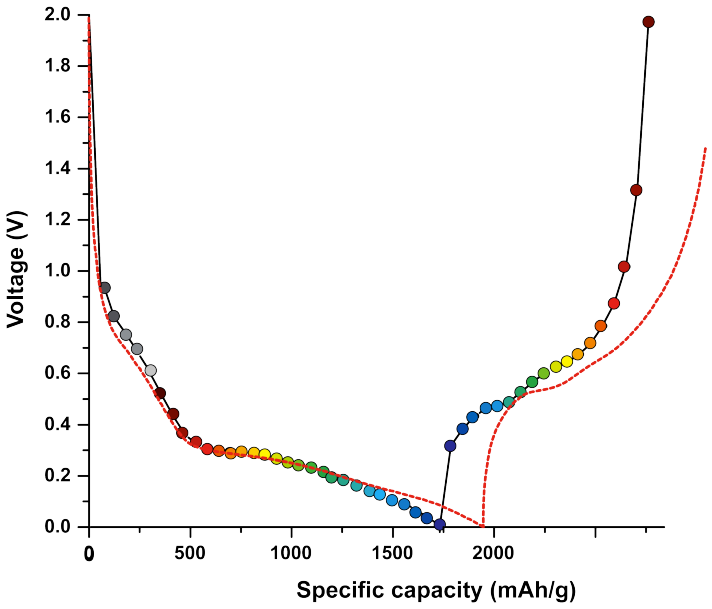

Figure 4.9. Comparison of the electrochemical profiles for the first cycle with coin cell (red dashed line) and AMPIX cell (black line with dots)

Furthermore, the final lithiation products at the end of the first discharge are different between *in-situ* PDF (Li_7Ge_2 major phase) and *ex-situ* NMR ($Li_{15}Ge_4$ major phase) measurements. As shown in Figure 4.9, there is no significant difference of the electrochemical profiles between

in-situ (AMPIX cell) and *ex-situ* (coin cell) measurements above 200 mV, but the second process below 200 mV is slightly curtailed in the *in situ* PDF measurement, reducing the capacity compared to coin-cell measurements. This would mean the transformation to $Li_{15}Ge_4$ is incomplete in the *in situ* measurement due to the challenges of low voltage experiments *in situ* electrochemical cells, but it does indicate that the final discharge product of the n-Ge is $Li_{15}Ge_4$, and explains the inconsistency between the *ex situ* NMR and *in situ* PDF.

During the charging process, the steep rising region at 400 mV in the dQ/dV plot shows the two major groups of resonances at 22ppm and -13/-58ppm, indicating that mixtures of Li_7Ge_3 and $Li_{15}Ge_4$ are present. By 600mV, only the resonance at 22 ppm exists and the signals from $Li_{15}Ge_4$ completely disappear. The characteristic two peaks between 4 and 6 Å appear in the corresponding PDFs, indicating the formation of Ge-Ge dumbbells. At the end of charge, the resonance at 22 ppm disappears, suggesting the phase transformation from Li_7Ge_3 to amorphous Ge, consistent with the PDF data.

The final lithiated products between *ex-situ* NMR and *in-situ* PDF results are inconsistent, so they might follow the different delithiation pathways, similar to what is observed in Si anodes.[46,47] Delithiation of $Li_{15}Ge_4$ may lead to the reformation of Li_7Ge_3 directly if delithiation follows the thermodynamic pathway and delithiation of a mixture of Li_7Ge_2 and $Li_{15}Ge_4$ may follow a reversible mechanism. This will be discussed later at the second cycle.

The Second Cycle

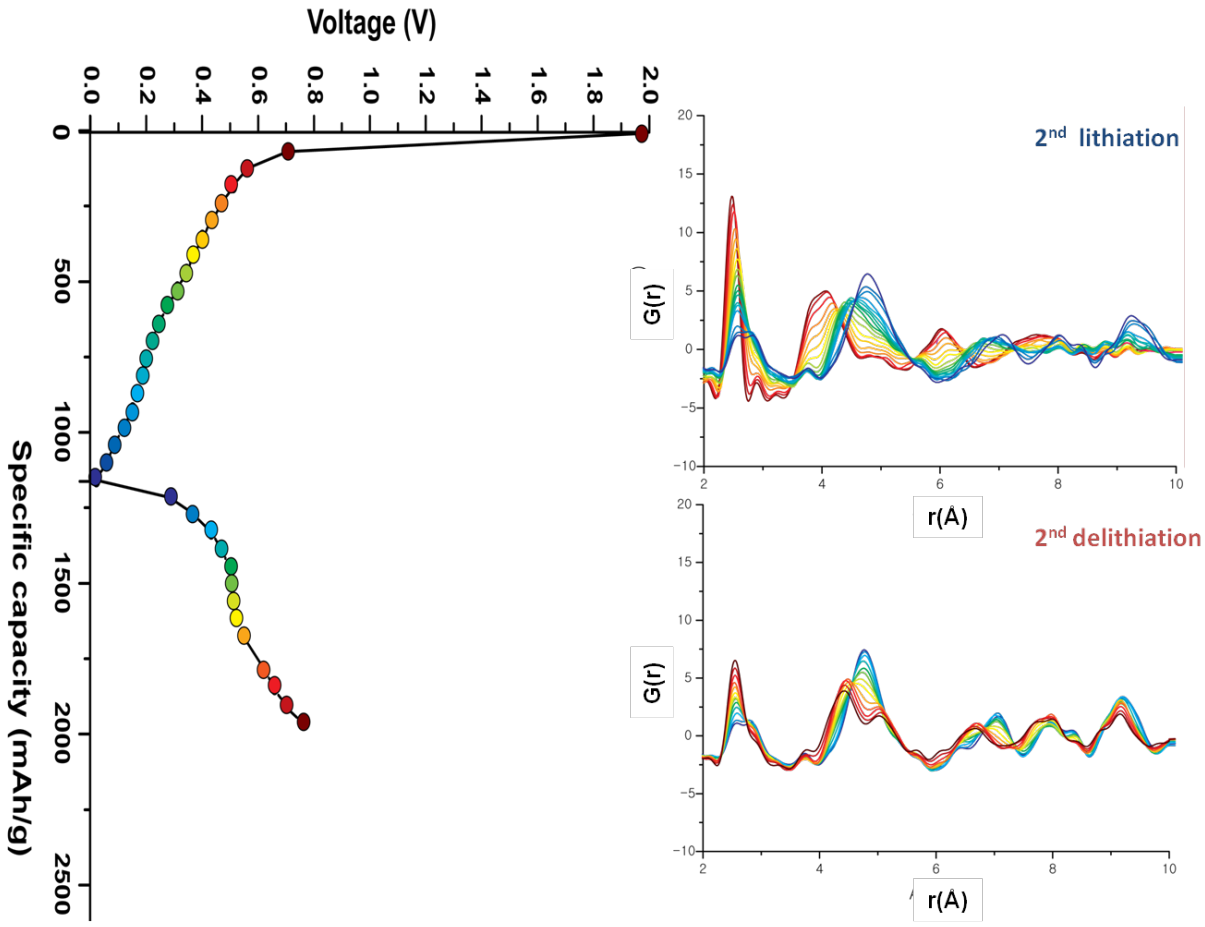

Figure 4.10. *In-situ* PDF patterns for n-Ge of the second (de) lithiation at a rate of C/15. The corresponding electrochemical discharge-charge curves are plotted using the same color-coding. Full PDF patterns are shown in Figure 4.12.

The second (de) lithiation of the amorphous Ge, formed after the 1st cycle, is monitored by using *in-situ* PDFs and *ex-situ* ^{7}Li NMR. At the early stages of discharge, the PDF shows little change from that of a-Ge until 500 mV. As the lithiation proceeds, the sharp peak at 2.5 Å gradually decreases and shifts to a higher value. The broad peak at 4 Å also shifts to larger values by 300 mV. Between 300 and 200mV, broad one peak is clearly observed around 4.5 Å. Unlike micron-sized Ge, the characteristic correlations from parallel-aligned Ge-Ge dumbbells are not clearly resolved into two peaks during the 1st/ 2nd discharging processes in n-Ge. Upon further lithiation, the broad peak at 2.7 Å from Li-Ge correlations grows and the Ge-Ge

dumbbell like correlations (broad peak at 4.5 Å) shift to 4.7 Å, indicating the formation of the Li_7Ge_2 or $Li_{15}Ge_4$ phases. At the end of discharge, the PDF patterns show correlations out to high-r values, suggesting the crystallization of the end phase, and these correlations are persisting until 500mV upon charging. (Figure 4.12) The best fit to the PDF pattern at 0mV on the second discharge is obtained with a combination of 75% Li_7Ge_2 and 25% $Li_{15}Ge_4$, suggesting an incomplete conversion to $Li_{15}Ge_4$ at the second discharge. (Figure 4.11) A larger spdiameter, which is used to determine the nanoparticle size, is observed in $Li_{15}Ge_4$ (102 Å), compared to the spdiameter of Li_7Ge_2 (30 Å), reflecting a relatively small correlation length of Li_7Ge_2 phase in this r-range.

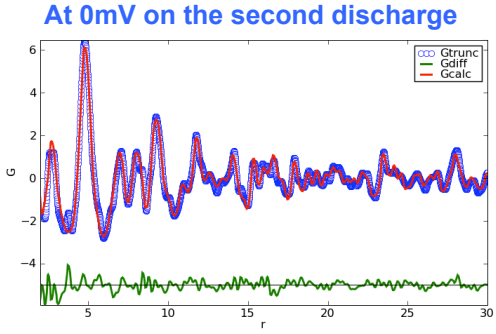

Li_7Ge_2	$Li_{15}Ge_4$	R_w
0.75	0.25	0.1892

Figure 4.11. PDF refinement at 0mV on the second discharge. The phase fraction and corresponding R_w value are listed in table.

By analogy with the first delithiation, the voltage profile starts with a steep rise to around 500mV, the small flatter region is followed by and a sharp peak at 630mV in the dQ/dV plot is observed. The PDF data are largely consistent with the electrochemical profiles. The peak at 4.7Å, from non-bonded Ge-Ge correlations, is converted to parallel-aligned Ge-Ge dumbbells phases by 700mV, as evidenced by the growth of the Ge-Ge peak at 2.5 Å and the splitting of the next nearest neighbor peak, characteristic of parallel-aligned dumbbells. *In-situ* PDF was only measured until 750mV on the second charge due to the limit of the scheduled beam time. However, the similarity of the electrochemistry on the first and second lithiation and on the basis of the previous studies and *ex-situ* ^{7}Li NMR results, we assume that these Ge-Ge dumbbells phases are converted to the amorphous Ge phase during the further charging process.

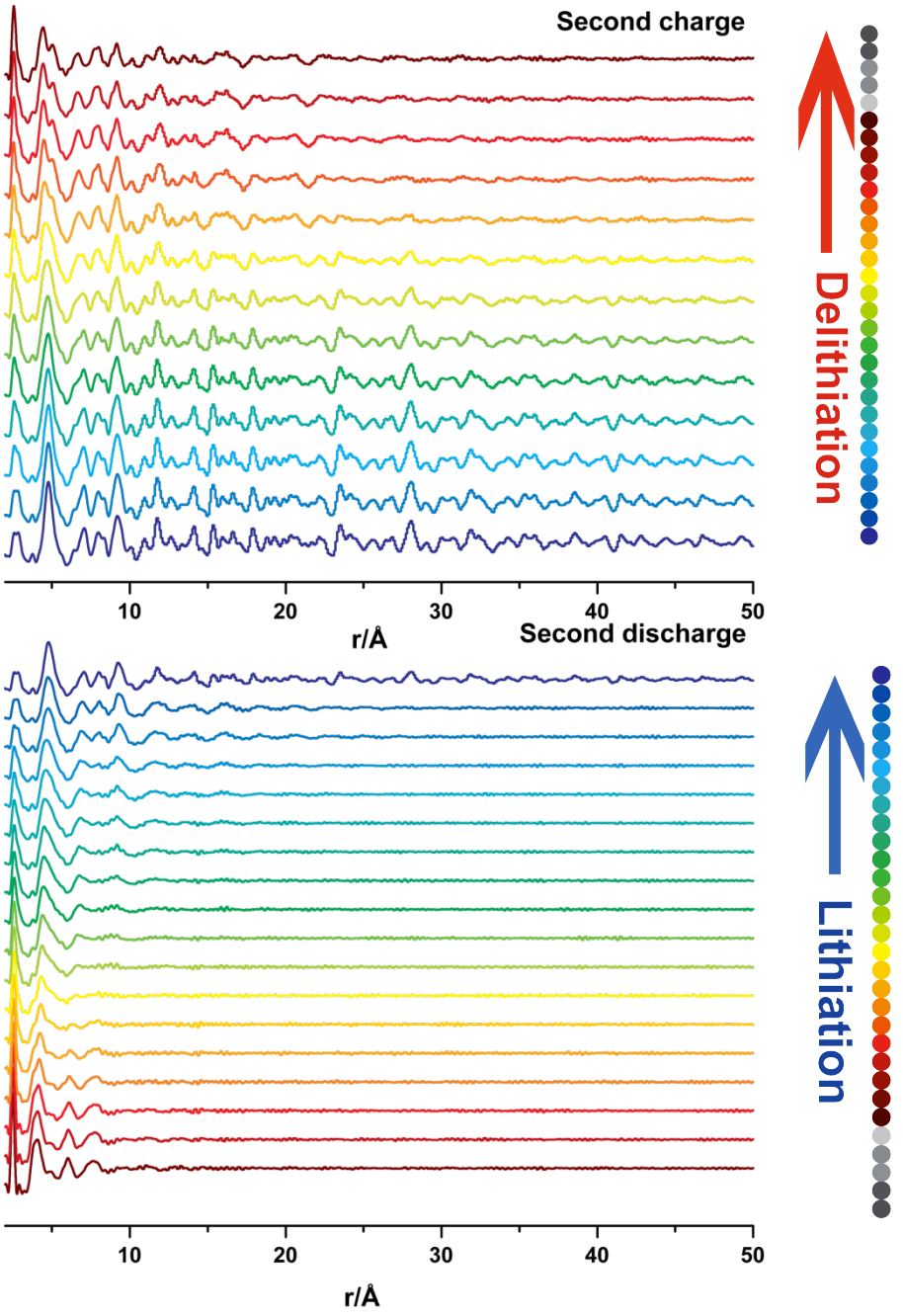

Figure 4.12. *In-situ* PDF patterns for n-Ge observed during the second (de) lithiation at a rate of C/15 out to 50Å. (Delithiation stopped at 750mV.)

The ^{7}Li NMR spectra (Figure 4.13) at the early stage of the second discharge (300mV) show a broad resonance centered around 19 ppm, tentatively indicating that the initial lithiation starts with the formation of disordered lithiated Ge phases, possibly within the matrix of the

amorphous germanium. The corresponding *in-situ* PDFs show the Ge-Ge correlations, but this correlation in the PDF is not clearly resolved to two peaks, indicating that the dumbbells formed are not parallel aligned as in Li_7Ge_3. Instead, an amorphous Li_7Ge_3 phase might be formed initially or Li_7Ge_3 might not be reformed on the lithiation of amorphous germanium, instead favoring the formation of structures, which do not feature alignment of dumbbells. It is noted, that the structure of amorphous germanium proposed by Walters *et al*[44], features a tetrahedral network, which does not offer easy kinetic pathways for the formation of parallel aligned dumbbells, compared to cubic germanium. This may be a factor in the different connectivity, which appears to form in this region. Further modeling of phases in this region is required.

The initial lithiation (300mV) at the second cycle occurs at a lower overpotential than the first cycle (200mV). A small resonance at 22 ppm appears at 200 mV and steadily grows by 100mV, an indication of the formation of the Li_7Ge_3 phase. A broad component is observed under the 22ppm and ascribed to the residual more disordered lithiated Ge phases. On the basis of the first lithiation results, the gradual structural transformation from Li_7Ge_3 to Li_7Ge_2 is suggested, but this gradual resonance shift is not detected in the second lithiation due to the limitation of *ex-situ* experiments. A recent *in-situ* ^{7}Li NMR study[45] showed a similar lithiation pathway to the first cycle except for the formation of $Li_{2.26}Ge$ occurred at more positive potential (0.17 V of the first lithiation→ 0.25 V of the second lithiation). This is similar to what was observed for Si[47] and suggests that the more porous structure of Si in the second cycle will speed up Li diffusion and the reaction kinetics. Weker *et al*[6] also suggested the increased porosity from Li extraction after the first cycle in micron-sized Ge. Thus, the voltage difference of initial lithiation can be attributed to the amorphous property of Ge.

Upon discharging to 0mV, two major resonances are observed at -13 and -58 ppm, which can be assigned to $Li_{15}Ge_4$, and a minor resonance at around 20 ppm is also observed, suggesting phases containing similar ^{7}Li local environments as that in Li_7Ge_3. The resonance at -22ppm is not detected at 0 mV.

In the charging process, two major resonances at -13/-58ppm and a minor resonance at around 20 ppm are observed at 500mV, indicating mixtures of residual Li_7Ge_3 and $Li_{15}Ge_4$, consistent with the observed in both electrochemical profiles and PDF patterns. At 600 mV, the broad resonance only exists unlike the first delithiation and the signals from $Li_{15}Ge_4$ completely disappear. In addition, the characteristic Ge-Ge dumbbells correlations appear in the

corresponding PDFs, indicating the formation of parallel aligned Ge-Ge dumbbells phases. At the end of charge, the broad resonance disappears, suggesting the phase transformation from the disordered lithiated Ge phases to amorphous Ge phase.

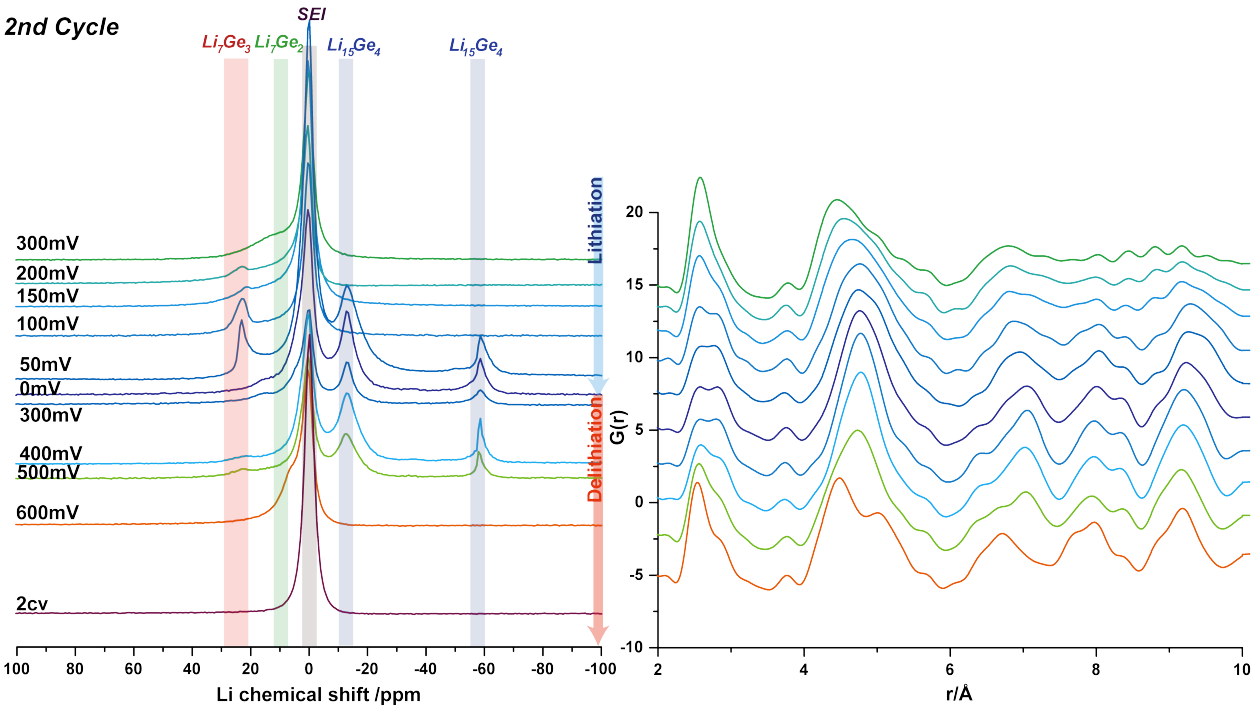

Figure 4.13. *Ex-situ* ^{7}Li NMR spectra of the second (de) lithiation of n-Ge electrodes at a rate of a C/20. Relevant NMR peak assignments are shown. The corresponding *in situ* PDF patterns for the selected NMR spectra are also plotted

Table 4.1 shows the summary of voltage profiles for structural changes in dQ/dV plots during the first cycle. Experimental conditions, such as current rates and binder systems, for each pristine Ge are different. Each Ge pristine material shows similar (de) lithiation pathways in the first cycle, but the structural phase transformations in potentials show the some variations and possibly depend on the size and morphology of Ge particles, the current rates, binders and electrolytes due to differences in electronic networking, tortuosities of the paths for Li^{+} in the electrode or electrolyte.

Table 4. 1. The summary of voltage profiles for the defined (de) lithiation processes at the first cycle.

First Cycle	n-Ge (20nm)	Synthesized-Ge (ave.2~3μm)	100 mesh Ge (<149μm)
Current rate	C/15	C/50	C/50
Binder system	PVDF	PVDF	CMC/PAA
SEI formation	700mV	500mV	350mV
The formation of Li_7Ge_3	280mV	350mV	270mV
Gradual structural transformation from Li_7Ge_3 to Li_7Ge_2	150mV	200mV	150mV
The formation of crystalline $Li_{15}Ge_4$	<100mV	50mV	100mV
Delithiation of crystalline $Li_{15}Ge_4$	540mV	-	450mV
The formation of amorphous Ge phase.	600mV	-	640mV

By correlating *in-situ* PDF, *ex-situ* NMR, and electrochemical results of crystalline n-Ge, a similar (de) lithiation pathway to micron-sized Ge system is observed during the first cycle.

The first cycle,

On discharge: n-Ge → Li_7Ge_3→a-Li_7Ge_2→ $Li_{15}Ge_4$ + a-Li_7Ge_2 (from incomplete conversion in *in-situ* PDF)

On charge: a-Ge← Li_7Ge_3 ←a-Li_7Ge_2← $Li_{15}Ge_4$+ a-Li_7Ge_2 (from incomplete conversion in *in-situ* PDF)

or

Amorphous n-Ge← Li_7Ge_3 ← $Li_{15}Ge_4$

In an analogy with the *in-situ* NMR results in chapter 3, only the *in-situ* PDF data support the existence of Li_7Ge_2 phase during charging and full conversion from Li_7Ge_2 to $Li_{15}Ge_4$ is not achieved at the end of discharge. Table 4.2 shows the phase compositions from refinement results at the first/second early stage of charging. The phase fractions of Li_7Ge_2 are almost constant upon charging, suggesting that it represents an inactive portion of the electrode

conversion at 0mV. Therefore, no evidence for reformation of Li_7Ge_2 from $Li_{15}Ge_4$ upon charging is also observed in the PDF. Further *ex-situ* PDF experiments are required to provide the more detailed information of structural transformations on charge.

Table 4.2. Phase composition from refinement results at the early stage of charge

1st charge	**Li_7Ge_3**	**Li_7Ge_2**	**$Li_{15}Ge_4$**	**R_w**	**2nd charge**	**Li_7Ge_3**	**Li_7Ge_2**	**$Li_{15}Ge_4$**	**R_w**
319mV	-	0.54	0.46	0.2166	287mV	-	0.63	0.37	0.1541
385mV	-	0.53	0.47	0.2178	371mV	-	0.63	0.37	0.1583
432mV	-	0.49	0.51	0.2269	431mV	-	0.63	0.37	0.1583

At the second cycle, (de) lithiation processes follow the highly disordered phase transformation, in contrast to the first cycle, and can be proposed below.

The second cycle,

On discharge: a-Ge → a-Li_xGe → a-Li_7Ge_3 →a-Li_7Ge_2→ $Li_{15}Ge_4$+ a-Li_7Ge_2 (from incomplete conversion in *in-situ* PDF)

On charge: a-Ge← a- dumbbell type Li_xGe ← $Li_{15}Ge_4$+ a-Li_7Ge_2 (from incomplete conversion in *in-situ* PDF)

Further works (*in-situ* NMR or *ex-situ* PDF experiments) are required to improve the currently proposed (de) lithiation mechanism.

4.3. Conclusions

The (de) lithiation mechanism of n-Ge anodes has been studied with *in-situ* PDF, and *ex situ* ^{7}Li NMR. The lithiation process of n-Ge anodes involves the formation of Li_7Ge_3 first through a two-phase reaction step, followed by its transformation to Li_7Ge_2, and then Li_7Ge_2 converts to crystalline $Li_{15}Ge_4$ at the end of lithiation at the first cycle. The in situ PDF studies show a lower capacity and therefore the end product is a mixture of $Li_{15}Ge_4$ and Li_7Ge_2. During delithiation, the extraction of Li from crystalline $Li_{15}Ge_4$ forms Li_7Ge_3, which eventually forms amorphous Ge. A similar (de) lithiation pathway occurs in subsequent cycles with highly disordered phase transformations, though differences in the alignment of Ge-Ge dumbbells in the Li_7Ge_3-like compound formed at the start of subsequent lithiation indicates that some differences in lithiation mechanism may exist This study provides complemental experimental evidence from PDF and NMR techniques for understanding the (de) lithiation mechanism of n-Ge anodes.

4.4. References

(1) Park, C. M.; Kim, J. H.; Kim, H.; Sohn, H. J. *Chem. Soc. Rev.* **2010**, *39*, 3115.

(2) Zhang, W.-J. *J. Power Sources* **2011**, *196*, 13.

(3) Fuller, C.; Ditzenberger, J. *Phys. Rev.* **1953**, *91*, 193.

(4) Wang, D. W.; Chang, Y. L.; Wang, Q.; Cao, J.; Farmer, D. B.; Gordon, R. G.; Dai, H. J. *J. Am.Chem.Soc.* **2004**, *126*, 11602.

(5) Li, D.; Seng, K. H.; Shi, D.; Chen, Z.; Liu, H. K.; Guo, Z. *J. Mater. Chem. A* **2013**, *1*, 14115.

(6) Weker, J. N.; Liu, N.; Misra, S.; Andrews, J. C.; Cui, Y.; Toney, M. F. *Energ. Environ. Sci.* **2014**, *7*, 2771.

(7) Cui, G. G., L.; Zhi, L.; Kaskhedikar, N.; van Aken, P. A.; Muellen, K.; Maier *J. Adv. Mater.* **2008**, *20*, 3079.

(8) Lee, H.; Kim, M. G.; Choi, C. H.; Sun, Y. K.; Yoon, C. S.; Cho, J. *J. Phys. Chem. B* **2005**, *109*, 20719.

(9) Seo, M. H.; Park, M. H.; Lee, K. T.; Kim, K.; Kim, J. H.; Cho, J. *Energ. Environ. Sci.* **2011**, *4*, 425.

(10) Chan, C. K.; Zhang, X. F.; Cui, Y. *Nano. Lett.* **2008**, *8*, 307.

(11) Ko, Y. D.; Kang, J. G.; Lee, G. H.; Park, J. G.; Park, K. S.; Jin, Y. H.; Kim, D. W. *Nanoscale* **2011**, *3*, 3371.

(12) Cui, G. G., L.; Kaskhedikar, N.; van Aken, P. A.; Maier, J. *Electrochim Acta* **2010**, *55*, 985.

(13) Park, M. H.; Cho, Y.; K. Kim; J. Kim; M. L. Liu; Cho, J. *Angew. Chem.* **2011**, *123*, 9821.

(14) Jia , H.; Kloepsch, R.; He , X.; Badillo, J. P.; Gao, P.; Fromm, O.; Placke, T.; Winter, M. *Chem. mater.* **2014**, *26*, 5683.

(15) Yang, L. C.; Gao, Q. S.; Li, L.; Tang, Y. D.; Wu, Y. P. *Electrochem. Commun.* **2010**, *12*.

(16) Park, M. H.; Kim, K.; Kim, J.; Cho, J. *Adv. Mater.* **2010**, *22*, 415.

(17) Lee, H. C., J. *Nano Lett.* **2007,**, *7,* , 2638.

(18) Kim, M. G. C., J. *J. Electrochem. Soc.* **2009,** , *156,*, A277.

(19) Seng, K. H.; Park, M.-H.; Guo, Z. P. L., H. K.; Cho, J. *Angew. Chem. Int. Ed.* **2012**, *51*, 5657.

(20) DiLeo, R. A. F., S.; Ganter, M. J.; Rogers, R. E.; Raffaelle, R. P.; Landi, B. J. *J. Phys. Chem. C* **2011**, *115*, 22609.

(21) Wang, X.-L.; Han, W.-Q.; H. Chen; Bai, J.; Tyson, T. A.; Yu, X.-Q.; Wang, X.-J.; Yang, X.-Q. *J. Am. Chem. Soc.* **2011,** , *133,* , 20692.

(22) Lee, H.; Kim, H.; Doo, S.; Cho, J. *J. Electrochem. Soc.* **2007**, *154*, A343.

(23) Li, X.; Liang, J.; Hou, Z.; Zhu, Y.; Wang, Y.; Qian, Y. *Chem. Commun.* **2015**, *51*, 3882.

(24) Xu, Y.; Zhu, X.; Zhou, X.; Liu, X.; Liu, Y.; Dai, Z.; Bao, J. *J. Phys. Chem. C* **2014**, *118*, 28502.

(25) Xue, D.-J.; Xin, S.; Yan, Y.; Jiang, K.-C.; Yin, Y.-X.; Guo, Y.-G.; Wan, L.-J. *J. Am. Chem. Soc.* **2012**, *134*, 2512.

(26) Zhong, C.; Wang, J.-Z.; Gao, X.-W.; Wexler, D.; Liu, H.-K. *J. Mater. Chem. A* **2013**, *1*, 10798.

(27) Seng, K. H.; Park, M. H.; Guo, Z. P.; Liu, H. K.; Cho, J. *Angewandte Chemie* **2012**, *51*, 5657.

(28) Nitta, N.; Yushin, G. *Part. Part. Syst. Charact.* **2014**, *31*, 317.

(29) Seng, K. H.; Park, M. H.; Guo, Z. P.; Liu, H. K.; Cho, J. *Nano letters* **2013**, *13*, 1230.

(30) Wang, X.-L.; Han, W.-Q.; Chen, H.; Bai, J.; Tyson, T. A.; Yu, X.-Q.; Wang, X.-J.; Yang, X.-Q. *J. Am. Chem. Soc.* **2011**, *133*, 20692.

(31) Graetz, J.; Ahn, C. C.; Yazami, R.; Fultz, B. *J Electrochem Soc* **2004**, *151*, A698.

(32) Borkiewicz, O. J.; Shyam, B.; Wiaderek, K. M.; Kurtz, C.; Chupas, P. J.; Chapman, K. W. *J. Appl. Crystallogr.* **2012**, *45*, 1261.

(33) Chupas, P. J.; Qiu, X.; Hanson, J. C.; Lee, P. L.; Grey, C. P.; Billinge, S. J. L. *J. Appl. Crystallogr.* **2003**, *36*, 1342.

(34) Chupas, P. J.; Chapman, K. W.; Lee, P. L. *J. Appl. Crystallogr.* **2007**, *40*, 463.

(35) Hammersley, A. P.; Svensson, S. O.; Hanfland, M.; Fitch, A. N.; Häusermann, D. *High Pressure Res.* **1996**, *14*, 235.

(36) Qiu, X.; Thompson, J. W.; Billinge, S. J. L. *J. Appl. Crystallogr.* **2004**, *37*, 678.

(37) Farrow, C. L.; Juhás, P.; Liu, J. W.; Bryndin, D.; Božin, E. S.; Bloch, J.; Proffen, T.; Billinge, S. J. L. *J. Phys.: Condens. Matter* **2007**, *19*, 335219.

(38) Zhang, W.-J. *J. Power Sources* **2011**, *196*, 877.

(39) Obrovaca, M. N.; Krauseb, L. J. *J. Electrochem. Soc.* **2007**, *154*, A103.

(40) Lim, L. Y.; Liu, N.; Cui, Y.; Toney, M. F. *Chem. Mater.* **2014**, *26*, 3739.

(41) Cho, Y. J.; Im, H. S.; Kim, H. S.; Myung, Y.; Back, S. H.; Lim, Y. R.; Jung, C. S.; Jang, D. M.; Park, J.; Cha, E. H.; Cho, W. I.; Shojaei, F.; Kang, H. S. *ACS Nano* **2013**, *7*, 9075.

(42) Kasper, J. S.; Richards, S. M. *Acta Cryst.* **1964**, *17*, 752.

(43) Etherington, G.; Wright, A. C.; Wenzel, J. T.; Dore, J. C.; Claeke, J. H.; Sinclair, R. N. *J. Non-Cryst. Solid* **1982**, *48*.

(44) Walters, J. K.; Newport, R. J. *Phys. Rev. B: Condens. Matter Mater. Phys.* **1996**, *53*.

(45) Tang, W.; Liu, Y.; Peng, C.; Hu, M. Y.; Deng, X.; Lin, M.; Hu, J. Z.; Loh, K. P. *J. Am.Chem. Soc.* **2015**, *137*, 2600.

(46) Key, B.; Morcrette, M.; Tarascon, J.-M.; Grey, C. P. *J Am Chem Soc* **2010**, *133*, 503.

(47) Ogata, K.; Salager, E.; Kerr, C. J.; Fraser, A. E.; Ducati, C.; Morris, A. J.; Hofmann, S.; Grey, C. P. *Nature communications* **2014**, *5*, 3217.

Chapter 5

Studies of Li_xSn_y by XRD, $^{7}Li/^{119}Sn$ MAS NMR and PDF analysis

Abstract

Metallic tin is a promising anode material in secondary lithium-ion batteries (LIBs) due to its high capacity (993 mAh/g) and compatibility with other elements. Here, several Li_xSn_y crystalline phases, Li_2Sn_5, Li_7Sn_3, Li_7Sn_2, and $Li_{17}Sn_4$ prepared by ball milling and an annealing process, and LiSn prepared by electrochemical lithiation, have been characterized with XRD, ^{7}Li / ^{119}Sn solid state nuclear magnetic resonance (NMR) spectroscopy, and pair distribution function (PDF) analysis. The local structure of crystalline Li_xSn_y has been investigated in order to obtain a set of trends in ^{7}Li and ^{119}Sn NMR spectra.

5.1. Introduction

Tin based materials are very attractive anode materials due to their high energy densities[1,2] and have slightly higher operating potentials compared to graphite, which reduces the safety issues associated with metallic lithium deposition.[3] Tin undergoes a reversible alloying process with lithium and exhibits a high theoretical capacity of 993 mAh/g.[4]

During electrochemical cycling, each mole of Sn theoretically can take up 4.4 Li atoms to form a $Li_{4.4}Sn$ alloy phase, but the associated volume expansion is approximately 260%, which can cause cracking and a loss of reversible capacity.[5] When Sn reacts with lithium, it forms several Li-Sn alloy phases, which have different lattice parameters and structures. Therefore, stress occurs while converting from one phase to the other. This stress is usually released by cracking or fragmentation of the Sn particles[5]. To overcome the problem of the huge volume change, various approaches have been reported to improve the cycling stability of tin. Multiphase composites, such as with inactive matrixes or carbon-based composites and nano-structured/ nano composite materials are being widely explored for the next-generation LIBs.[4]

Several groups have studied the Li-Sn model compounds utilizing ^{7}Li NMR.[6,7] Furuya *et al*.[6] investigated a series of Li_xSn_y alloys by means of static solid-state ^{7}Li NMR and reported that $Li_{22}Sn_5$/LiSn/$LiSn_2$ show a relatively large Knight shift, while Li_7Sn_2/Li_5Sn_2, defined as ionic alloys, show a small shift. Bekaert *et al.*[7], in a high resolution magic-angle spinning (MAS) ^{7}Li NMR study of Li-Sn model compounds supported by electronic structure calculations using density functional theory (DFT), determined ^{7}Li shifts of each model compound and demonstrated a good correlation between the participation of the Li to the DOS at the Fermi level and the corresponding ^{7}Li NMR shifts. Three different ranges of Li Knight shift are observed for metallic $Li_{22}Sn_5$, Li-rich Li_xSn_y (Li_7Sn_3, Li_5Sn_2, $Li_{13}Sn_5$ and Li_7Sn_2) and Sn-rich Li_xSn_y (Li_2Sn_5 and LiSn) compounds. $Li_{22}Sn_5$ is dominated by the DOS at metallic lithium and Sn-rich Li compounds are affected by the covalent Sn-Sn interactions, giving a high DOS at the Fermi level. Thus, these compounds show higher Knight shift values. All of the other Li

rich Li_xSn_y compounds (Li_7Sn_3, Li_5Sn_2, $Li_{13}Sn_5$ and Li_7Sn_2) have lower Knight Shift values due to decreased contributions of the Sn-Sn bond.

Several groups[8-11] have studied electrochemically lithiated Sn-based materials such as TCO (tin-based amorphous composite oxide), SnO, SnO_2, and Sn via ^{7}Li NMR. They all reported relatively low shifts (<10 ppm) for the fully electrochemically lithiated Sn compounds. Idota *et al.*[12] suggested that this shift could be not regarded as a Knight shift and these compounds did not have a metallic Li environment. Wang *et al.*[10] suggested that a melt-prepared Li-Sn alloy and an electrochemically lithiated SnO at the maximum Li content have different local structures and electronic environments of Li. Goward *et al.*[8] also suggested that the absence of a Knight shift for electrochemically lithiated SnO could be explained by the small size of Li-Sn domains, where the free motion of conduction electrons is suppressed.

In this chapter, relevant Li_xSn_y model compounds (with nominal compositions Li_2Sn_5, LiSn, Li_7Sn_3, Li_7Sn_2, and $Li_{22}Sn_5$) have been prepared by solid-state synthesis and electrochemical lithiation and probed using XRD, X-ray pair-distribution function (PDF) analysis, and high-resolution ^{7}Li and ^{119}Sn solid-state NMR spectroscopy. Solid-state NMR has been a powerful technique for probing the local structures and electronic properties of electrode materials for LIBs. Solid-state NMR is an element-specific technique that is very sensitive to the local environment of the nucleus probed, in this case ^{7}Li and ^{119}Sn. PDF analysis is a total scattering method, utilizing Bragg scattering and diffuse scattering in equal weighting, thus, it is a particularly powerful technique for characterizing amorphous and disordered systems. These characterization methods will assist with the identification and structural determination of the Li_xSn_y phases that form during electrochemical lithiation.

5.2. Experimental section

5.2.1.Preparation of model compounds

5.2.1.1. Synthesis

The lithium-tin model compounds (Li_2Sn_5, Li_7Sn_3, Li_7Sn_2, and $Li_{22}Sn_5$) were prepared by mechanical mixing. Stoichiometric amounts of lithium foil (Aldrich) and tin metal (Alfa Aesar, 325 mesh, 99.999%) were placed in a zirconium ball mill jar in an Ar-filled glove box and ball milled for 8 hours in a SPEX SamplePrep8000 Mixer/Mill high energy ball mill. The mechanically alloyed powder was transferred back into the glove box, packed into a stainless steel tube, inserted into a schlenk tube, and heated at a T_{ann} (annealing temperature) under vacuum. The sample preparation temperature and time are given in Table 5.1. Annealing conditions were determined on the basis of previous studies[13,14]. The final products were stored under Argon atmosphere before characterization.

Table 5. 1. Annealing conditions used to synthesize Li-Sn model compounds

	High Energy ball milling	Annealing condition
Li_2Sn_5	8hr	300°C/40hr
Li_7Sn_3	8hr	400°C/24hr
Li_7Sn_2	8hr	600°C/67hr
$Li_{22}Sn_5$	8hr	550°C/67hr

5.2.1.2. Electrochemical lithiation

LiSn was prepared by electrochemical lithiation. Coin cells were assembled in an Ar filled glove box using Li metal foil (Aldrich) as the negative electrode and tin metal (Alfa Aesar, 325 mesh, 99.999%) as the positive electrode. 1M $LiPF_6$ in a 1:1 volumetric mixture of ethylene carbonate (EC) and dimethyl carbonate (DMC) was used as the electrolyte and a porous glass fiber (GF/B, Whatmann) as the separator. The cells were cycled using an Arbin instruments battery cycler with a cycling rate of C/100 (corresponding to a discharge to a theoretical capacity of 993 mAh/g in 100 hours, assuming that $Li_{4.4}Sn$ is the final electrochemical lithiation product[15]) between 0.0 and 2.0 V at room temperature. After electrochemical cycling, each cell was dissembled and

the active material was washed with dimethyl carbonate (DMC, 99+% Sigma-Aldrich) and dried in the Ar-filled glove box.

5.2.2. X-ray Diffraction

Diffraction patterns were measured on a Bruker D8 diffractometer using Cu Kα irradiation (λ=1.54Å) with a scan rate of 3°/min for a 2θ range of 10° to 80°. Samples were sealed with an airtight cover under an Ar atmosphere before being loaded into the XRD holder.

5.2.3. *Ex situ* Pair distribution function analysis

Dried *ex situ* samples for PDF analysis were loaded into 1-mm diameter Kapton capillaries in an Ar-filled glovebox and sealed with epoxy. Total scattering data were acquired at the dedicated PDF beamline 11-ID-B at the Advanced Photon Source, Argonne National Laboratory. High-energy X-rays (~58 keV, λ = 0.2128 Å) were used in combination with a large amorphous-silicon based area detector (Perkin-Elmer) to collect X-ray scattering data to high values of momentum transfer ($\mathbf{Q}_{max} \approx 23$ Å). The scattering images were reduced to one-dimensional data within FIT2D[16] using CeO_2 as a calibration standard. The data were corrected for background scattering, Compton scattering and detector effects within pdfgetX2[17] and Fourier transformed to get $\mathbf{G}(\mathbf{r})$, the PDF. No attempt was made to subtract the carbon signals from the total PDF pattern. Least-squares refinements of structures against PDF data were performed in PDFGui[18] in the distance range of 0 – 30 Å.[18] The initial value for the Q_{damp} parameter was set as 0.045 and refined against the data for crystalline Sn, and the atomic displacement parameters were set to initial values of $U_{11}=U_{22}=U_{33} = 0.005Å^2$ (constrained to be equal for all the Sn and Li atoms) and $U_{12}=U_{23}=U_{13}=0$. Q_{damp}, lattice parameters, the linear atomic correlation factor (delta 1), and anisotropic temperature factors (U_{11}, U_{22}, U_{33}) were refined. The fractional coordinates factors (x, y, z) were not refined here. The initial refinements of each PDF pattern assume a single pure phase; however, incorporation of a second minor phase significantly improved the refinement quality of some patterns, as indicated by reduced refinement quality factors, i.e., the R_w values. Note that the value of

R_w-factors for PDF refinements is higher than those for a Rietveld refinement of similar merit.

5.2.4. *Ex situ* ^{7}Li and ^{119}Sn Solid State NMR

Ex situ samples were packed in 1.3 mm diameter Zirconia rotors in an Ar-filled glove box. Only Li_2Sn_5 is mixed with dry silica (50 wt%). High-resolution ^{7}Li MAS NMR spectra were acquired on a Varian InfinityPlus-500 MHz spectrometer at a magnetic field of 11.7 T, with a 1.3 mm MAS probe (Ago Samoson) at a spinning speed of 50 kHz. ^{7}Li NMR spectra were acquired using a rotor-synchronized spin-echo sequence (90°-τ-180°-τ-acq), where τ-values were set to be equal to one rotor period, i.e., 20 μs. The 90° pulse length was 2.2 μs and the recycle delay was 10 s. ^{7}Li spectra were referenced to a 1M ^{7}LiCl solution at 0 ppm and were normalized for analysis on the basis of the number of acquisitions and sample mass.

^{119}Sn spin-echo mapping[19-23] (or VOCS[24-26], variable offset cumulative spectrum) experiments were performed at 11.7 T on a Varian Infinity Plus spectrometer with a 1.3 mm MAS probe. The ^{119}Sn spectra were reference to SnO_2 powder set at -604.3 ppm. ^{119}Sn NMR spectra were acquired using a rotor-synchronized spin-echo sequence (90°-τ-180°-τ-acq), where τ-values were set to be equal to one rotor period. The 90^{o} pulse length was 1.8 μs and the recycle delay 0.3s. The irradiation frequency was varied with a step size of 0.14 MHz (750 ppm) over a range of about 1.5 MHz, where the step size was chosen to be less than ω_1.[27,28] Table 5.2 shows ^{119}Sn spin-echo mapping experimental conditions for each sample.

Table 5.2. ^{119}Sn spin-echo mapping experimental conditions for each compound.

	Irradiation frequency offset (ppm)	Spinning speeds (kHz)
β-Sn	8250/7500/6750/6000/5250	40
	6750	30/35/40
Li_2Sn_5	7500/6750/6000	25
	6750	25/30/35
LiSn	7500/6750/6000/4500/3750/3000/2250/1500/750/0	35
	6750/6000	35/40/45
Li_7Sn_3	4500/3750/3000/2250/1500/750/0/-750	35

	750	30/35/40
Li_7Sn_2	3000/2250/1500/750/0/-750/-1500	35
	750	30/35/40
$Li_{22}Sn_5$	7500/6000/4500/3750/3000/2250/1500/750/0/-750/-1500	35

5.3. Results and Discussion

5.3.1. Li_xSn_y Alloy Model Compounds

Nominal Li_2Sn_5, Li_7Sn_3, Li_7Sn_2 and $Li_{22}Sn_5$ were prepared by a high-energy ball-milling/ annealing process and LiSn was prepared by electrochemical lithiation. Li_xSn_y model compounds were characterized by XRD, PDF analysis and $^7Li/^{119}Sn$ solid-state NMR.

5.3.2. X-ray Diffraction (XRD) and Pair Distribution Function (PDF) analysis

The XRD patterns of Sn metal (β-Sn) and nominal compositions of Li_xSn_y (Li_2Sn_5, LiSn, Li_7Sn_3, Li_7Sn_2 and $Li_{22}Sn_5$) compounds are shown in Figure 5.1. Calculated PDFs with their fit to experimental data are found in Figure 5.2, and the refinement statistics (residual values and phase fractions) are listed in Table 5.3.

The XRD pattern of Li_2Sn_5 can be indexed by the Li_2Sn_5 structure reported by Hansen *et al.*[29] and shows the presence of unreacted β-Sn. This is confirmed by the refinement against PDF data, which shows 64% Li_2Sn_5 and 36% Sn. When a PDF refinement using a single Li_2Sn_5 phase is performed, an extremely poor fit is obtained (R_w=0.5837), but a much-improved fit (R_w=0.0903) is observed by addition of the β-Sn phase. This Li_2Sn_5 compound was prepared only by high-energy ball-milling without further annealing, thus the atomic positions might be slightly disordered or the major phase might be amorphous. The ball-milled Li_2Sn_5 phase is clearly detected in XRD, the long-range order technique, but there is a poor match in the short-range order techniques such as PDF analysis or ^{119}Sn NMR (discussed later).

The XRD reflections from LiSn, Li_7Sn_3, and Li_7Sn_2 can be indexed by the structures reported by Müller *et al.*[30], Müller[31], and Frank *et al.*[32], repectively. The initial refinements of Li_7Sn_3 (R_w=0.1588) and Li_7Sn_2 (R_w=0.1562) as a single phase againt PDF data show excellent fits. The best fit of Li_7Sn_3 to experimental PDF data is obtained with a combination of 83% Li_7Sn_3 and 17% LiSn. The R_w value of the nominal Li_7Sn_2 is also

improved by incorporating a second minor phase, giving a better fit with a phase fraction of 94% Li_7Sn_2 and 6% $Li_{13}Sn_5$.

The X-ray pattern of the phase with nominal composition $Li_{22}Sn_5$ gives a good match with the $Li_{22}Sn_5$ structure reported by Gladyshevski *et al.*[33] and the $Li_{17}Sn_4$ structure revised by Lupu *et al.*[34] due to almost identical XRD patterns. Both structures have the same number and similar positions of Sn crystallographic sites in the unit cell that gives rise to almost indistinguishable XRD patterns. However, their number of Li crystallographic sites and positions are different ($Li_{22}Sn_5$ has16 Li and $Li_{17}Sn_4$ has 13 Li crystallographic sites). When a PDF refinement using the $Li_{17}Sn_4$ structure is performed, a better fit with lower R_w value is obtained compared to using the $Li_{22}Sn_5$ structure (Figure 5.3 and Table 5.4). Addition of a Li_7Sn_2 phase in the $Li_{17}Sn_4$ phase reduces the R_w of the refinement from 22.2% to 10.0%, whereas, the $Li_{22}Sn_5$ phase with the addition of the Li_7Sn_2 phase only reduces the R_w value from 24.6% to 16.1%. Moreover, extremely large Li thermal parameters are obtained in the refinement using the $Li_{22}Sn_5$ phase, which indicates that a higher degree of disorder is required to fit the PDF data (Table 5.4). The best fit to the nominal $Li_{22}Sn_5$ phase is obtained with phase fraction of 73% $Li_{17}Sn_4$ and 27% Li_7Sn_2. Moreover, a recent DFT calculation of the Li-Si and Li-Ge system[35], predicts that $Li_{17}Si_4$ and $Li_{17}Ge_4$ are the stable phase on the tie line, while $Li_{22}X_5$ and $Li_{21}X_5$ (X=Si and Ge) are above the tie line, indicating they are metastable phases. Therefore, the synthesized Li richest model compound is assigned to $Li_{17}Sn_4$ on the basis of PDF refinement statistics.

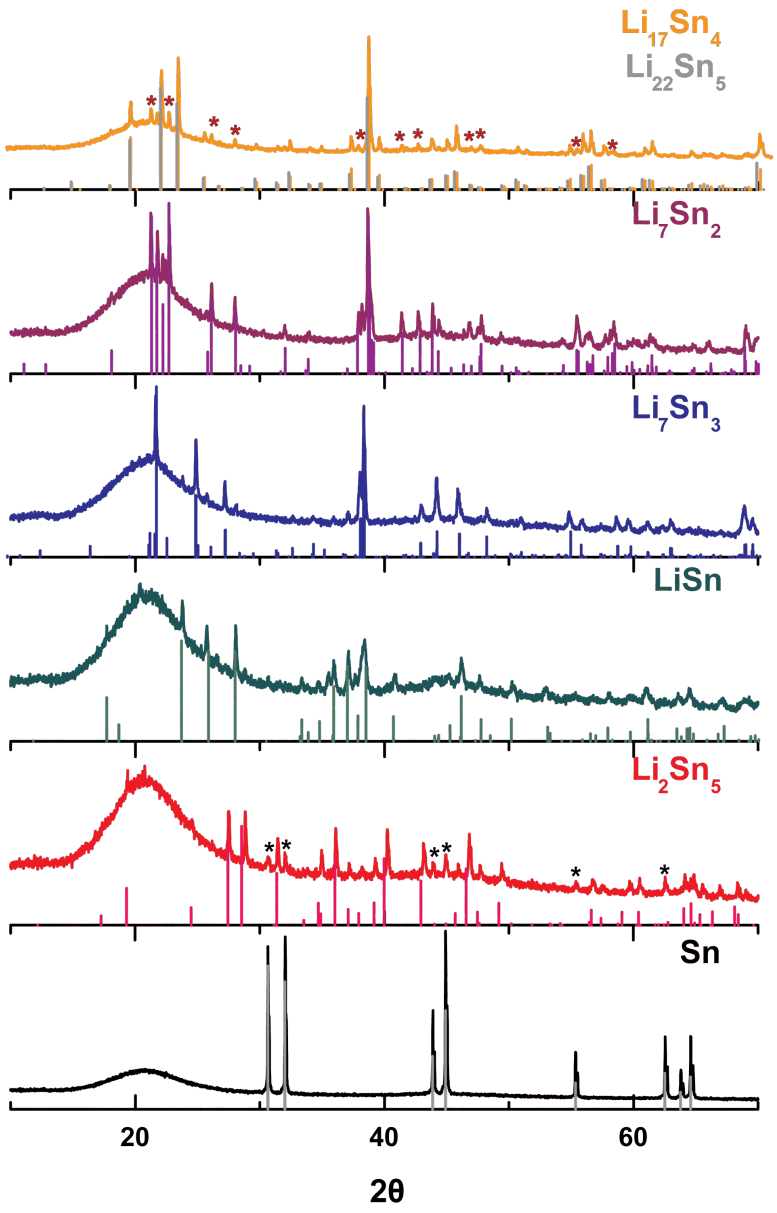

Figure 5.1. X-ray diffraction data (λ=1.54 Å) for the phases obtained by either a high-energy ball-milling and annealing process or by electrochemical lithiation with nominal stoichiometries; Sn, Li_2Sn_5, LiSn, Li_7Sn_3, Li_7Sn_2 and $Li_{22}Sn_5$. The calculated peak intensities below each pattern correspond to the simulated patterns for the corresponding structures. Both the $Li_{22}Sn_5$ and $Li_{17}Sn_4$ simulated patterns are shown below the experimental nominal $Li_{22}Sn_5$ pattern. $Li_{22}Sn_5$ has a minor Li_7Sn_2 phase (* mark). Li_2Sn_5 phase is a not pure phase, and contains reflections from Sn metal (* mark). The broad background centered at 2θ = 20°, most noticeable in the patterns of the poorly crystalline phases, comes from the Kapton sample holder.

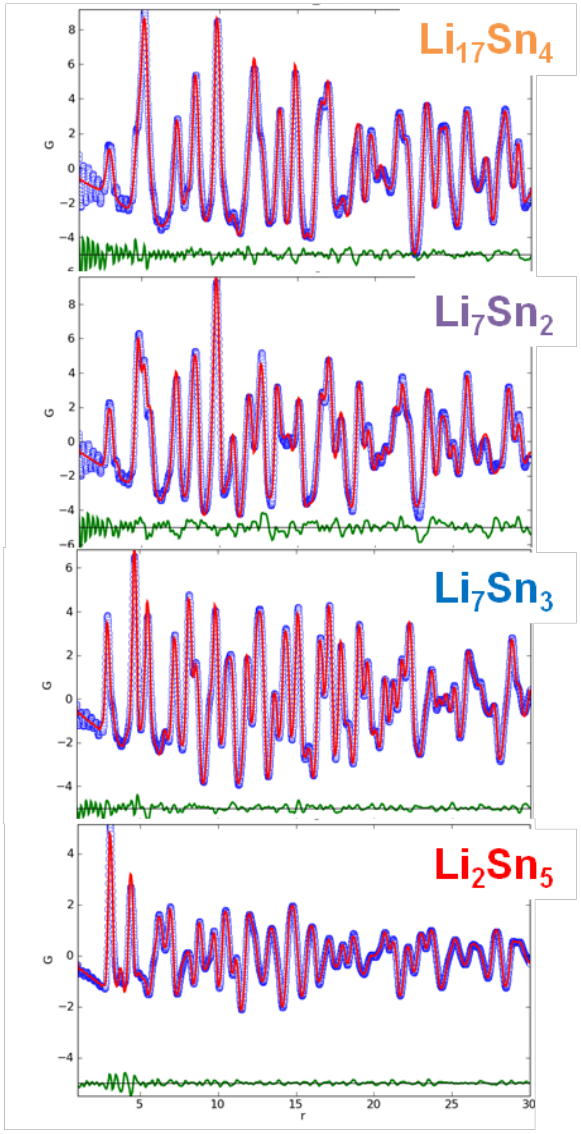

Figure 5.2. PDF (G(r)) patterns (blue) of the model compounds: Li_2Sn_5 (64% Li_2Sn_5 and 36% Sn) Li_7Sn_3 (83% Li_7Sn_3 and 17% LiSn*)*, Li_7Sn_2 (94% Li_7Sn_2 and 6% $Li_{13}Sn_5$), and $Li_{17}Sn_4$ (nominal $Li_{22}Sn_5$) (73% $Li_{17}Sn_4$ and 27% Li_7Sn_2). The refinement patterns are shown in red with green lines representing the difference between the experimental and refined pattern. Further details including the chemical phases, their corresponding weighting factors, and refinement statistics are shown in Table 5.3.

Table 5.3. The distribution of Sn in different phases in the model compounds with corresponding R_w values for the fit to experimental data. The relative abundance of each phase is determined from the unit cell content from the fits to PDF data.

Composition	Phase 1	Phase 2	R_w
Li_2Sn_5	1 (Li_2Sn_5)	-	0.5837
	0.64 (Li_2Sn_5)	0.36 (β-Sn)	0.0903
Li_7Sn_3	1 (Li_7Sn_3)	-	0.1588
	0.83 (Li_7Sn_3)	0.17 (LiSn)	0.07207
Li_7Sn_2	1 (Li_7Sn_2)	-	0.1562
	0.94 (Li_7Sn_2)	0.06 ($Li_{13}Sn_5$)	0.1100
$Li_{17}Sn_4$ (nominal $Li_{22}Sn_5$)	1 ($Li_{17}Sn_4$)	-	0.2215
	0.73 ($Li_{17}Sn_4$)	0.27 (Li_7Sn_2)	0.0996

*LiSn doesn't have PDF data due to decomposition during shipping process.

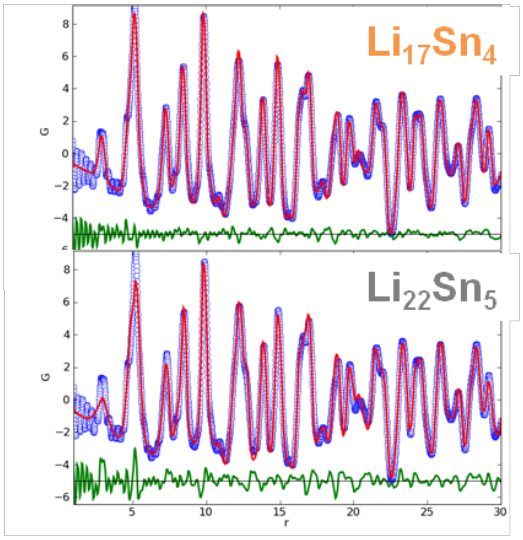

Figure 5.3. Comparison of PDF refinement patterns with $Li_{17}Sn_4$ and $Li_{22}Sn_5$; representative refined patterns (red) overlapped with experimental patterns (blue). The difference between simulated and experimental PDFs is shown in green (offset by -5). The phase composition extracted from the refinement results and refinement statistics for each phase is listed in Table 5.4.

Table 5.4. Comparison of PDF refinement statistics for the nominal $Li_{22}Sn_5$ phase using the $Li_{17}Sn_4$ and $Li_{22}Sn_5$ structures. The first model considered either $Li_{17}Sn_4$ or $Li_{22}Sn_5$, only. The effect of adding a Li_7Sn_2 impurity phase was then explored.

Unit cell parameter(Å)		$Li_{17}Sn_4$	Li_7Sn_2	$Li_{22}Sn_5$	Li_7Sn_2
		a=19.6907	a=9.8000 b=13.8000 c=4.7500	a=19.7640	a=9.8000 b=13.8000 c=4.7500
Sn distribution		1.00		1.00	
unit cell parameter	a	19.6972		19.7071	
Li thermal parameter		0.0223		0.1114	
Sn thermal parameter		0.0157		0.0188	
R_w		0.2215		0.2459	
Sn distribution		0.73	0.27	0.72	0.28
unit cell parameter	a	19.6943	9.8184	19.6867	9.8236
	b		13.8757		13.9658
	c		4.7434		4.7414
Li thermal parameter		0.0202	0.4432	0.1620	0.0644
Sn thermal parameter		0.0110	0.0093	0.0136	0.0104
R_w		0.0996		0.1611	

5.3.3. ^{7}Li solid-state NMR

The ^{7}Li NMR resonances for several Li_xSn_y model compounds are shown in Figure 5.4 and the assigned isotropic peaks are given in Table 5.5. By the analogy with Li_xSi_y system,[36-38] the Sn-rich compounds (Li_2Sn_5 and LiSn) resonate at higher frequencies while the Li-rich compounds (Li_7Sn_3, Li_7Sn_2 and $Li_{17}Sn_4$) resonate at lower frequencies.

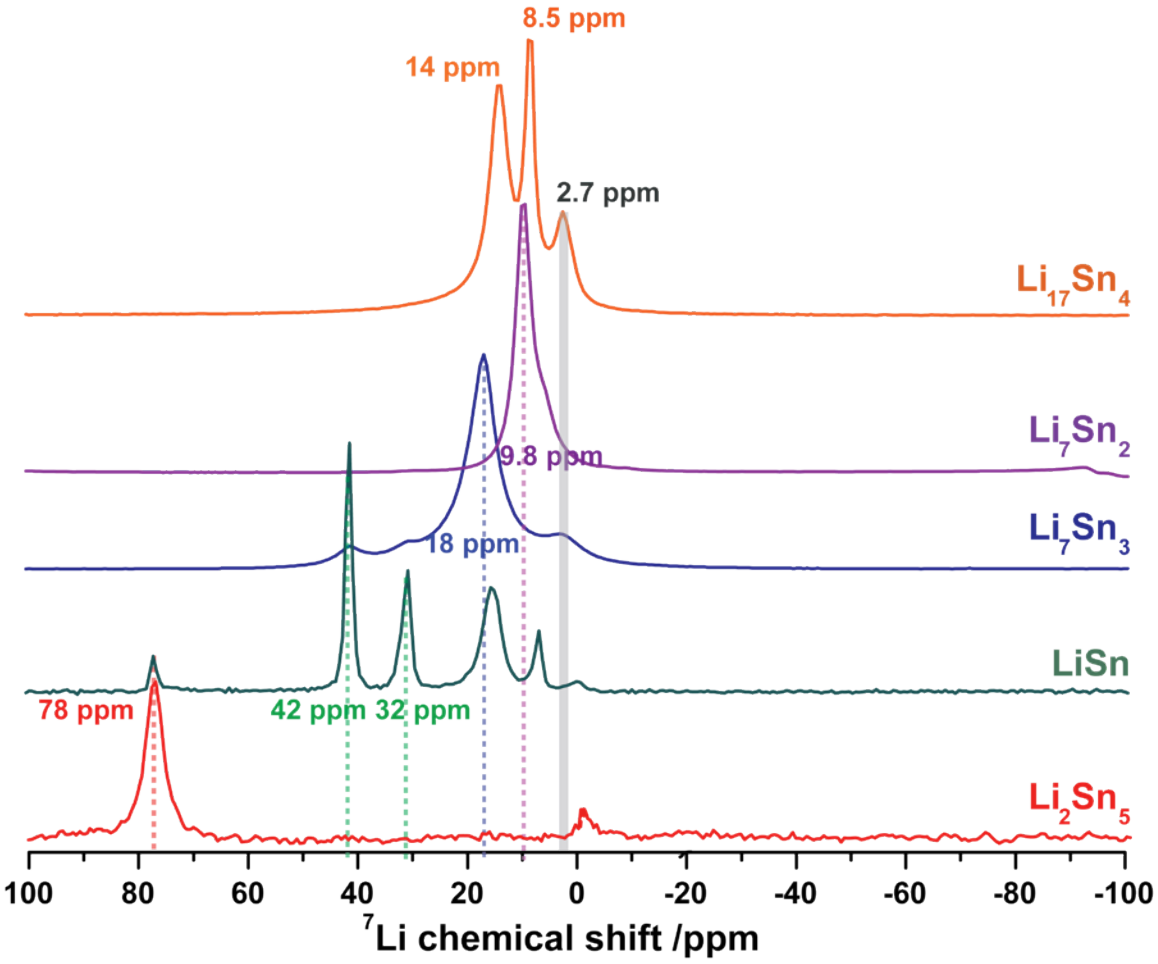

Figure 5.4 ^{7}Li MAS NMR spectra of synthesized Li_2Sn_5, Li_7Sn_3, Li_7Sn_2, and $Li_{17}Sn_4$ and electrochemically lithiated LiSn. The peaks close to 0 ppm correspond to diamagnetic impurities. Dashed lines indicate isotropic peaks for each compound and the grey line indicates a diamagnetic lithium phase such as Li_2O or LiOH.

The Sn-rich compounds have metallic properties[39] due to the Sn electronic structure at the Fermi level resulting in a Knight shift of the ^{7}Li NMR resonance. Li_2Sn_5 has a single Li crystallographic site, isolated by a 3-dimensional Sn network structure and gives rise to a single resonance at +78 ppm, consistent with previous studies.[7] The peak near 0 ppm is attributed to diamagnetic impurities.

Electrochemically prepared LiSn contains a mixture of Li_xSn_y compounds, *i.e.,* Li_2Sn_5 (78ppm), LiSn (42/32 ppm) and Li- rich compounds (15/7 ppm) based on ^{7}Li NMR spectrum, but a major phase can be ascribed to LiSn on the basis of the XRD results. The LiSn structure consists of 2-dimensional Sn layers intercalated by lithium atoms with 2 Li crystallographic sites. Thus the dominant +42 ppm resonance can be assigned to Li1 (2n), while the +32 ppm resonance is assigned to Li2 (1e), in agreement with previously reported values.[7] The resonances at 15 and 7 ppm are tentatively assigned to Li-rich compounds with dumbbell type Sn-Sn bonds (Li_5Sn_2 or $Li_{13}Sn_5$) and Li_7Sn_2, respectively.

For the Sn-rich compounds, the number of isotropic peaks in the ^{7}Li NMR spectra is consistent, for the most part, with the number of Li crystallographic sites. A noticeable discrepancy is observed for the more lithiated Li_7Sn_3 and Li_7Sn_2 phases. Sn-rich compounds contain isolated Li sites compared to Li-rich compounds, so the mobility of Li ions can be suppressed. For Li rich compounds, Bekaert *et al*[7] suggested that either exchange processes occur between different crystallographic sites due to fast Li ion mobility or that the difference of Li environments for each crystallographic site is too small to distinguish from each other.

Li_7Sn_3 has nonlinear trimer Sn-Sn bonds with 7 Li crystallographic sites. In this phase, the main ^{7}Li NMR signal at 18 ppm (77%) corresponds to Li_7Sn_3, consistent with previous studies.[7] The impurities are composed to 13% LiSn and 9% diamagnetic phases (on the basis of peak deconvolution with Dmfit[40] shown in Figure 5.5). The phase composition and fraction of the Li_7Sn_3 obtained from PDF (83% Li_7Sn_3 / 17% LiSn) and NMR (85% Li_7Sn_3 / 15% LiSn excluding the diamagnetic phases which are not detected in PDF) are consistent within the error of fitting.

The more lithiated compound Li_7Sn_2 resonates at 9.8 ppm with small shoulder at 5.8 ppm (% integral is 84% and 16% from peak deconvolution, respectively). Bekaert *et*

al.[7] also reported that this minor resonance (5 ppm) from Li_7Sn_2 appears at 263 K and suggested that a second Li site could be resolved due to reduced Li mobility. Li_7Sn_2 has Sn-Sn dumbbells and isolated Sn atoms with 6 Li crystallographic sites but these are not clearly separated in the ^{7}Li NMR spectra, most likely due to a fast exchange phenomenon.[7] The Li2 site on the edge of the unit cell has the longest Li-Sn distance (>3.4 Å). Thus the resonance at 5.8 ppm is tentatively assigned to this Li site. The PDF analysis suggests that the Li_7Sn_2 phase contains less than 6% $Li_{13}Sn_5$, while NMR shows no obvious ^{7}Li resonance from $Li_{13}Sn_5$, indicating some slight disorder in the Li_7Sn_2 or the presence of a second minor phase.

Several papers have reported ^{7}Li MAS NMR spectra for $Li_{22}Sn_5$,[6,7,10,11] with broad resonances and significant Knight shifts (60~120 ppm). In this work, $Li_{17}Sn_4$ instead of $Li_{22}Sn_5$ was formed by ball milling and annealing. The synthesized $Li_{17}Sn_4$ phase gives rise to resonances at 14, 8.5, and 2.7 ppm. The resonance at 8.5 ppm can be assigned to the Li_7Sn_2 phase impurity, consistent with the XRD and PDF results, and the 2.7 ppm resonance is assigned to Li_2O[41], the oxygen possibly originating from impurities introduced during the ball-milling process. The phase composition and fraction of the $Li_{17}Sn_4$ obtained from PDF (72% $Li_{17}Sn_4$ / 27% Li_7Sn_2) and NMR (67% $Li_{17}Sn_4$ / 33% Li_7Sn_2 excluding the diamagnetic phases which are not detected in PDF) are close. On the basis of the PDF refinement result, the compound synthesized with the nominal composition $Li_{22}Sn_5$ is assigned to $Li_{17}Sn_4$, which is known to have poor metallic properties[34] in contrast with the metallic phase $Li_{22}Sn_5$.[7] This is also supported by the absence of a large Knight shift in the ^{7}Li spectrum.

Table 5.5. Assigned isotropic peaks of ^{7}Li NMR spectra for Li_xSn_y compounds along with the number of crystallographic sites.

Composition	Li sites	Isotropic Chemical shift (ppm)
Li_2Sn_5	1	78
LiSn	2	42, 32
Li_7Sn_3	7	18

Li_7Sn_2	6	9.8
$Li_{17}Sn_4$	13	14

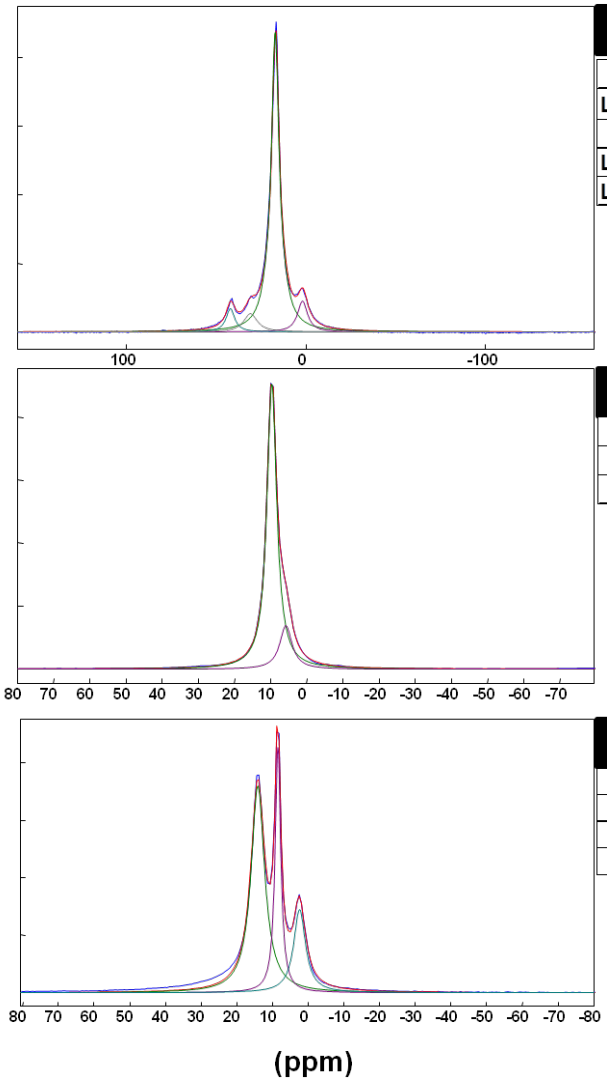

^{7}Li NMR : Li_7Sn_3

	pos(ppm)	wid(Hz)	Integral %
Li_7Sn_3	18	3341.00	77.38
	2	384.00	9.18
LiSn	42	8200.00	6.11
LiSn	32	6021.00	7.34

^{7}Li NMR : Li_7Sn_2

pos(ppm)	wid(Hz)	% integral
9.8	1904.00	84.17
5.5	1069.00	15.83

^{7}Li NMR : $Li_{17}Sn_4$

pos(ppm)	wid(Hz)	% integral
14	2721.00	54.45
8.5	1652.00	26.57
2.7	524.00	18.98

Figure 5.5. Deconvolution results of Li_7Sn_3, Li_7Sn_2 and $Li_{17}Sn_4$, showing the peak position (pos), width (wid) and integral (%).

5.3.4. ^{119}Sn solid-state NMR

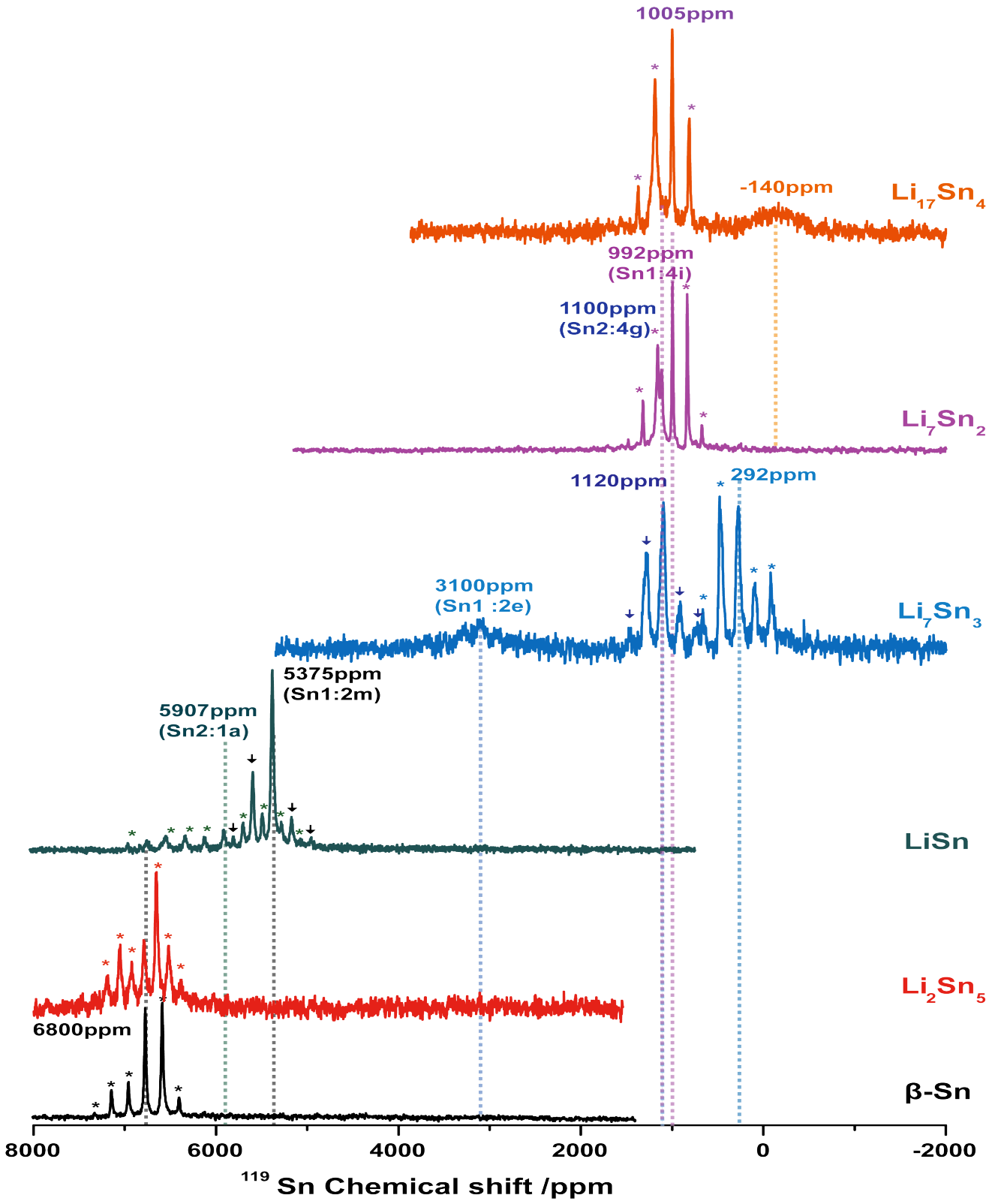

Figure 5.6. ^{119}Sn MAS NMR spectra of β-Sn (at 6750ppm[a] with 35kHz spinning speed), synthesized Li_2Sn_5 (at 6750 ppm[a] with 25 kHz), Li_7Sn_3 (summed spectra from 3000 ppm to 0 ppm with 35 kHz), Li_7Sn_2 (at 750 ppm[a] with 35 kHz) and $Li_{17}Sn_4$ (summed spectra from 3000 ppm to -1500 ppm with 35 kHz) and electrochemically lithiated LiSn (at 6000 ppm[a] with 35 kHz). Each dashed line indicates isotropic peaks for each compound. Each asterik (*) mark indicates a spinning side band. ([a] :irradiation frequency offset)

The ^{119}Sn NMR spectra for β-Sn and the Li_xSn_y model compounds are shown in Figure 5.6. The isotropic peaks for each model compound were identified by comparison of spectra with different spinning speeds (shown in Figures 5.7. (β-Sn and Li_2Sn_5), 5.9 (Li_2Sn_5), 5.11 (Li_7Sn_3), 5.12 (Li_7Sn_2), 5.13 ($Li_{17}Sn_4$), and 5.14 (LiSn)). The Sn-rich compounds (Li_2Sn_5 and LiSn) resonate at higher frequencies, while the Li-rich compounds (Li_7Sn_3, Li_7Sn_2 and $Li_{17}Sn_4$) exhibit resonances at much lower frequencies. This is similar to the trend observed in the ^{7}Li NMR spectra, in which the change of Li shift with lithium content is similar.

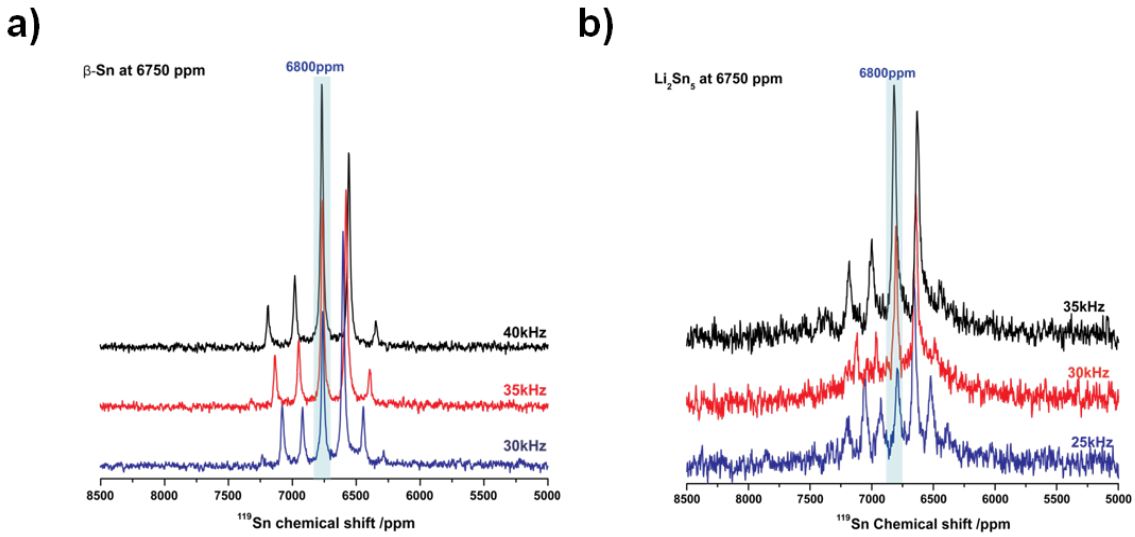

Figure 5.7. ^{119}Sn MAS NMR spectra with different spinning speeds ; a) β-Sn and b) Li_2Sn_5.

β-Sn has I*4*/*amd* symmetry and 1 Sn crystallographic site. Each Sn atom is located in a distorted octahedral site coordinated by 4 Sn (Sn-Sn bond distance: 3.02 Å) and 2 Sn (Sn-Sn bond distance: 3.18Å), as seen in Figure 5.8a. The large ^{119}Sn Knight shift of +6800 ppm is due to the metallic nature of Sn. The ^{119}Sn NMR spectrum of β-Sn also shows large spinning sideband manifolds, which is dominated by large chemical

shift anisotropy (CSA, 524ppm). A η_{cs} of 0.04 (*i.e.*close to a zero value within experimental error) is obtained[42], indicating an axial symmetry of CSA tensors[43], which agrees with the axial symmetry due to the distorted octahedral structure of β-Sn. For the Sn-rich compounds (Li_2Sn_5 and LiSn), the number of nearby Sn sites decreases as Sn is replaced by Li environments. Li_2Sn_5 has a 5-coordinated Sn1 site and a 6-coordinated Sn2 site (Sn1:Sn2=8i:2d). LiSn also has 2 inequivalent Sn crystallographic sites with 4 neighboring Sn, *i.e.*, Sn1 exists as a tetrahedron type, whereas Sn2 has a square planar environment (Sn1:Sn2=2m: 1a).

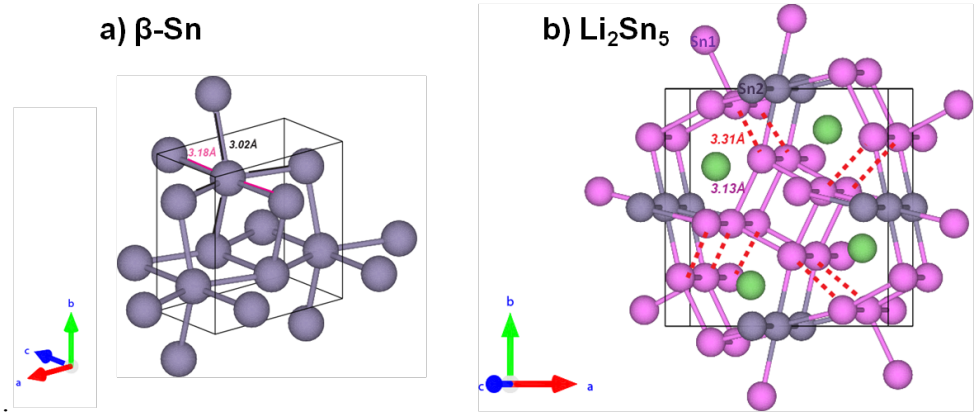

Figure 5.8. The crystal structures of a) β-Sn and b) Li_2Sn_5. β-Sn has two types of Sn-Sn bonds distance. Li_2Sn_5 has a Sn-Sn network with 3.13 Å bond distance; 5 coordinated Sn1 site is quasi 6 coordinate as shown by the red dashed lines. (The closest located Sn distance is 3.31 Å)

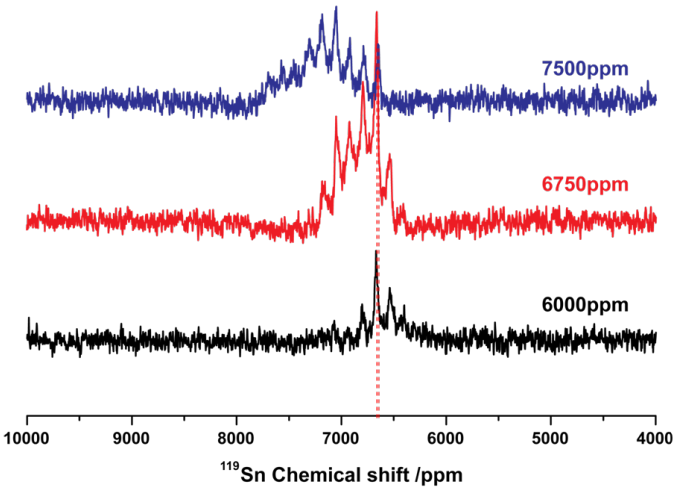

Figure 5.9.^{119}Sn MAS NMR spectra of Li_2Sn_5 acquired with different observe frequencies with 25 kHz spinning speeds. Dashed line indicates an isotropic peak.

The ^{119}Sn NMR signal of Li_2Sn_5 occurs at a shift similar to that of the β-Sn, at 6800 ppm. As there is a decreasing number of neighboring Sn sites, the Sn environments in Li_2Sn_5 is different from β-Sn. However, only one peak is observed at 6800 ppm, which has the same isotropic shift as β-Sn, but has a significantly larger chemical shift asymmetry (η_{cs}) parameter of 0.45 (Table 5.6) compared to η_{cs} =0.04 for β-Sn. As shown in Figure 5.8, the Sn1 site is a quasi 6-coordinated Sn due to the next-nearest Sn atom with a slightly longer Sn-Sn distance of 3.31 Å, in comparison to the shortest Sn-Sn distances of 3.13 Å. Each Sn site in Li_2Sn_5 has a similar coordinated environment to β-Sn and the difference between 2 Sn crystallographic sites in Li_2Sn_5 phase must be too small to be resolved in the^{119}Sn NMR experiment. The reported ^{119}Sn Mössbauer isomer shift (δ) of Li_2Sn_5[13,14](δ(Sn1) = 2.49mm/s and δ(Sn2) = 2.36mm/s), where is related to the s electron density at the Sn nucleus, also shows only a small difference from β-Sn (δ (Sn)=2.56mm/s), consistent with our ^{119}Sn NMR spectra results. However the Mössbauer quadrupole splitting observed for Li_2Sn_5 (Δ(Sn1) = 0.42mm/s and (Δ(Sn2) = 0.78mm/s) is significantly larger than β-Sn (Δ(Sn) = 0.29mm/s). Since the quadrupole splitting is related to asymmetry around the Sn nucleus, this supports the larger chemical shift asymmetry parameter for Li_2Sn_5. As shown in Figure 5.9, an extremely broad component also exists under the 6800ppm resonance, indicating the possible formation of a more disordered Li_2Sn_5 phase, consistent with a poor fit in the PDF refinement. In addition, the dried silica used for diluting Li_2Sn_5 may have reacted with Li_2Sn_5 or contained residual H_2O that reacted with Li_2Sn_5 and produced byproducts. Therefore, the observed 6800ppm resonance is tentatively assigned to Sn1/Sn2 sites of Li_2Sn_5 and unreacted β-Sn (18% from PDF analysis), and the broad component under the 6800ppm is tentatively ascribed to the more disordered Li_2Sn_5 phase.

For Li-rich compounds (Li_7Sn_3, Li_7Sn_2 and $Li_{17}Sn_4$), Sn only exists as isolated atoms or small clusters, *i.e.*, dumbbell or trimer structures (See Figure 5.10). The ^{7}Li NMR resonances of the Li-rich compounds do not have as large of a Knight shift as the Sn-rich compounds.

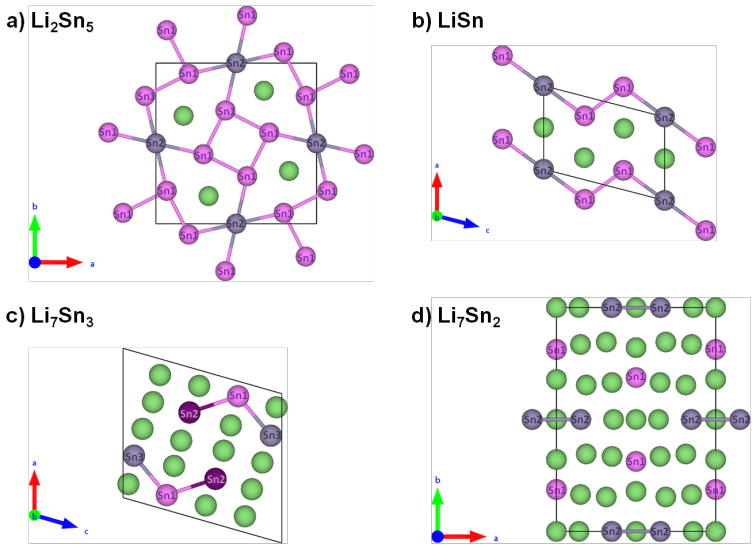

Figure 5.10. The crystal structures of Li_xSn_y model compounds with crystallographic Sn sites investigated as part of this chapter: a) Li_2Sn_5 (Sn1(8i) and Sn2(2d)), b) LiSn (Sn1(2m) and Sn2(1a)), c) Li_7Sn_3 (Sn1(2e), Sn2(2e), and Sn3(2e), d) Li_7Sn_2 (Sn1(4i) and Sn2(4g))

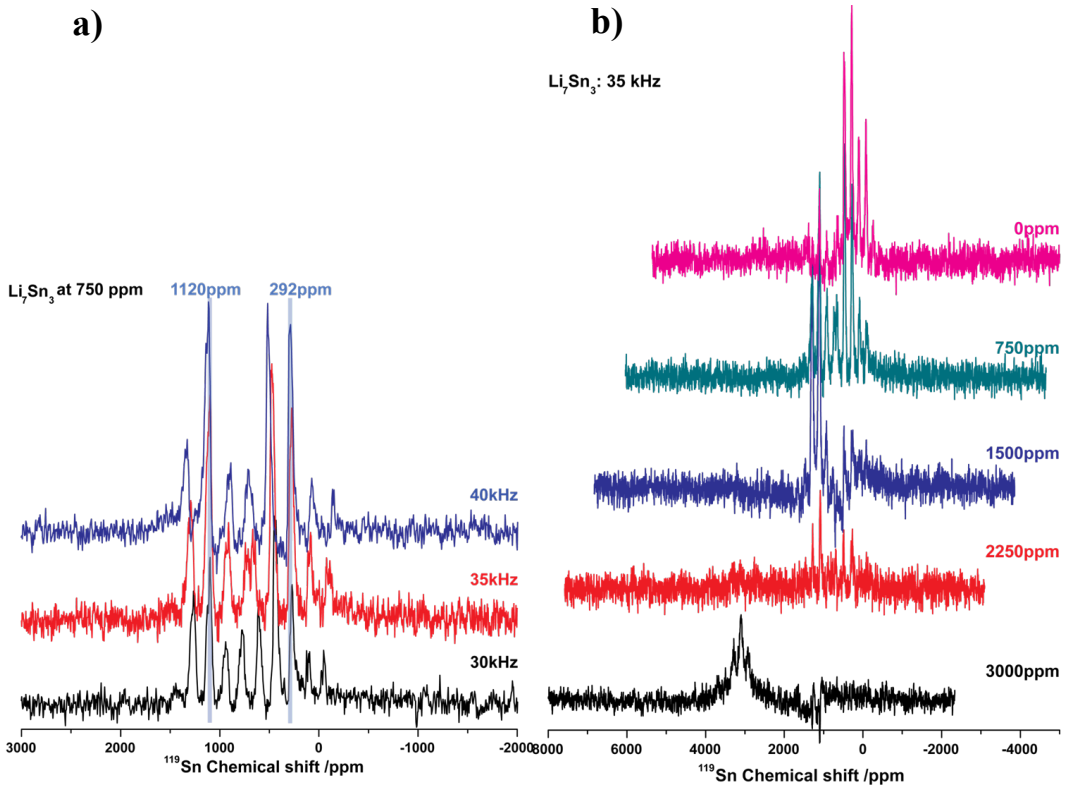

Figure 5.11. ^{119}Sn MAS NMR spectra of Li_7Sn_3; a) spectra with different spinning speeds and b) spin-echo mapping MAS spectra with 35kHz spinning speed.

Li_7Sn_3 has 3 Sn crystallographic sites with a nonlinear trimer Sn structure. The ^{119}Sn NMR signal of Li_7Sn_3 shows three isotropic resonances flanked by a series of spinning side bands at 3100, 1120, and 292 ppm. The resonance at 3100 ppm can be assigned to the bridging Sn atom (Sn1 (2e)) that has two Sn-Sn bonds and is expected to have the greatest Knight shift. The other 2 Sn sites (Sn2 (2e) and Sn3 (2e)) are terminal sites that have similar local environments (one Sn-Sn bond), thus they are tentatively assigned to the 1120ppm resonance. The ^{119}Sn resonance at 292 ppm will be discussed later.

For Li_7Sn_2, two isotropic shifts are observed at 992 and 1100 ppm. In comparison with Li_7Sn_3 spectrum where the ^{119}Sn signal of Sn-Sn dumbbell type shows a similar range of shift at 1120 ppm, the resonance at 1100ppmcan be assigned to Sn-Sn dumbbell sites (Sn2 (4g) Sn-Sn bond distance: 3.00 Å) and 992ppm can be ascribed to isolated Sn (Sn1 (4i)).

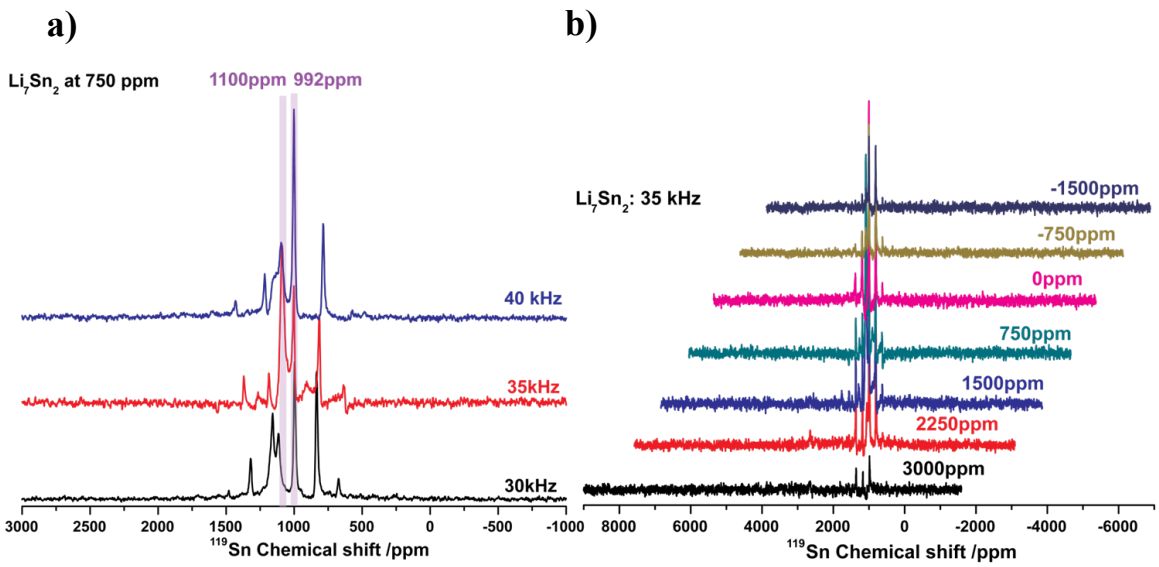

Figure 5.12. ^{119}Sn MAS NMR spectra of Li_7Sn_2; a) spectra with different spinning speeds and b) spin-echo mapping MAS spectra with 35kHz spinning speed.

The ^{119}Sn NMR spectrum of $Li_{17}Sn_4$ results in a very broad peak centered at -140 ppm and a sharp peak at 1005 ppm. $Li_{17}Sn_4$ has only isolated Sn environments with 4 crystallographic sites. $Li_{17}Sn_4$ contains an impurity Li_7Sn_2 phase observed both by PDF

analysis (23%) and ^{7}Li NMR (27%), and the resonance at 1005 ppm support the presence of the impurity Li_7Sn_2 phase.

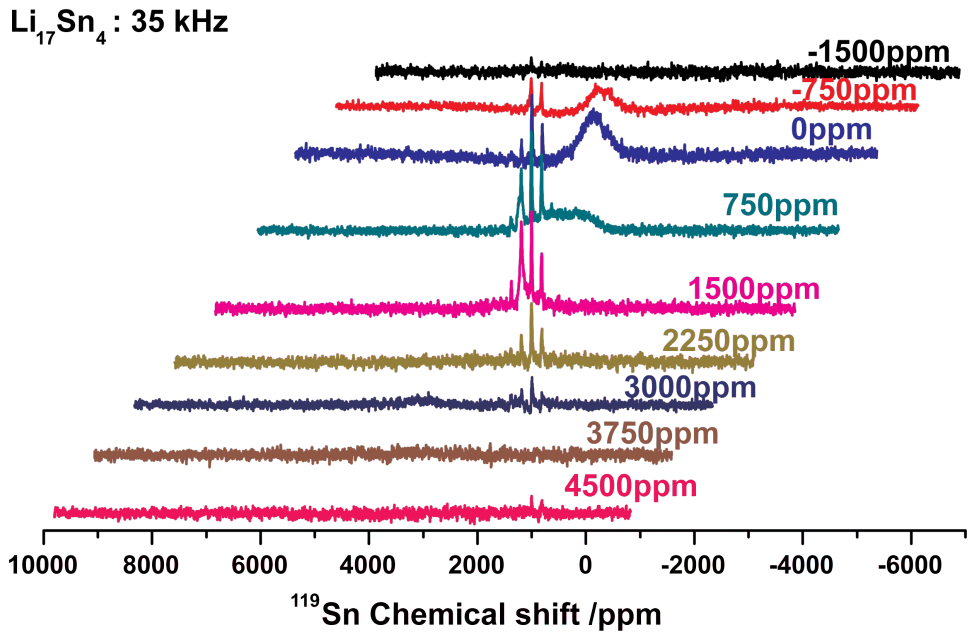

Figure 5.13. ^{119}Sn MAS NMR spectra of $Li_{17}Sn_4$: spin-echo mapping MAS spectra with 35kHz spinning speed.

The ^{119}Sn resonance at 292 ppm in Li_7Sn_3 is at a lower frequency than an isolated Sn structure of Li_7Sn_2 (992 ppm), thus this shift indicates that Li_7Sn_3 contains a different Sn environment, which is more shielded by Li. Further study is required to provide more detailed information on the structure for this resonance.

LiSn prepared electrochemically gives rise to two isotropic peaks at 5375 and 5905 ppm, corresponding to 2 different Sn sites (Sn1 (2m) and Sn2 (1a)). The dominant peak at 5375 ppm can be assigned to Sn1 (2m, tetrahedron type) site based on the multiplicity of the sites, while the weak peak near 5905 ppm is associated with Sn2 site (1a, square planar type). Haarmann *et al.*[44] also observed one broad peak near 5400 ppm, using a rotational frequency of 15 kHz at a magnetic field strength of 11.74 T, but did not observe a second resonance. In contrast, our ^{119}Sn signals are clearly resolved as the different 2 Sn sites due to faster magic-angle spinning (35 kHz) at the same magnetic

field. The sample also contains Li_2Sn_5 according ^7Li NMR result, which results in near 6780 ppm.

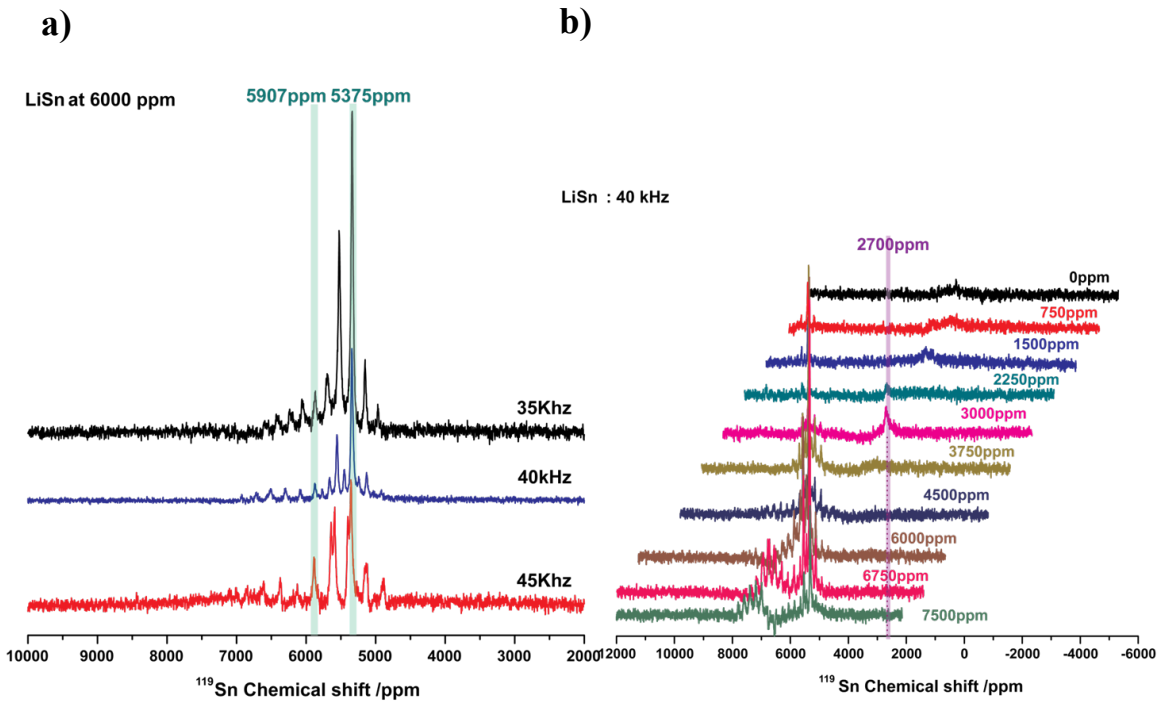

Figure 5.14. ^{119}Sn MAS NMR spectra of LiSn; a) spectra with different spinning speeds and b) spin-echo mapping MAS spectra with 40kHz spinning speed.

Table 5.6. Assigned ^{119}Sn NMR signals of for the Li_xSn_y compounds with number of crystallographic sites.

Compounds	# of Sn sites	Site designation	% area[a]	δ_{iso} (ppm)	CSA (ppm)	η_{cs}	η_{cs} error
β-Sn	1	4a	-	6800	524	0.04	+/-0.10
Li_2Sn_5	2	Sn1(8i)/Sn2(2d)	-	6800	564	0.45	+/-0.01
LiSn	2	Sn2(1a)	39	5907	831	0.72	+/-0.02
		Sn1(2m)	61	5375	-411	0.02	+/-0.12
Li_7Sn_3	3	Sn1(2e)		3100	429	0.94	+/-0.05
		Sn2(2e)	43	1120	-425	0.27	+/-0.12
		2e	57	292	-585	0.28	+/-0.06
Li_7Sn_2	2	Sn2(4g)	53	1100	182	0.07	+/-8.82
		Sn1(4i)	47	992	443	0.07	+/-0.40
$Li_{17}Sn_4$	4	16e/16e/24f/24g	-	-140			

[a]On the basis of peak deconvolution with Dmfit[40] shown in Figure 5.15.

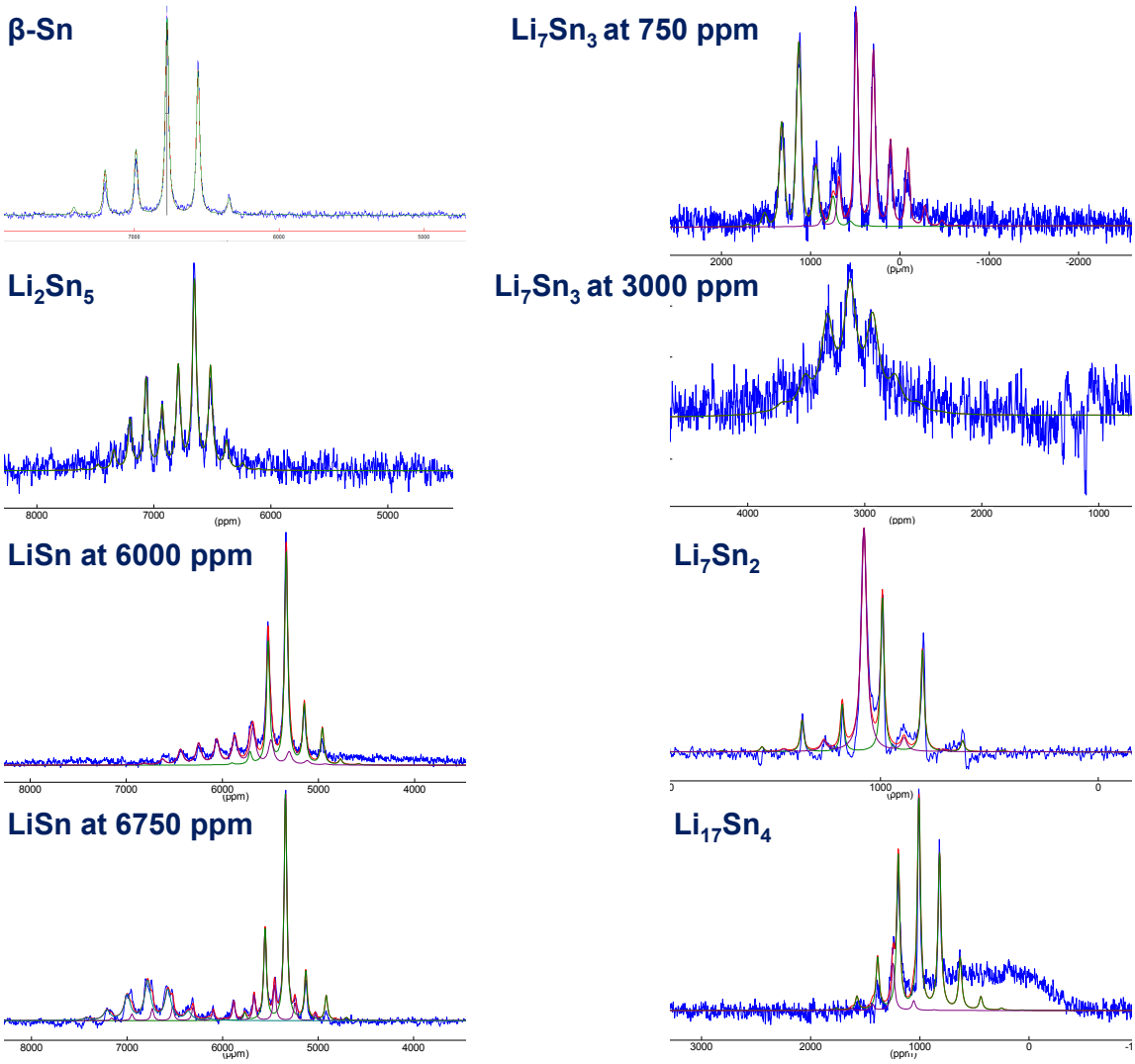

Figure 5.15. ^{119}Sn MAS NMR deconvoluted spectra.

β-Sn (at 6750ppm[a]), Li_2Sn_5 (at 6750ppm[a]), Li_7Sn_2 (at 750 ppm[a]) and $Li_{17}Sn_4$ (at 750 ppm[a])

([a] :irradiation frequency offset)

5.4. Conclusions

Crystalline Li_xSn_y model compounds (Li_2Sn_5, LiSn, Li_7Sn_3, Li_7Sn_2, and $Li_{17}Sn_4$) have been synthesized and characterized with XRD, PDF, and ^{7}Li/ ^{119}Sn high-resolution solid-state NMR.

^{7}Li and ^{119}Sn NMR signals have shown a clear trend, as lithium content increases, each shift moving toward lower frequencies. On the basis of Sn structures, model compounds are divided into two distinct groups; the Sn-rich compounds (Li_2Sn_5, LiSn) and the Li-rich compound (Li_7Sn_3, Li_7Sn_2, and $Li_{17}Sn_4$). ^{119}Sn NMR results could be useful to identify Li_xSn_y phases in electrochemically lithiated Sn systems.

5.5. References

(1) Chevrier, V. L.; Ceder, G. *J. Electrochem.Soc.* **2011**, *158*, A1011.

(2) Wang, X. L.; Han, W. Q.; Chen, J.; Graetz, J. *ACS Appl. Mater. Interfaces* **2010**, *2*, 1548.

(3) Chen, J. *Materials* **2013**, *6*, 156.

(4) Zhang, W.-J. *J. Power Sources* **2011**, *196*, 13.

(5) Park, C. M.; Kim, J. H.; Kim, H.; Sohn, H. J. *Chem. Soc. Rev.* **2010**, *39*, 3115.

(6) Furuya, K. O., K.; Mineo, Y.; Matsufuji, A.; Okuda, J.; Erata,T. J. *J. Phys.: Condens. Matter 2001* **2001**, *13*, 3519.

(7) Bekaert , E.; Robert, F.; Lippens, P. E.; Ménétrier , M. *J. Phys. Chem. C* **2010**, *114*, 6749.

(8) Goward, G. R.; Nazar, L. F.; Power, W. P. *J. Mater. Chem.* **2000**, *10*, 1241.

(9) Idota Y, K. T., Matsufuji A, Maekawa Y, Miyasaja T *Science* **1997**, *276*, 1395.

(10) Wang, Y. S., J.; Huang, C. K.; Surampudi, S.; Greenbaum,; G., S. *Solid State Ionics* **1998**, *110*, 167.

(11) Goward, G. R.; Leroux, F.; Power, W. P.; Ouvrard, G.; Dmowski, W.; Egami, T.; Nazar, L. F. *Electrochem. Solid-State Lett.* **1999**, *2*, 367.

(12) Idota, Y.; Kubota, T.; Matsufuji, A.; Maekawa, Y.; Miyasaja, T. *Science* **1997**, *276*, 1395.

(13) Robert, F.; Lippens, P. E.; Olivier-Fourcade, J.; Jumas, J. C.; Gillot, F.; Morcrette, M.; Tarascon, J. M. *J. Solid State Chem.* **2007**, *180*, 339.

(14) Dunlap, R. A.; Small, D. A.; MacNeil, D. D.; Obrovac, M. N.; Dahn, J. R. *J.Alloys Compd.* **1999**, *289*, 135.

(15) Noh, M.; Kwon, Y.; Lee, H.; Cho, J.; Kim, Y.; Kim, M. G. *Chem. Mater.* **2005**, *17*, 1926.

(16) Hammersley, A. P.; Svensson, S. O.; Hanfland, M.; Fitch, A. N.; Hausermann, D. *High Pressure Res.* **1996**, *14*, 235.

(17) Qiu, X.; Thompson, J. W.; Billinge, S. J. L. *J. Appl. Crystallogr* **2004**, *37*, 678.

(18) Farrow, C. L.; Juhás, P.; Liu, J. W.; Bryndin, D.; Božin, E. S.; J. Bloch; Proffen, T.; Billinge, S. J. L. *J. Phys.: Condens. Matter* **2007**, *19*, 335219.

(19) Mali, G., Ristic, A., and Kaucic, V. *J. Phys. Chem. B* **2005**, *109*, 10711.

(20) Canesson, L. a. T., A. *Chem. Commun.* **1997**, 241.

(21) Sananes, M. T. a. T., A. *J. Chem. Soc., Chem. Commun.* **1995**, 1323.

(22) Tong, Y. Y. *J. Magn. Reson., Ser. A* **1996**, *119*, 22.

(23) Sananes, M. T., Tuel, A., and Volta, J. C. *J. Catal.* **1994**, *145*, 251.

(24) Massiot, D., Farnan, I., Gautier, N., Trumeau, D., Trokiner, A., and Coutures, J. P. *Solid State Nucl. Magn. Reson.* **1995**, *4*.

(25) Ash, J. T. a. G., P. J. *Magn. Reson. Chem.* **2006**, *44*.

(26) Schurko, R. W., Wi, S., and Frydman, L. *J. Phys. Chem. A* **2002**, *106*, 51.

(27) Tong, Y. Y. *J. Magn. Reson., Ser A* **1996**, *119*, 22.

(28) Kim, J.; Middlemiss, D. S.; Chernova, N. A.; Zhu, B. Y. X.; Masquelier, C.; Grey, C. P. *J. Am. Chem. Soc.* **2010**, *132*, 16825.

(29) Hansen, D. A.; Chang, L. J. *Acta Crystallogr.,Sect. B: Struct. Sci.* **1969**, *25*, 2392.

(30) Schäfer, H.; Eisenmann, B.; Müller, W. *Angew. Chem. int. Ed.* **1973**, *12*, 695.

(31) Müller, W. *Z. Naturforsch., B: J. Chem. Sci* **1974**, *29b*, 304.

(32) Frank, U.; Müller, W.; Schäfer, H. *Z. Naturforsch., B: J. Chem.Sci* **1975**, *30b*, 6.

(33) Gladyshevski, E. I. O., G. I.; Kripyakevich, P. I. *Sov. Phys. Crystallogr.* **1964**, *9*, 269.

(34) Lupu, C.; Mao, J.-G.; Rabalais, J. W.; Guloy, A. M.; Richardson, J. W. *Inorg. Chem.* **2003**, *42*, 3765.

(35) Morris, A. J.; Grey, C. P.; Pickard, C. J. *Condens. Matter Phys.* **2014**.

(36) Key, B.; Bhattacharyya, R.; Morcrette, M.; Seznéc, V.; Tarascon, J.-M.; Grey, C. P. *J. Am. Chem. Soc.* **2009**, *131*, 9239.

(37) Ogata, K.; Salager, E.; Kerr, C. J.; Fraser, A. E.; Ducati, C.; Morris, A. J.; Hofmann, S.; Grey, C. P. *Nat. Commun.* **2014**, *5*, 3217.

(38) Jung, H.; Allan, P. K.; Hu, Y.-Y.; Borkiewicz, O. J.; Wang, X.-L.; Han, W.-Q.; Du, L.-S.; Pickard, C. J.; Chupas, P. J.; Chapman, K. W.; Morris, A. J.; Grey, C. P. *Chem. Mater.* **2015**.

(39) Ienco, A.; Hoffmann, R.; Papoian, G. *J. Am. Chem. Soc.* **2001**, *123*, 2317.

(40) Massiot, D.; Fayon, F.; Capron, M.; King, I.; Le Calvé, S.; Alonso, B.; Durand, J. O.; Bujoli, B.; Gan, Z.; Hoatson, G. *Magn. Reson. Chem.* **2002**, *40*, 70.

(41) Meyer, B. M.; Leifer, N.; Sakamoto, S.; Greenbaum, S. G.; Grey, C. P. *Electrochem. Solid-State Lett.* **2005**, *8*, A145.

(42) Bak, M.; Rasmussen, J. T.; Nielsen, N. C. *J. Magn. Reson., Ser A* **2000**, *147* 296.

(43) Levitt, M. *Spin Dynamics: Basics of Nuclear Magnetic Resonance*; Wiley, 2008.

(44) Haarmann, F.; Grüner, D.; Bezugly, V.; Rosner, H. a.; Grin, Y. *Z. anorg. allg. Chem.* **2006**, *632*, 1423.

Chapter 6. Conclusions

This work provides a variety of *ex-/in-situ*, experimental techniques, which probe short-, medium-, and long-range structure in combination with structural and energetic predictions from DFT studies can be used to obtain comprehensive insights into complex lithiation mechanisms in alloy phases. This characterization method can also apply to a similar alloy anodes and amorphous multi-phase (de) lithiated systems for better understanding the long-range and local structural variations during cycling.

1) Relevant model compounds (Li_7Ge_3, Li_7Ge_2, $Li_{15}Ge_4$, and $Li_{22}Ge_5$) were first synthesized and identified by XRD, PDF, and *ex-situ* high-resolution ^7Li solid-state NMR spectroscopy. Model compound study provides experimental signatures for identifying the (de) lithiated germanium phase during cycling.

2) (De) lithiation mechanisms of micron and nano-sized germanium have been studied in detail by identifying the long range and local structural transformations, on the basis of relevant model compound study.

3) Li_xSn_y model compounds (Li_2Sn_5, LiSn, Li_7Sn_3, Li_7Sn_2,and $Li_{17}Sn_4$) were synthesized and characterized by XRD, PDF, and *ex situ* high-resolution ^7Li/ ^{119}Sn solid-state NMR spectroscopy.^{119}Sn NMR is first introduced to provide the local structural environments of Sn in Li_xSn_y.